T.R.

GEBZE TECHNICAL UNIVERSITY

GRADUATE SCHOOL OF NATURAL AND APPLIED SCIENCE

INVESTIGATION OF ELECTROCALORIC PROPERTIES OF TEXTURED 0.72PMN-0.28PT THICK FILMS

İREM BÖBREK

A THESIS SUBMITTED FOR THE DEGREE OF

MASTER OF SCIENCE

DEPARTMENT OF MATERIALS SCIENCE AND ENGINEERING

GEBZE

2022

T.R.

GEBZE TECHNICAL UNIVERSITY

GRADUATE SCHOOL OF NATURAL AND APPLIED SCIENCE

INVESTIGATION OF ELECTROCALORIC PROPERTIES OF TEXTURED 0.72PMN-0.28PT THICK FILMS

İREM BÖBREK

A THESIS SUBMITTED FOR THE DEGREE OF

MASTER OF SCIENCE

DEPARTMENT OF MATERIALS SCIENCE AND ENGINEERING

THESIS SUPERVISOR

PROF. DR. EBRU MENŞUR ALKOY

GEBZE

2022

T.C.

GEBZE TEKNİK ÜNİVERSİTESİ

FEN BİLİMLERİ ENSTİTÜSÜ

DOKULU 0.72PMN-0.28PT KALIN FİLMLERİN ELEKTROKALORİK ÖZELLİKLERİNİN İNCELENMESİ

İREM BÖBREK

YÜKSEK LİSANS TEZİ

MALZEME BİLİMİ VE MÜHENDİSLİĞİ ANABİLİM DALI

DANIŞMANI

PROF. DR. EBRU MENŞUR ALKOY

GEBZE

2022

GEBZE TEKNİK ÜNİVERSİTESİ	**YÜKSEK LİSANS JÜRİ ONAY FORMU**

GTÜ Fen Bilimleri Enstitüsü Yönetim Kurulu'nun 07/02/2022 tarih ve 2022/08 sayılı kararıyla oluşturulan jüri tarafından 24/02/2022 tarihinde tez savunma sınavı yapılan İrem Böbrek'ın tez çalışması Malzeme Bilimi ve Mühendisliği Anabilim Dalında YÜKSEK LİSANS tezi olarak kabul edilmiştir.

JÜRİ

ÜYE (TEZ DANIŞMANI)	: Prof. Dr. Ebru Menşur Alkoy
ÜYE	: Dr. Öğretim Üyesi Abdülkerim Gök
ÜYE	: Dr. Öğretim Üyesi Ayşe Berksoy Yavuz

ONAY

Gebze Teknik Üniversitesi Fen Bilimleri Enstitüsü Yönetim Kurulu'nun

...…/……/…… tarih ve ……/…..... sayılı kararı.

SUMMARY

In this thesis study, lead magnesium niobate (PMN)−lead titanate (PT) with composition of the morphotropic phase boundary (MPB) was investigated. $0.72(Pb_{1/3}Mg_{2/3}Nb_{2/3})$-$0.28(PbTiO_3)$ (0.72PMN−0.28PT) ceramics were produced by the tape-casting and dry-press methods. The ceramic powders were synthesized by solid state calcination method. Barium titanate ($BaTiO_3$) and strontium titanate ($SrTiO_3$) template particles were synthesized by molten salt synthesis method. These particles were used to texture the PMN-PT ceramics. Additionally, ceramics were fabricated with 0.5% mole and 1% mole manganese addition. All samples were sintered at 1150ºC or 1200ºC at various durations. Phase analysis was carried out by X-ray diffraction (XRD) method. Scanning electron microscope (SEM) was used for microstructural analysis of the ceramics. Dielectric, ferroelectric, piezoelectric, electrocaloric properties of 0.72PMN-0.28PT depending on texture, temperature and doping element were also investigated and discussed in detail. This thesis study was financially supported by AFOSR, awarded number #FA9550-18-1-0450 and supported by GTÜ-BAP project number 2020-A-101-10.

Keywords: Lead-based Ferroelectrics, PMN-PT, Textured, Templated particles, Electrocaloric Effect.

ÖZET

Bu tez çalışmasında, morfotropik faz sınırına (MFS) yakın kurşun magnezyum niyobat (PMN)-kurşun titanat(PT) incelenmiştir. $0.72(Pb_{1/3}Mg_{2/3}Nb_{2/3})-0.28(PbTiO_3)$ kompozisyonu, katı hal kalsinasyonu ile sentezlenip, seramikler şerit döküm ve kuru pres yöntemleri ile üretilmiştir. PMN-PT seramiklerinde doku oluşumu için kullanılan baryum titanat ($BaTiO_3$) ve stronsiyum titanat ($SrTiO_3$) şablon parçaları ergiyik tuz sentezi ile elde edilmiştir. Ayrıca %0.5 mol ve %1 mol Mangan katkılı kuru pres yöntemiyle PMN-PT seramikleri üretilmiştir. Tüm numuneler çeşitli sürelerde 1150ºC veya 1200ºC de sinterlenmiştir. Faz analizi, X-ışını kırınımı (XRD) yöntemi ile gerçekleştirilmiştir. Seramiklerin mikroyapısal analizi için taramalı elektron mikroskobu (SEM) kullanılmıştır. 0.72PMN-0.28PT'nin doku, sıcaklık ve katkı elementine bağlı olarak dielektrik, ferroelektrik, piezoelektrik, elektrokalorik özellikleri de araştırılmış ve detaylı olarak tartışılmıştır. Bu tez çalışması, AFOSR tarafından #FA9550-18-1-04-50 proje numarası ve GTÜ-BAP tarafından #2020-A-101-10 proje numarası ile finansal olarak desteklenmiştir.

Anahtar Kelimeler: Kurşun esaslı ferroelektrik, PMN-PT, Dokulu, Şablon Tane, Elektrokalorik etki.

ACKNOWLEDGEMENT

I would like to express my gratitude to my advisor Prof. Dr. Ebru MENŞUR-ALKOY for her constant guidance, support and motivation during my thesis study and education. Also, thanks to Prof. Dr. Sedat ALKOY for his guidance and criticism during successfully completing of this thesis.

I want to thank to thesis committee members Assist. Prof. Abdülkerim GÖK and Assist. Prof. Ayşe BERKSOY-YAVUZ for their criticism and valuable opinions. Additionally, I would like to thank to Prof. Dr. İ. Burç MISIRLIOĞLU from Sabancı University and Assist. Prof. M. Barış OKATAN from IYTE for valuable contribution for electrocaloric analyses.

Thanks to each member of 'Piezo Research Group' and many other colleagues of Gebze Technical University, Department of Materials Science and Engineering for their contribution of my study.

Additional appreciation to Dr. Ali SAYIR for his motivational and financial support of American Air Force Scientific Research Office-Project Award #FA9550-18-1-0450. And thanks to support of Gebze Technical University-BAP project number #2020-A-101-10.

Last and the biggest gratitude to my family then to my friends for their constant support, effort, and joy in my life.

TABLE of CONTENTS

	Page
SUMMARY	v
ÖZET	vi
ACKNOWLEDMENTS	vii
TABLE of CONTENTS	viii
LIST of ABBREVIATIONS and ACRONYMS	x
LIST of FIGURES	xii
LIST of TABLES	xvii
1. INTRODUCTION	1
1.1. Aim of The Study	2
2. LITERATURE REVIEW	3
2.1. Electroceramics	3
2.2. Piezoelectrics	5
2.3. Ferroelectrics	7
2.3.1. Relaxor Ferroelectrics	10
2.3.2. Perovskite Structure	13
2.3.3. PMN-PT Solid Solution	15
2.4. Caloric Effect	17
2.4.1. Electrocaloric Effect	18
2.4.2. Thermodynamic of Electrocaloric Measurements	23
2.4.3. Types of Electrocaloric Measurements	28
3. EXPERIMENTAL STUDY	29
3.1. Synethesis of PMN-PT Powders	29
3.2. Preparation of the Dry Pressed Samples	31
3.3. Processing of Tape Cast Samples	31
3.4. Preparation of $BaTiO_3$ and $SrTiO_3$ Templates	33
3.5. Characterization	33

4. RESULTS and DISCUSSION 36
4.1. Structural Analyses 36
4.1.1. Phase and Microstructural Analyses of PMN-PT Powder 36
4.1.2. Structural Analyses of Templates 37
4.1.3. Structural Analyses of 0.72PMN-0.28PT Ceramics 39
4.2. Microstructural Analyses of the PMN-PT Thick Films 42
4.2.1. SEM Analyses of Tape Cast Ceramics 42
4.2.2. SEM Analyses of Dry pressed Ceramics 46
4.3. Electrical Measurement Results 49
4.3.1. Dielectric Measurement Results 49
4.3.2. Bipolar and Monopolar Strain Measurement Results 52
4.3.3. Electrocaloric Measurement Results and Analyses 56
5. CONCLUSION 69

REFERENCES 71
BIOGRAPHY 74

LIST OF ABBREVATIONS AND ACRONYMS

Abbreviations and Aronyms:		**Explanations**
Å	:	Angstrom
C	:	Capacitance
cm	:	Centimeter
COR	:	Chemically Ordering Region
E_c	:	Coercive Field
C	:	Coulomb
T_c	:	Curie Temperature
^oC	:	Celsius
K	:	Dielectric Constant
ε_r	:	Dielectric Permittivity
DC	:	Direct Current
DSC	:	Differential Scanninig Calorimetry
DTA	:	Differential Thermal Analysis
E	:	Electric Field
ECE	:	Electrocaloric Effect
eV	:	Electrovolt
ΔS	:	Entropy Change
Q	:	Isothermal Heat
G		Gibbs Free Energy
H	:	Magnetic Field
$C_E(T)$	:	Heat Capacity
Hz	:	Hertz
h	:	Hour
kV	:	Kilovolt
kV/cm	:	Kilovolt per centimeter
tanδ	:	Loss Tangent
MPa	:	Megapascal

m	:	Meter
m^2	:	Meter square
µm	:	Micrometer
$\mu C/cm^2$	:	Microcoulomb per centimeter square
min	:	Minute
Mc	:	Magnetocaloric Effect
mc	:	Mechanocaloric Effect
MPB	:	Morphotropic Phase Boundary
%	:	Percentage
pC/N	:	PicoCoulomb per Newton
pm/V		Picometer per Voltage
P_r	:	Remnant Polarization
P_s	:	Spontaneous Polarization
S	:	Strain
SEM	:	Scanning Electron Microscope
ΔT_{EC}	:	Temperature Change
ε_0	:	Vacuum Dielectric Permittivity
V	:	Voltage
wt	:	Weight
XRD	:	X-ray Diffraction
$BaTiO_3$	:	Barium Titanate
$MgNb_2O_6$	:	Magnesium Niobium Oxide
MnO_2	:	Manganese Dioxide
Nb_2O_6	:	Niobium Oxide
PbO	:	Lead Oxide
PMN	:	Lead Magnesium Niobate
PNR	:	Polar Nano Region
PT	:	Lead Titanate
PZT	:	Lead Zirconate Titanate
TiO_2	:	Titanium Dioxide

LIST OF FIGURES

Figure Number:		Page
2.1:	Relationships between dielectric, piezoelectric, pyroelectric, and ferroelectric materials.	4
2.2:	The plot of substitutions effect on Curie temperature.	4
2.3:	Heckmann diagram.	6
2.4:	Schematic illustration of 32 crystal groups.	6
2.5:	a) non-polar alignment, b-c) polar alignment. The arrows show the direction of P_s	8
2.6:	Plots belong to different type of materials.	9
2.7:	a) Ferroelectric hysteresis and b) butterfly loops.	9
2.8:	Schematic illustration of different domain stabilization modality due to length scales of microstructure.	9
2.9:	Plots belong to ferroelectrics and relaxor ferroelectric materials.	12
2.10:	Schematic illustration of temperature dependence of PMN relaxor's nano-regions.	13
2.11:	Schematic illustration of perovskite structure.	14
2.12:	Piezoelectric materials development depends on years.	14
2.13:	a) Phase diagram of the (1-x) PMN-xPT relaxor ferroelectric system with application types. b) PMN-PT detailed crystal structure.	16
2.14:	Schematic illustration of perovskite unit cell due to polarization rotation.	16
2.15:	Dielectric permittivity vs. temperature plots as a function of PT content.	16
2.16:	Schematic illustration of various caloric effect and their correlation between each other.	17
2.17:	Electrothermal properties, applied forces and their response relationship on the Heckmann diagram.	19
2.18:	Temperature vs. time plot depend on caloric effect (EC:electrocaloric)	19

2.19: Illustration of ECE cooling system working principle. 20
2.20: The chronological timeline of caloric materials due to use of caloric materials type. 21
2.21: The illustration of cubic perovskite structure in the middle with different technological application type. 22
3.1: The flow chart of the fabrication of $MgNb_2O_6$ and PMN-PT powders by columbite and solid-state calcination methods. 30
3.2: The flow chart for production of PMN-PT ceramic samples. 32
3.3: Schematic representation of sample preparation process. 32
3.4: Precision LC ferroelectric tester device. 35
3.5: LCR meter device. 35
4.1: XRD pattern of $MgNb_2O_6$ powder. 37
4.2: XRD pattern, SEM micrograph, and particle size distribution graph of 0.72PMN-0.28PT powder after the calcination. 37
4.3: XRD pattern and SEM micrograph (inset figure) of $BaTiO_3$ templates. 38
4.4: XRD pattern and SEM micrograph (inset figure) of $SrTiO_3$ templates. 38
4.5: Comparison of XRD patterns of random and textured PMN-PT ceramics with 5% mole BT template addition. 39
4.6: Comparison of XRD patterns of random and textured PMN-PT ceramics sintered at 1200ºC for 4h with 5% mole BT template addition. 40
4.7: Comparison of XRD patterns of random and textured PMN-PT ceramics sintered at 1200ºC for 8h with 5% mole BT template addition. 40
4.8: Comparison of XRD patterns of random and textured PMN-PT ceramics sintered at 1150ºC for 5h with 1% mole BT template addition. 41
4.9: Comparison of XRD patterns of undoped and doped PMN-PT ceramic samples with 0.5% mole and 1% mole Mn addition of PMN-PT. 41
4.10: SEM micrograph of cross section of random PMN-PT ceramic sample with different magnification. 42

4.11: SEM micrograph of cross section of random PMN-PT ceramic sample with 5% mole BT and sintered at 1150ºC for 4h. 43
4.12: SEM micrograph of cross section of random PMN-PT ceramic sample with 5% mole BT and sintered at 1200ºC for 4h. 43
4.13: SEM micrograph of cross section of random PMN-PT ceramic sample with 5% mole BT and sintered at 1200ºC for 8h. 43
4.14: SEM micrograph of cross section of random PMN-PT ceramic sample with 1% mole BT. 44
4.15: SEM micrograph of cross section of random PMN-PT ceramic sample with 5% mole ST. 44
4.16: SEM micrograph of surface of random PMN-PT ceramic. 44
4.17: SEM micrograph of surface of textured PMN-PT ceramic sample with 5% mole BT and sintered at 1150ºC for 4h. 45
4.18: SEM micrograph of surface of textured PMN-PT ceramic sample with 5% mole BT and sintered at 1200ºC for 4h. 45
4.19: SEM micrograph of surface of textured PMN-PT ceramic sample with 5% mole BT and sintered at 1200ºC for 8h. 45
4.20: SEM micrograph of surface of random PMN-PT ceramic sample with 1% mole BT. 46
4.21: SEM micrograph of surface of textured PMN-PT ceramic sample with 5% mole ST. 46
4.22: Comparison of SEM cross section analyses of PMN-PT samples: a-b) undoped c-d) 0.5% mole Mn e-f) 1% mole Mn doped dry pressed. 47
4.23: Comparison of SEM surface images of PMN-PT samples: a-b) undoped c-d) 0.5% mole Mn e-f) 1% mole Mn doped dry pressed 48
4.24: Comparison of dielectric constant and loss tangent vs. temperature plots of PMN-PT ceramic samples: a) Random, b) 5% mole BT sintered at 1150ºC for 4h, c) 5% mole BT sintered at 1200ºC for 4h d) 1% mole BT, e) 5% mole ST. 50
4.25: Comparison of dielectric constant and loss tangent vs. temperature plots of PMN-PT ceramic samples: a) undoped and b) doped with 1% mole Mn. 51

4.26: Comparison of strain vs. electric field plots of random PMN-PT ceramics: a) Bipolar and b) Unipolar. 52
4.27: Comparison of strain vs. electric field plots of PMN-PT ceramics with 5% mole BT sintered at 1150ºC for 4h: a) Bipolar and b) Unipolar. 52
4.28: Comparison of strain vs. electric field plots of PMN-PT ceramic with 5% mole BT sintered at 1200ºC for 4h: a) Bipolar and b) Unipolar. 53
4.29: Comparison of strain vs. electric field plots of PMN-PT ceramics with 5% mole BT sintered at 1200ºC for 8h: a) Bipolar and b) Unipolar. 53
4.30: Comparison of bipolar, strain vs. electric field plot of all tape-cast PMN-PT ceramics. 54
4.31: Comparison of unipolar, strain vs. electric field plot of all tape-cast ceramics. 55
4.32: Comparison of bipolar and unipolar strain vs. electric field plots of PMN-PT ceramics: a-b) undoped and c-d) 1% mole Mn doped. 56
4.33: Results of random sample at measured at 60kV/cm 2000ms i) Polarization vs. electric field ii) ΔT vs. temperature and iii) Pyroelectric coefficient vs. temperature plots. 58
4.34: Results of textured sample with 5% mole BT, sintered at 1150ºC for 4h, measured at 60kV/cm 2000ms i) Polarization vs. electric field ii) ΔT vs. temperature and iii) Pyroelectric coefficient vs. temperature plots. 59
4.35: Results of textured sample with 5% mole BT, sintered at 1200ºC for 4h, measured at 60kV/cm 2000ms i) Polarization vs. electric field ii) ΔT vs. temperature and iii) Pyroelectric coefficient vs. temperature plots. 60
4.36: Results of textured sample with 5% mole BT, sintered at 1200ºC for 8h, measured at 60kV/cm 2000ms i) Polarization vs. electric field ii) ΔT vs. temperature and iii) Pyroelectric coefficient vs. temperature plots. 61

4.37: Results of textured sample with 1% mole BT, measured at 60kV/cm 2000ms i) Polarization vs. electric field. 62

4.38: Results of undoped dry pressed sample, sintered at 1150ºC for 4h, measured at 60kV/cm 2000ms i) Polarization vs. electric field ii) ΔT vs. temperature and iii) Pyroelectric coefficient vs. temperature plots. 63

4.39: Results of 0.5% mole Mn doped dry pressed sample measured at 60kV/cm 1000ms i) Polarization vs. electric field ii) ΔT vs. temperature and iii) Pyroelectric coefficient vs. temperature plots. 64

4.40: Results of 1% mole Mn doped dry pressed sample measured at 60kV/cm 2000ms i) Polarization vs. electric field ii) ΔT vs. temperature and iii) Pyroelectric coefficient vs. temperature plots. 65

4.41: All samples P_{max} values vs. temperature plots. 66

4.42: Electrocaloric measurement results of textured 0.72PMN-0.28PT samples applied electric field, parallel and perpendicular to $<001>_{pc}$ directions. 67

LIST OF TABLES

Table Number:		**Page**
2.1:	Some materials values of ECE of PMN-PT samples.	23
3.1:	The content of PMN-PT powder.	29
4.1:	All tape-casting samples ε_r vs.T vs. tanδ values on plots.	51
4.2:	%Strain values of all tape-casting samples.	54
4.3:	ECE measurement values of all samples at 25ºC	66
4.4:	ECE measurement values of all samples at 90ºC.	66

1. INTRODUCTION

In recent years, ceramics fabricated with a crystallographic texture by preferentially orienting the grain in certain orientations, have attracted attention due to their superior properties that can complete with single crystals and commercia lead zirconate titanate [Pb (Zr,Ti)O_3 -PZT] without requiring an expensive infrastructure. In addition, using template grain growth and tape-casting methods, textured ceramics can be successfully produced.

In this study, the solid solution of lead magnesium niobate and lead titanate [(1-x)Pb($Mg_{1/3}Nb_{2/3}$)O_3-x$PbTiO_3$ (PMN-PT)] were chosen as the main component. The electrical properties of these ceramics vary in composition and temperature. In this study, x =0.28 was chosen and 0.72PMN-0.28PT composition was fabricated. 0.72PMN-0.28PT was obtained mainly by the tape-casting method and textured samples will be produced by the templated grain growth (TGG) method using $BaTiO_3$ and $SrTiO_3$ single crystal templates.

0.72PMN-0.28PT is in the rhombohedral phase at room temperature according to phase diagram of PMN-PT and it shows relaxor behavior. PMN-PT is used for different applications depending on the amount of PT in the structure. Morphotropic phase boundary compositions are used in piezoelectric transducer applications, while relaxor compositions are used as electrostrictive actuators. In this thesis, x = 0.28, one of the relaxor compositions of PMN-PT was examined for electrocaloric (ECE) application, one of the solid-state cooling methods. The effect of anisotropy created by texturing on the electrocaloric effect will be examined. Ceramics were produced as plates with a thickness of 500 μm and ECE measurements were taken by indirect method. The effect of anisotropy on the electrocaloric properties was reported for the first time in the literature.

1.1. Aim of The Study

The main purpose of this thesis is to investigate based on empirical knowledge of one of the new generation solid-state cooling systems called as electrocaloric refrigeration. The essential steps of the study steps of the study are as follows:

- The study was conducted to obtain It will be obtained appropriate composition, morphology, and grain size for 0.72PMN-0.28PT powder produced by solid-state calcination method.
- It was aimed to obtain textured ceramics with a thickness of 500 μm oriented in the direction of <001> combination by tape cast, and template grain growth (TGG) methods using templates.
- Another aimed of the study, to observe dopant element (Mn) effective in the PMN-PT ceramics structure and it is properties due to ferroelectrics, electrical, electrocaloric effect analyses.
- Ferroelectric, dielectric, electrical properties, and electrocaloric analysis of manufactured ceramic samples was done due to and it was investigated temperature depending on measurements to observe that how anisotropy in the structure of ceramic affected these properties.

2. LITERATURE REVIEW

2.1. Electroceramics

The word ceramics originally comes from the Greek word ‘keramos’ which a definition of pottery made of clay mixing with water, shaped while wet then dried, and fired in the 900ºC-1200ºC temperature range. During the ancient Greek ages, ceramic materials were used to store water and food, walls of oven, held molten metals. In time, pottery evolved to ceramic then to the advance ceramics due to improvement of ceramic-based research in the electrical industry [1].

Electroceramics are trending and promising materials for todays and future scientific research, devices, and applications. Due to their unique dielectric, piezoelectric, ferroelectric, pyroelectric, ferromagnetic, ionically conducting, electronically and superconducting properties. According to changes of material-based research, electroceramics research has become a more multidisciplinary field. Thus, the materials science studies can be separated into three fundamental notions.

- Different types of materials co-relation with each other,
- The exhaustive theorical studies of materials and their component,
- The investigation of materials in nano size using nanotechnology [2].

These three areas will be an essential point for future investigation of electroceramics and can take more attention to discover the paradigm of new applications.

The addition and substitution of alternative cation can enhance the properties of ferroelectrics and lead to remarkable changes by adjusting the below factors:

- Change the Curie and transition temperature; the Curie temperature change is important for permittivity peak level. Therefore, both substitution of Sr^{2+}, Ba^{2+} decreased the substitution of Pb increased the Curie temperature as shown in Figure 2.2.
- Limit the motion of domain wall; To avoid domain wall motion, transition ions such as Fe^{3+}, Ni^{2+}, Co^{3+} taken place of Ti^{4+} in the material structure.

- Introduce compositional heterogeneity or second phases; The addition of the intersection compound like $CaZrO_3$, $BaTiO_3$ effect extend of the permittivity temperature peak, because of this, the Curie point converted to a wider level of the range.
- Manage the size of crystallites; Commonly, cation ions have higher valency than replaced ions. To obtain crystal growth, La^{3+} replaced Ba^{2+} or Nb^{5+} replaced Ti^{4+}. As a result of this notion, the permittivity level increase under the Curie point.
- Control the content of oxygen and the valency of the Ti ion; Commonly, cation ions have higher valency than replaced ions. To obtain crystal growth, La^{3+} replaced Ba^{2+} or Nb^{5+} replaced Ti^{4+}. As a result of this notion, the permittivity level increase under the Curie point.

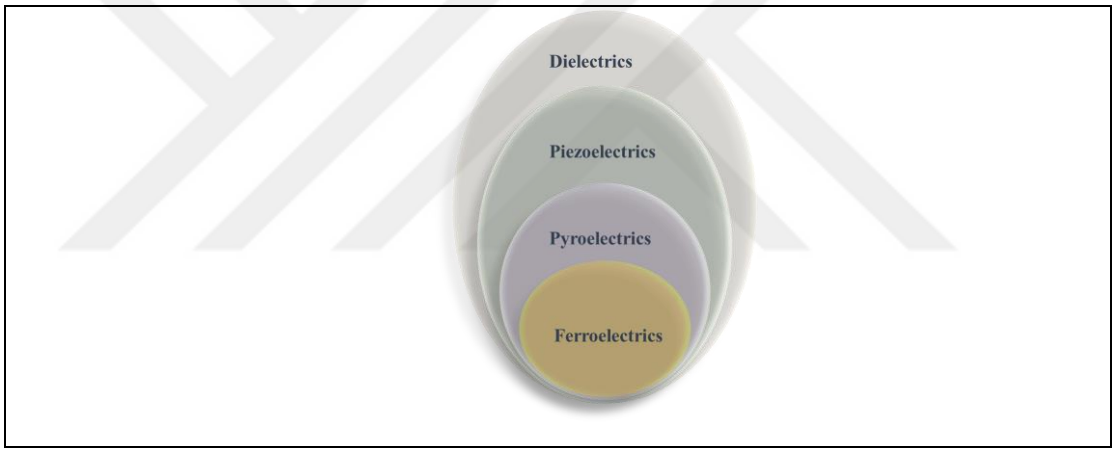

Figure 2.1. Relationships between dielectric, piezoelectric, pyroelectric, and ferroelectric materials.

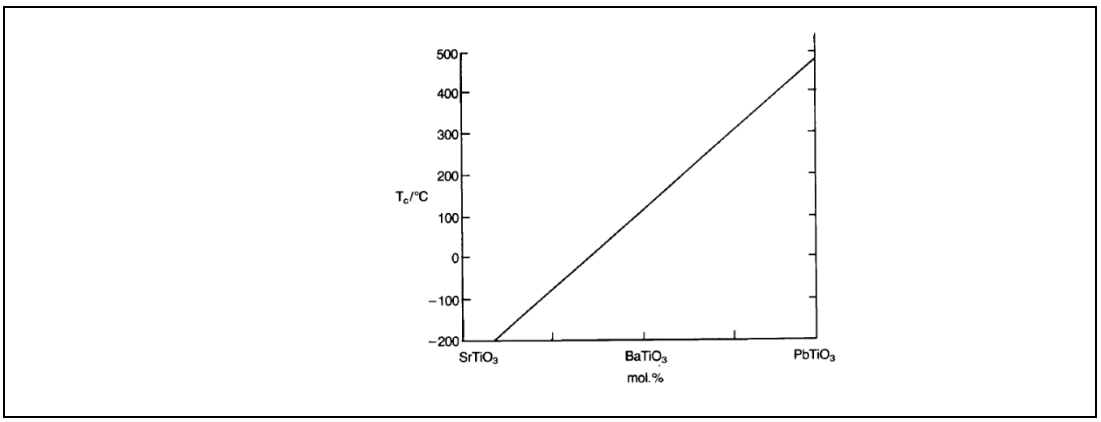

Figure 2.2. The plot of substitutions effect on Curie temperature.

As seen in Figure 2.1 dielectrics is a big title of ferroeectric ceramic based materials.And the separation of electroceramics can be derived into four titles as dielectrics, piezoelectrics, pyroelectrics, and ferroelectrics materials.

2.2. Piezoelectrics

The piezoelectric property emerged in 1880 when the Pierre and Jacques Curie's brothers discovered that some materials create electric charges on their surfaces under applied mechanical stress. This discovered property which named as piezoelectric effect. On the contrary, it was suggested by the Curie brothers that these materials under electric field should form mechanical strain, and Gabrial Lippmann experimentally improved this in his work in 1881. Thus, the mechanical force of the material under the electric field is called the reverse piezoelectric effect and shown in Figure 2.3 as Heckmann diagram showed the relation between mechanical and electrical properties of solids. Materials showing these properties are also called piezoelectric materials [4,5]. The piezoelectric effect is the formation of electric dipole because of the applied stress. In most classes of non-center of symmetry crystals in which moments can be induced arises. In this case, all ferroelectric materials are polarized in their crystal lattice. Due to their structure, they exhibit piezoelectric properties. According to the Neumann principle, symmetry of any physical property of the crystal, the point group of that crystal must include symmetry shown in Figure 2.4. Direct piezoelectric effect, switching the dipole moment due to the compression and tensile stress that occur in the polarized material, and an electrical potential difference occurs with the accumulation of charge on the surface. Converse piezoelectric effect, the electrical field in the crystal causing a change in volume [5,6, 7, 8].

$$D_i = d_{ijk} x_{jk} + \varepsilon_{ij}^{T} E_j \tag{2.1}$$

$$\mathrm{x_{ij}} = \mathrm{d_{ijk}} \mathrm{E_k} + S_{\mathrm{ijkl}}^{\mathrm{E}} \mathrm{X_{kl}} \tag{2.2}$$

Where $D_i$is electric displacement (C/m^2), E_k is electric field component (V/m), x_{ij} is strain component, d_{ijk} is component of the piezoelectric charge or strain constant, X_{jk}

is stress component (N/m^2).

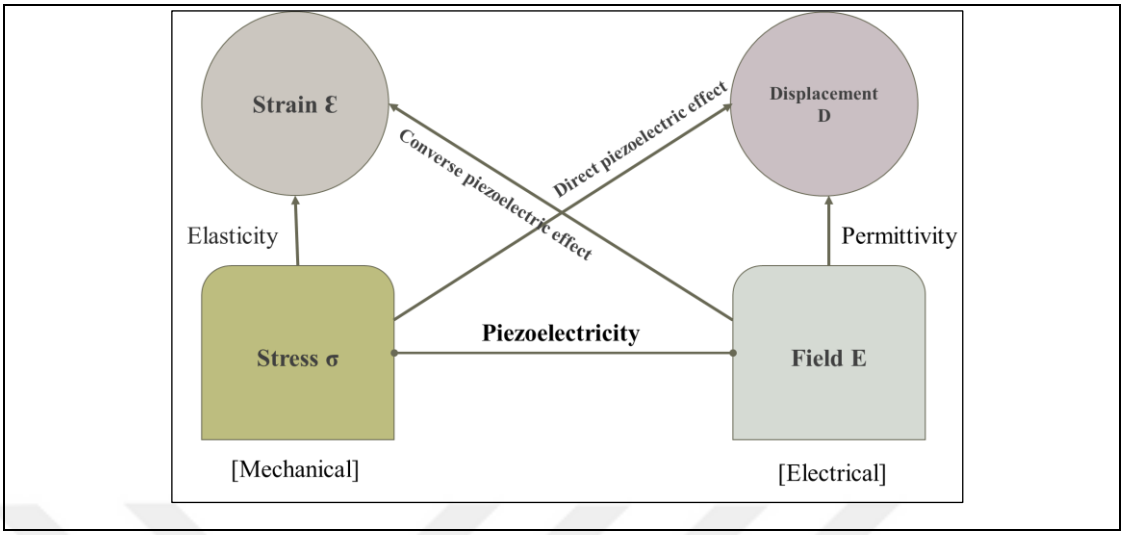

Figure 2.3: Heckmann diagram.

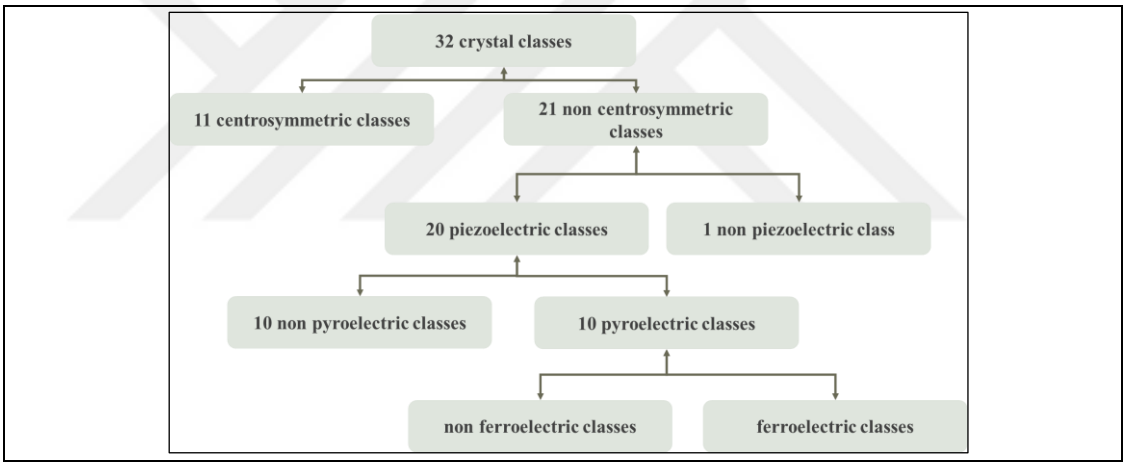

Figure 2.4: Schematic illustration of 32 crystal groups.

The piezoelectric effect is helpful within many applications that relate to the production of ceramic devices and sound detection, generation of high voltages or electronic frequency, micro-balance, and the ultra-fine focusing of optical assemblies. Due to being studied for decades, additionally, they have become the fundamental part of scientific instruments and instrumental techniques with atomic scale, such as Atomic Force Microscopes and Scanning Tunnelling Microscopes. They are worldwide spread that they are used even in very common applications. In the scientific domain, the most common usages they are most used in sensors and actuators [4].

2.3. Ferroelectrics

In 1920, the ferroelectric terminology was discovered in Rochelle salt by Valasek with the first hysteresis loop of a ferroelectric material and shown that permanent polarization is the natural notion of it. In 1940, it was discovered that barium titanate ($BaTiO_3$) has ferroelectricity. After that, during the 1950s, lead based (PZT) ceramics milestone for ferroelectric research. The studies of binary systems obviously demonstrated that phase transitions are important for compositional induced related morphotropic phase boundary (MPB) base research. Then during the 1980s-1990s, the relaxor-$PbTiO_3$ (relaxor PT) ferroelectric was discovered that it showed piezoelectric effect that is 3-10 times larger than conventional piezoelectric ceramics. Lastly, relaxor-PT ceramics in cubic perovskite structure in paraelectric phase can change during ferroelectric state into rhombohedral, monoclinic, orthorhombic, or tetragonal microstructure due to PT content and polling effect has high piezoelectric coefficient and high electromechanical coupling factors [9].

Piezoelectric materials have had rich research background depending on the investigations and utilization of a novel, increasingly promising piezoelectric composites. They focus on the property of these materials having spontaneous electric polarization that can be reversed, called ferroelectricity. Ferroelectric property has been seen in dielectric materials that do not have central symmetry in 32-point symmetry group. The spontaneous polarization (P_s), shown in Figure 2.5, can be reoriented by an external electric field (E), resulting in polarization P_r, and coercive field (E_c) can be identified, shown in Figure 2.6 and Figure 2.7.a. Additionally, spontaneous polarization provides an internal bias to the ferroelectric resulting in the loss of central-symmetry and a large piezoelectric strain Ɛ,

$$\varepsilon = Q(P_s + xE)^2 \approx QP_s + 2QxP_sE \tag{2.3}$$

where the first term is quadratic electrostrictive strain, and the second term is linear piezoelectric strain; Q and x are electrostrictive coefficient and dielectric susceptibility, respectively. Equation 2.3 offers that large spontaneous polarization and dielectric susceptibility can lead to a large piezoelectric effect. This statement be

supported with empirical results to why good ferroelectrics are generally good piezoelectric as well [6,7,8].

Ferroelectrics generally exhibits separate regions called domains that have different spontaneous polarization directions. For each domain the polarization state is uniform, so the ferroelectric domain is described as a cluster of individual unit cells that are oriented in the same direction. In each domain, the split from each other depends on orientation direction by domain walls, as seen Figure 2.8. Domains can be re-oriented by an external electric field.

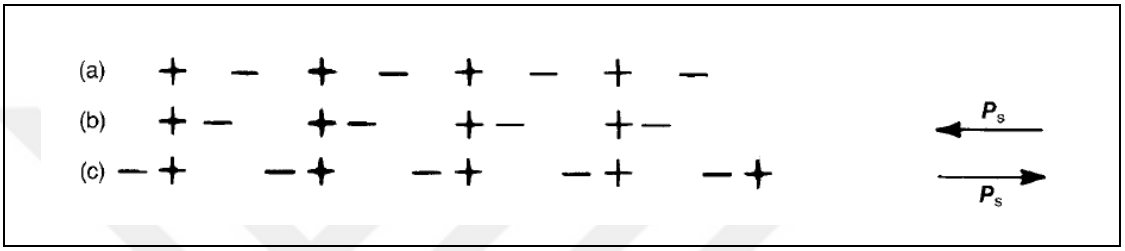

Figure 2.5 a) non-polar alignment, b-c) polar alignment. The arrows show the direction of Ps.

For ferroelectric ceramics unipolar mode is driven to avoid the case of mechanical stresses due to domain reorientation while maximizing the strain output. Nevertheless, the switching between remnant polarization states because of domain re-orientation is the fundamental feature for data storage applications that are driven in bipolar mode. Self-polarity and electric field observed in the ferroelectric materials and the effective hysteresis curve exist within a certain temperature range. The highest limit temperature point at which it can be observed is name as the Curie temperature (T_c) is named. Above this temperature, the ferroelectric property is lost, the materials behave as normal dielectric materials; this phenomenon is called paraelectric. Close to the curie temperature value in these regions, the dielectric permittivity level is very high, and generally above this temperature value ferroelectric material is nonpolar. The structural phase transition was occurring then the material became non-polar, and the spontaneous polarization disappears, dielectric constant (ε) exhibits irregularity around the phase transition, as described by the Curie-Weiss Law shown in Equation 2.4 [9,10,11,12]:

$$\varepsilon = \varepsilon_0 + \frac{c}{T - T_0} \approx \frac{c}{T - T_0} \tag{2.4}$$

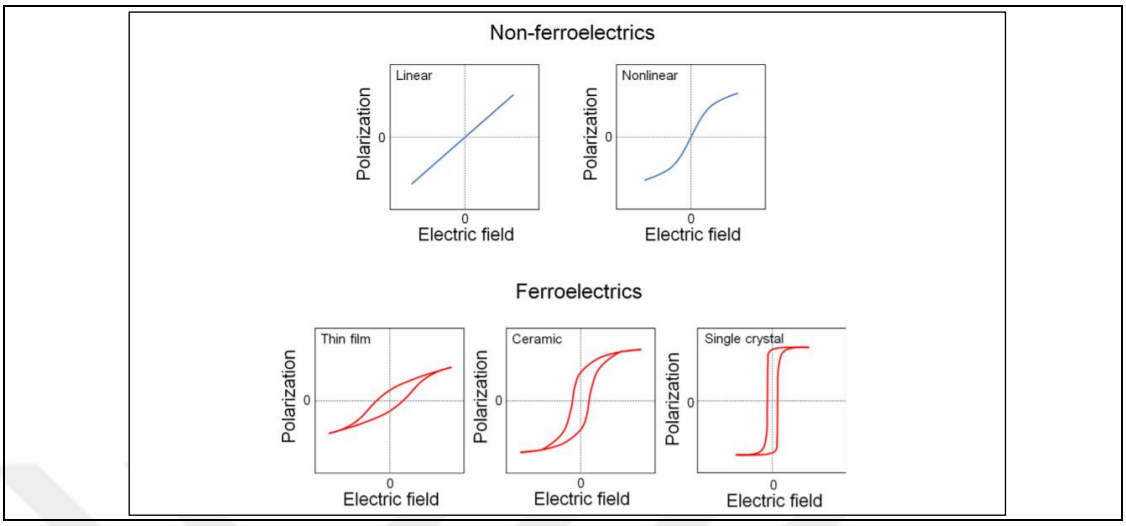

Figure 2.6: Plots belong to different type of materials.

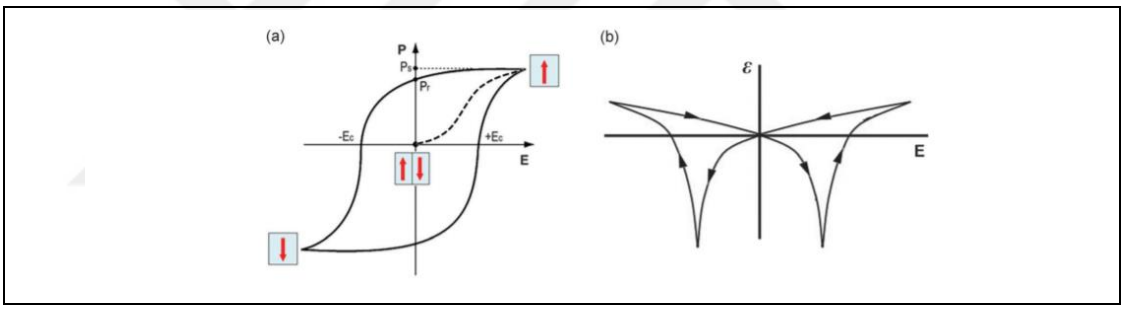

Figure 2.7: a)Ferroelectric hysteresis and b) butterfly loops.

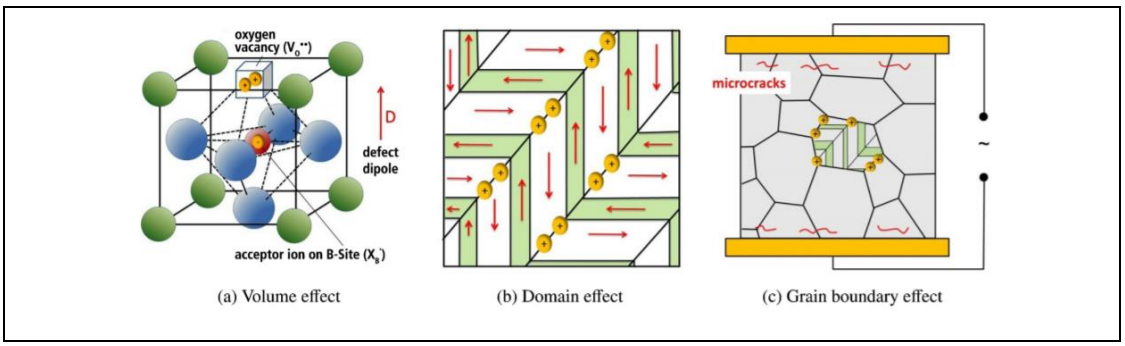

Figure 2.8. Schematic illustration of different domain stabilization modality due to lenght scales of microstructure.

2.3.1. Relaxor Ferroelectrics

Relaxors exhibit uncommonly broad dielectric constant within an extensive temperature range (~100 K) highly depending on the frequency. The results are an essential reason focus on solid-state physics. PMN has local polar nano regions (PNR) and a chemically ordering region (COR) with the size of several nm scales as an inhomogeneity in crystal, shown in Figure 2.10. PNR and COR belong to different symmetry groups and are considered to have non-centrosymmetric symmetry R3*m*, and centrosymmetric symmetry F*m*3*m*, respectively. As a result of this structure, there is spontaneous polarization P*s* along the ‹111›$_c$ direction of structure in PNRs, but there is no P*s* in CORs as shown in Figure 2.10. Besides chemical and structural inhomogeneities, there are ferroelectric domain structure inhomogeneities exist. The reason behind relaxor behavior has conjectured of depicted multiple inhomogeneities in above [11,12].

PMN -Pb $(Mg_{2/3}Nb_{2/3})O_3$ was the first relaxor ferroelectrics material that has found by Smolenskii and Agranovskaya in 1959. With the unique polar state of PMN, high electrostrictive and piezoelectric properties relaxor ferroelectrics quite different from classical ferroelectrics, especially PMN-PT and PZN $[Pb(Zn_{1/3}Nb_{2/3})O_3]$-PT solid solution systems. Polar nano regions (PNRs) are considered as an important point for developing dielectric and piezoelectric properties of relaxor-based ferroelectrics to Pb $(B^IB^{II})O_3$-PT than classical ferroelectrics, their excessively dynamic and delicate to an external stimulus. Even so, despite constant research related to Pb $(B^IB^{II})O_3$-PT based relaxor ferroelectric, the notion of how their nature benefits the electromechanical properties has not been studied too properly. After all, there is no exact definition to describe relaxor ferroelectrics [11,12].

Relaxors behavior basically can be explained in 3 states.

State 1; Relaxors own a high dielectric permittivity over a wider temperature range when compared to normal ferroelectrics, the near regions around T_c shown in Figure 2.10. The reason of it assumed that several nano-sized regions' absence was helpful to the switching of polar regions or vibrating of the interphase boundary between polar and nonpolar regions. Relaxors which belong to state 1, can be used for multilayer ceramic capacitor which are a part of electronic devices and circuits because of the high-level permittivity at the broad range temperature. One of the important

points is the minimal remnant polarization observed in relaxor ferroelectrics, the essential reason of it, during the applied external electric field to the relaxor, there is no macroscopic scale domain switching. Therefore, relaxors are promising materials for different types of capacitor applications, consumer electronics, pulsed power applications, and energy harvesting systems. The electromechanical properties with high-level dielectric permittivity can lead to large electrostrictive strain in relaxors expressed in Equation 2.5:

$$S_{33}(E_0) = Q_{33}[P_3(E_0)]^2 = Q_{33}\left[\int_0^{E_0} \varepsilon_{33}(E)\, dE\right]^2 \tag{2.5}$$

$S_{33}(E_0)$ is the applied electric field electrostrictive strain; $\varepsilon_{33}(E)$ is the dielectric permittivity, $P_3(E_0)$ is the polarization under an electric field with amplitude E_0 and Q_{33} is the electrostrictive coefficient, showing minimal dependence on the electric field. Relaxors have multiple advantages compared to PZT ceramics. PZT ceramics with fine grain size (‹1μm) have the fact that grain boundaries avoid the contribution of domain wall motion to polarization and strain. But relaxor ferroelectrics can show large electrostrictive strains shown in Figure 2.9.b-e., because of having smaller polar-regions whose sizes are above 10 nm.

State 2; State 2 relaxor ferroelectrics exhibit the most obvious dielectric behaviors. They show typical PE hysteresis loops and electric-field strain curves. Besides that, state 2, cannot show strong and time-stable remnant polarization, therefore, there is no high small-signal piezoelectric coefficient. Nevertheless, within domain wall motion and applied electric field to the reaxors nonpolar to polar state phase transitions was occurred, state 2 exhibits E-field induced strain behavior, large hysteresis, and nonlinearity. Thus, state 2 relaxor ferroelectrics are not eligible for piezoelectric applications. State 2 relaxor ferroelectrics are eligible for some applications which nonlinearity can be neglectable. Instance, solid-state cooling systems applications, air-conditioning, household refrigerator materials with electrocaloric effect is useful than classical vapor compression cycle systems. Electrocaloric systems have been actively studied because of large entropy change and/or phase transition due to applied temperature and electric field. Additionally,

relaxor ferroelectrics exhibit high piezoelectric effect bias electric field (d_{33} ≈1200 pC/N)

State 3; Piezoelectric properties can be achieved by poling thus obtaining long range ferroelectric domains and high remnant polarization. For ferroelectrics piezoelectric behavior is explained by coefficient d_{33}.

$$d_{33} = 2Q_{33}P_r\varepsilon_{33} \tag{2.6}$$

where Q_{33} is the electrostrictive coefficient, P_r is the remnant polarization, ε_{33} is dielectric permittivity. Usually, high piezoelectric properties of ferroelectrics are observed around morphotropic phase boundary compositions shown in Figure 2.13.a. Where ferroelectrics include flat energy landscape connecting two or more ferroelectric phase, under electric field leading to ease polarization. Relaxor-PT's exhibit higher piezoelectric coefficient and strains compared to the classical ferroelectric solid solution shown in Figure 2.9.d-e because all of them are with MPB composition. Additionally, can be affected by other factors such as Curie temperature, grain, and domain size, etc. Nevertheless, the long-range ferroelectric phases transition is always the dominant contributor to the high piezoelectricity, and nanoscale local structural heterogeneity is a key factor in relaxor ferroelectrics that benefit their piezoelectric properties.

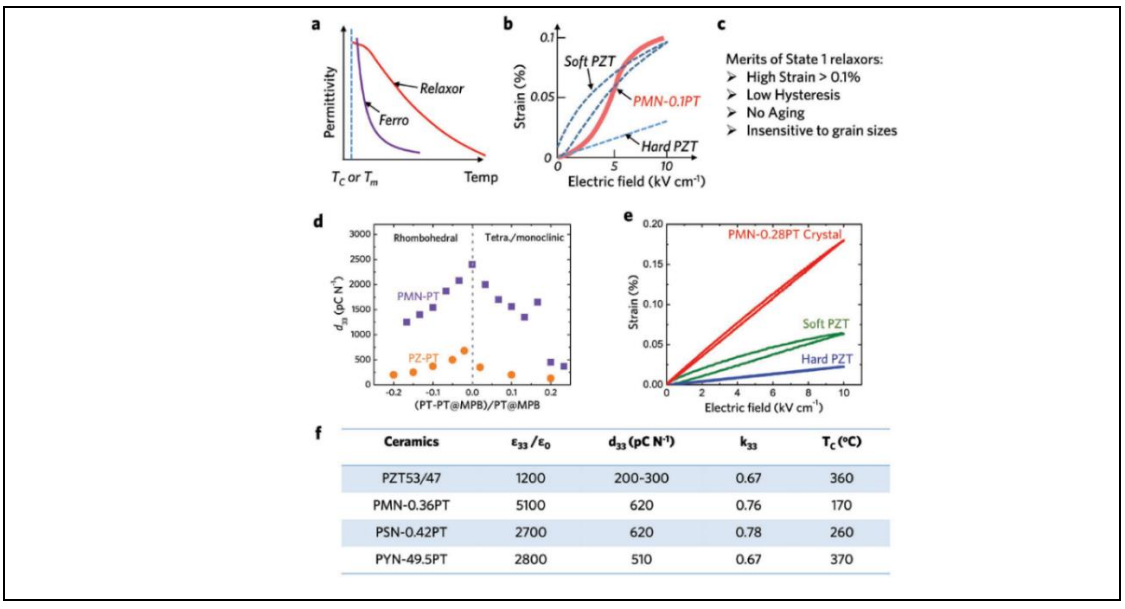

Ceramics	$\varepsilon_{33}/\varepsilon_0$	d_{33} (pC N^{-1})	k_{33}	T_C (°C)
PZT53/47	1200	200-300	0.67	360
PMN-0.36PT	5100	620	0.76	170
PSN-0.42PT	2700	620	0.78	260
PYN-49.5PT	2800	510	0.67	370

Figure 2.9: Plots belong to ferroelectrics and relaxor ferroelectric materials.

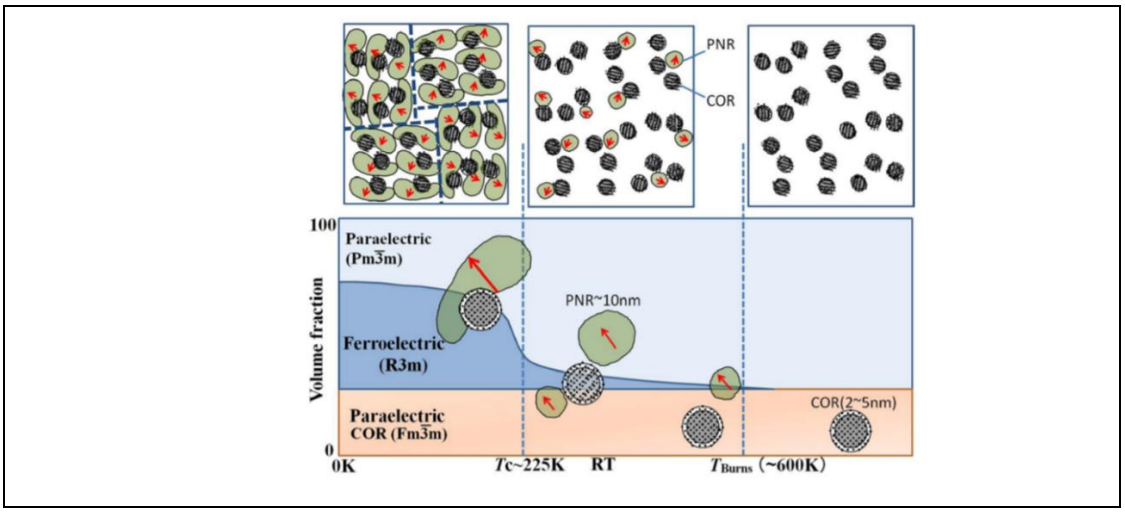

Figure 2.10: Schematic illustration of temperature dependence of PMN relaxor's nano-regions.

2.3.2. Perovskite Structure

L.A. Perovski who is a mineralogist from Russia has firstly characterized the structure of calcium titanium oxide ($CaTiO_3$) in the literature as chemical formula ABX_3 perovskite material structure shown in Figure 2.11 and their usage evolution depend on time, shown in Figure 2.12. Description of ABX_3 formula, where is A as a cation with large ionic radius, B as a metal cation, and X as an anion; as same as the crystallographic structure with $CaTiO_3$. Another short specification of the perovskite structure is exhibited AX_{12} cuboctahedron that shares its edges with a BX_6 octahedron, as shown in Figure 2.13.b. The oxide perovskite has an eligible structure to obtain desirable and adjustable properties due to it is stable energy level and is flexible to structurally accommodate lots of elements in the structure.

Most ferroelectric materials have some deformations of the perovskite structure shown in Figure 2.14 shows the representation of the ABO_3 perovskite structure. Cubic in perovskites, the larger cation (eg Pb^{2+}, Ba^{2+}, Sr^{2+}, Bi^{3+} or Na^{+}) is relative to oxygen, It is 12-fold coordinated. Smaller cation (eg Ti^{4+}, Zr^{4+}, Nb^{5+}, Zn^{2+}, Mg^{2+}) with oxygen octahedral is chordinal. Oxygen has six coordination with its B neighbor on both sides. and with its four more distant neighbors A, distortion occurs [8]. Perovskite crystal structure, R_A, R_B, and RO in its composition are perfect. If it is assumed to be a sphere, Equation 2.7., is valid for the perfect the perovskite structure. Provided that the tolerance factor (t) is in the range of $0.9<t<1.1$ in perovskite structure, perovskite the

structure is stable. In ferroelectrics, if the t value is greater than 1, the structure is usually tetragonal, if the tolerance factor is less than 1, it is rhombohedral shown in Figure 2.14 decompositions are observed [13,14].

$$t = \frac{R_A + R_0}{\sqrt{2}(R_b + R_0)} = 1 \tag{2.7}$$

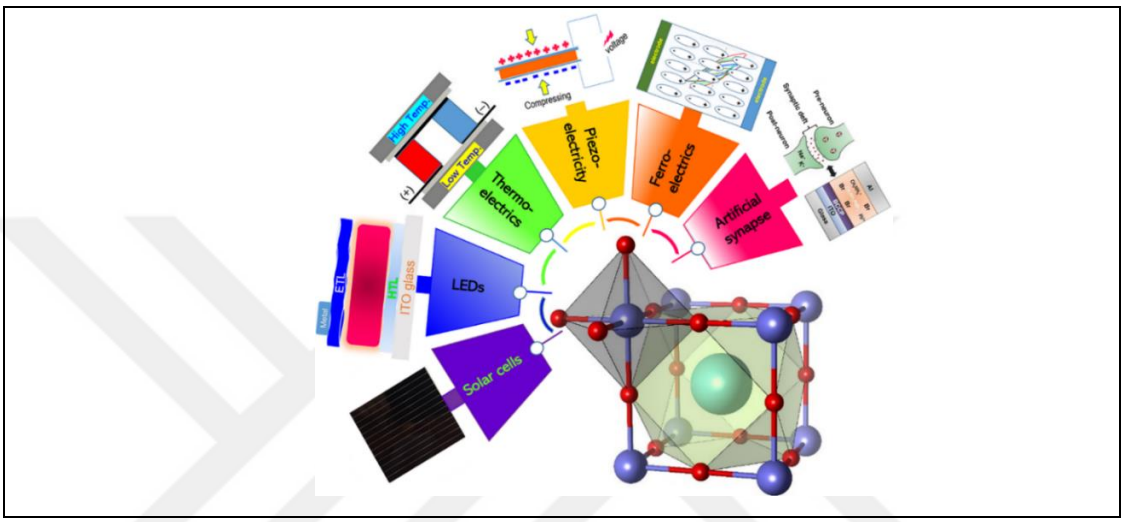

Figure 2.11: Schematic illustration of perovskite structure**.**

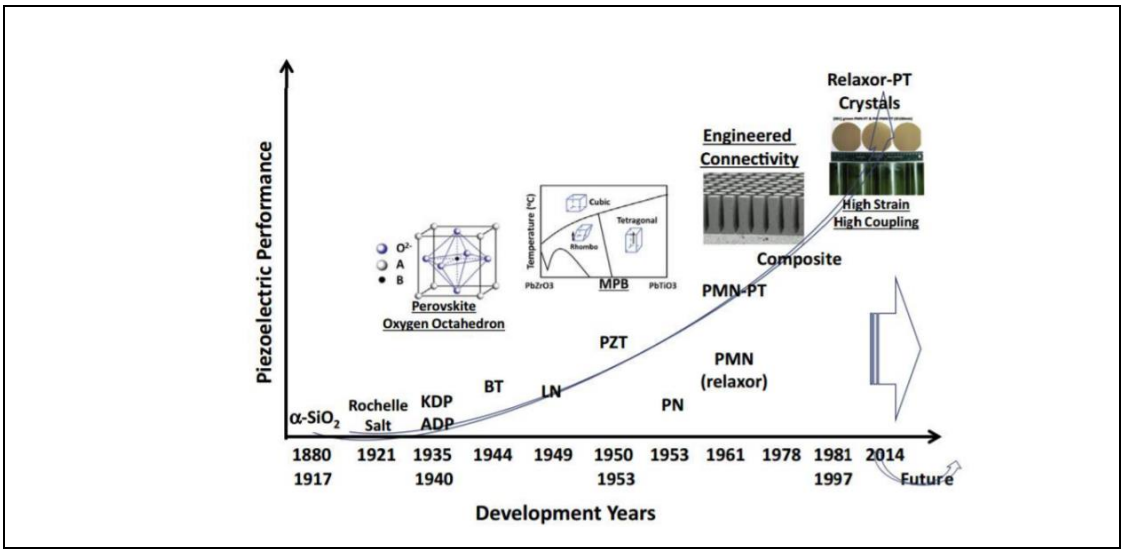

Figure 2.12: Piezoelectric materials development depend on years.

2.3.3. PMN-PT Solid Solution

Lead magnesium niobate Pb ($Mg_{1/3}Nb_{2/3}$) O_3 or (PMN) was first synthesized in the late 1950s. Relaxor PMN, which is a photoelectric prototype, has a different phase transition around 105ºC. PMN based relaxor exhibits maximum dielectric constant. Ferroelectrics are promising for transducer applications. These ceramics, it is predominantly in paraelectric phase at above curie temperature (T_c) and has high dimensional control. It is obtained by the quadratic electrostrictive effect. Stable ferroelectric domain structures dimensional creep and dimensional creep of traditional polar piezoelectric ceramics repetition (aging and aging effect) problems are largely eliminated has been removed. PMN with perovskite structure is randomly formed by Mg^{2+} and Nb^{5+} ions at B position containing the arrangement of and as previously mentioned disordered perovskite. Dielectric properties of PMN-[$Pb(Mg_{1/3}Nb_{2/3})O_3$]with the addition of PT-$PbTiO_3$ can be developed. Curie temperatures of PT and PMN are 490 ºC and -10 ºC, respectively. Thus, the T_c value of PMN-PT increases with PT content, as shown in Figure 2.15, it shows that how PT content level effected dielectric properties of PMN-PT. (1-x) $Pb(Mg_{1/3}Nb_{2/3})O_3$–$xPbTiO_3$(PMN-PT) binary solid solution system of PT, multilayer ceramic capacitor, actuators, smart materials and devices. Excellent dielectric and electromechanical properties with applicability potential has been studied extensively. In the PMN-PT solid solution system, with PT ratio 30-35% (T=25ºC), there is a gap between the rhombohedral-tetragonal ferroelectric phase boundary. It has a morphotropic phase boundary (MPB) the phase diagram of (1-x) PMN-x PT system is shown in Figure 2.13.a. MPB compositions have two equivalent energy states, because of the relation rhombohedral and tetragonal between, it then allows the re orientation of domain, it exhibits high dielectric and piezoelectric properties [12,17].

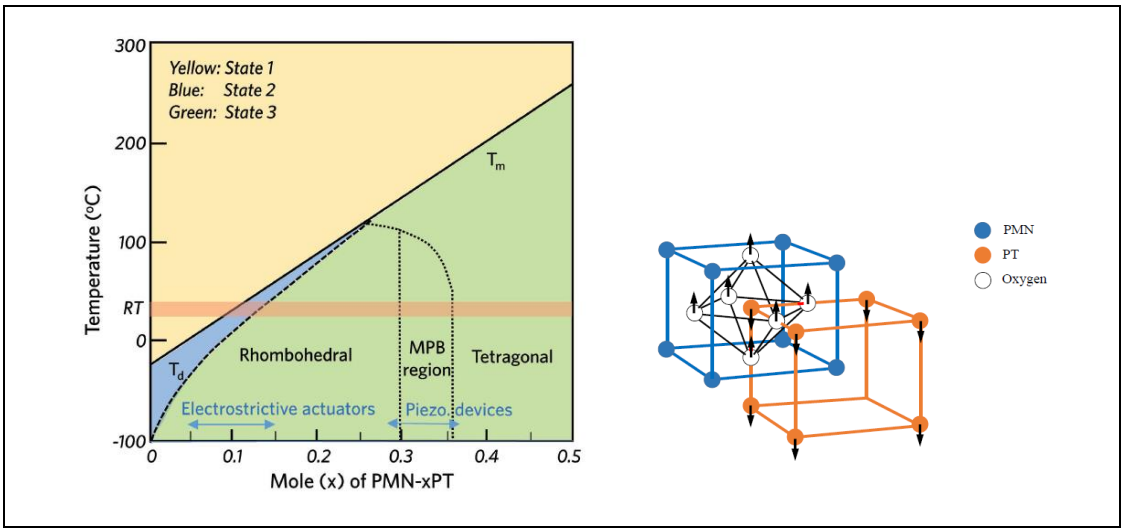

Figure 2.13: a) Phase diagram of the (1-x) PMN-x PT relaxor ferroelectric system with application types. b) PMN-PT detailed crystal structure.

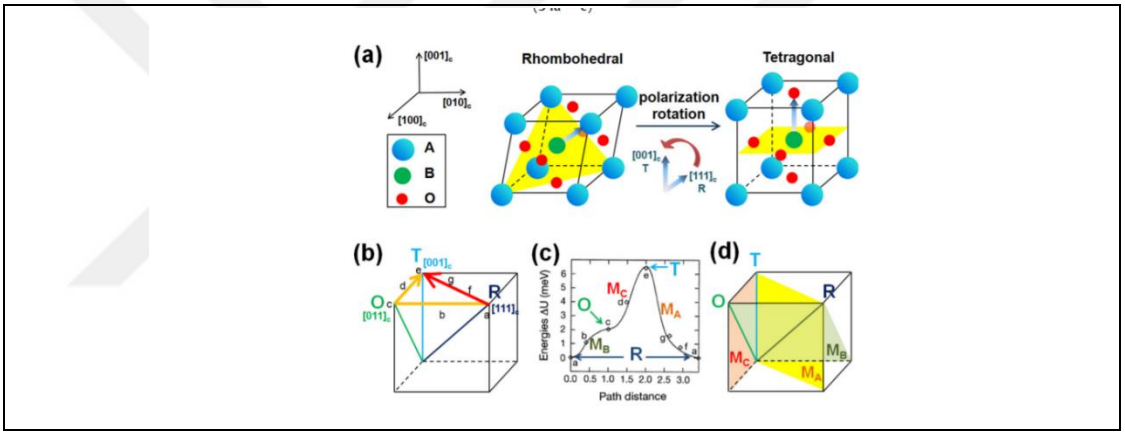

Figure 2.14:Schematic illustration of perovskite unit cell due to polarization rotation.

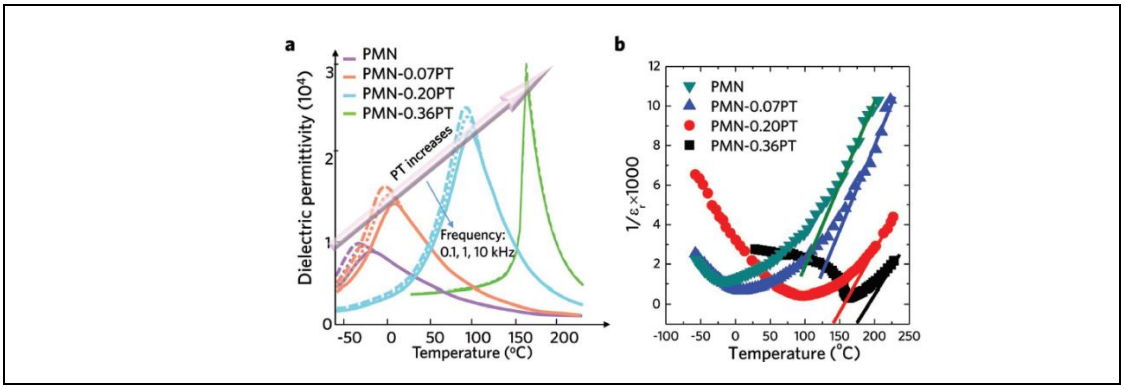

Figure 2.15: Dielectric permittivity vs. temperature plots as a function of PT content.

2.4. Caloric Effect

The caloric effect is thermal changes when magnetic, electric, and mechanical (uniaxial or isotropic) applied field occurs magnetically, electrically, and mechanically response. The adiabatic temperature change (ΔT), isothermal entropy change (ΔS), and isothermal heat (Q) are among the thermal changes' above. Conventional caloric materials exhibit ΔT >, ΔS<0, Q<0. Inverse caloric materials exhibit ΔT<, ΔS >, Q >, respectively when the applied variable level is increased. The caloric effect is mainly separated into three headings depending on the applied field type. Those are magnetocaloric (MC), electrocaloric (EC), and mechanocaloric (mC) effects, applied by changes in the magnetic field (H), the electric field (E), and the stress field (σ), respectively shown in Figure 2.16 [16].

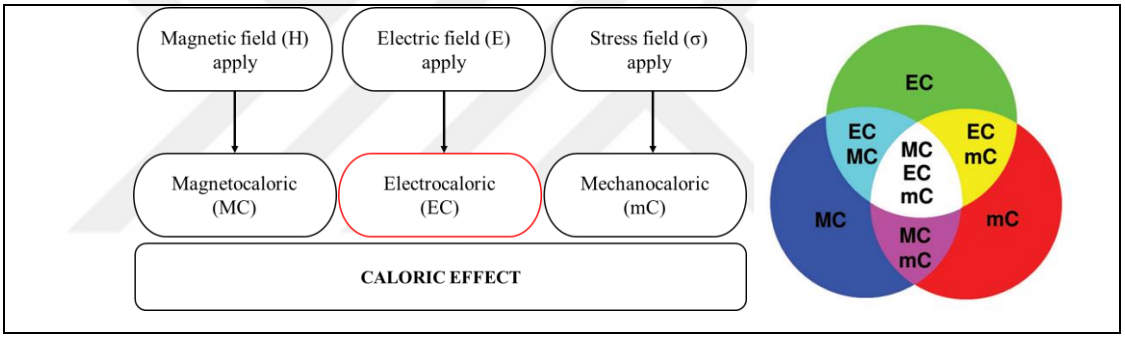

Figure 2.16: Shematic illustration of various Caloric Eeffect and their corelation between each other.

Theoretically, any material that will be exposed to an adiabatic stimulus can produce a reversible entropy changes at phase transitions. Above Curie temperature (T_c) some materials become paraelectric or paramagnetic which means there is no long-range dipolar or magnetic ordering. In reversible phase transititon material goes from low entropy level (ordered) to high-level entropy (disorder) state with interrelating thermal changes. The caloric effect is common among ferroic perovskite oxides that show solid-state phase transition. During the phase transition, several phases can stay in equilibrium level with the same free energy level, the system permitting to overcome zero energy obstacles. Adjacent to the phase transitions region, perovskite structure can have large thermal changes, this can cause caloric effect. Origin of the caloric effect comes from vibrations of lattice (phonons), electronic

excitations, magnetic, or dipolar ordering, these factors can cause symmetry in the perovskite structure [16,17].

2.4.1. Electrocaloric Effect

From the early stage of history, it has been known that heat affects material properties in different ways. Pyroelectric is one of the phenomena that results from applied temperature to the materials, discovered by Theophrastus in the fourth century B.C. Dielectric materials which have a unique axis of symmetry and lack center symmetry at the same time in their structure show a spontaneous polarization (*Ps*) and will exhibit a pyroelectric effect (PE) depending on applied temperature caused changes in Ps. The variations in Ps along the surface can produce a net voltage across the dielectric. With the attachment between both surfaces with the external circuit, a current can flow along with the surface's charge. The asset of an induced electric field or induced stress, the pyroelectric coefficient p(T) is defined as a change of spontaneous polarization with temperature as $p(T)=dP_s/dT$, and A is surface area. The short-circuit pyroelectric current i_p is;

$$i_P = A\, p(T) \frac{dT}{dt} \tag{2.8}$$

The opposite term of pyroelectric effect is called the electrocaloric effect. The basic description of EC is due to applied electric field cause changes of temperature and entropy in the material structure. For some reason it is hard to explain than PE. These two notions have rising interest lately years, they are related to each other, as seen Figure 2.17 as relationship between pyroelectric effect and electrocaloric effect in Heckman diagram. PE for recovery of electrical energy from waste heat, ECE for new design cooling system to avoid the use of liquid refrigerants [16,17,18].

Solid-state refrigeration based on electrocaloric effect (ECE) has been studied with high interest from early stage of history, as seen in Figure 2.20 the ECE usage depend on time.

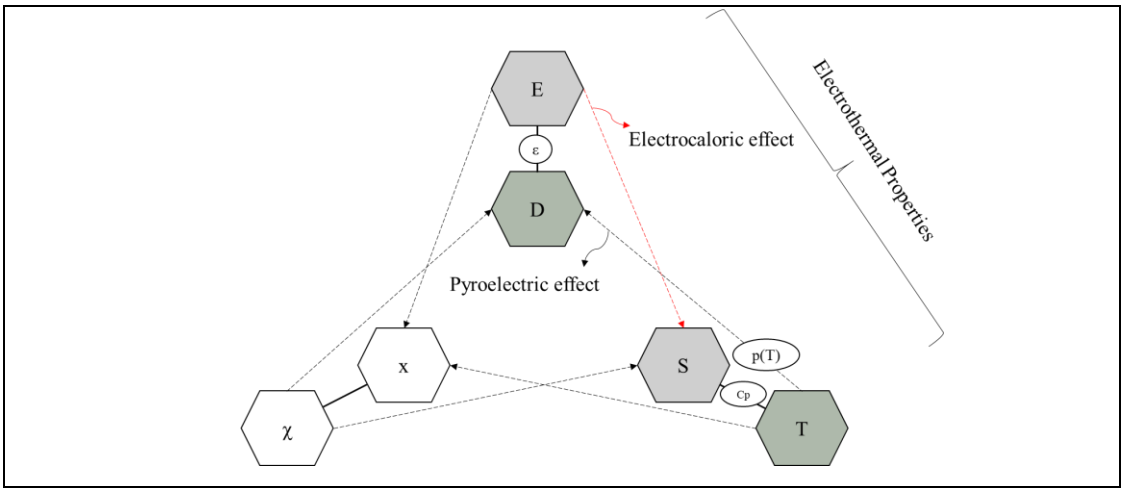

Figure 2.17: Electrothermal properties, applied forces and their response relationship on the Heckmann diagram.

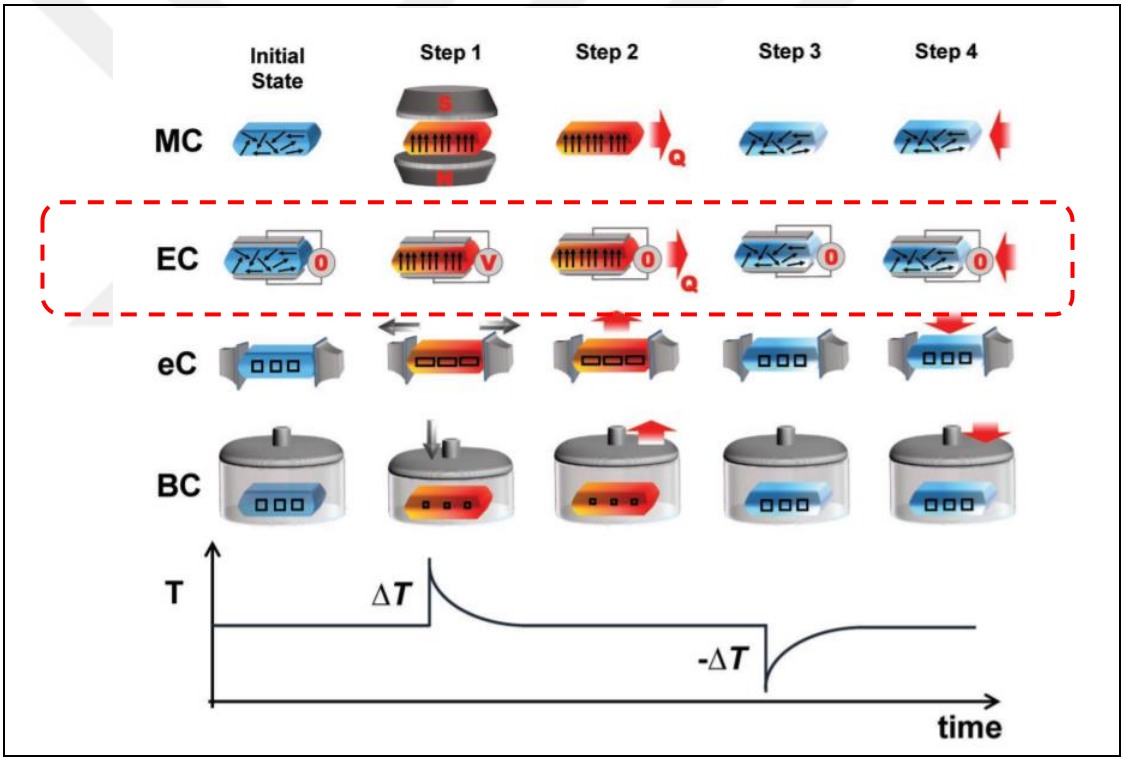

Figure 2.18: Temperature vs. time plot depend on caloric effect, (EC: electrocaloric).

The explanation of any caloric system's working principle can be separated into the four steps shown in Figure 2.18 and Figure 2.19. The initial step of the cycle is the adiabatic applied field type (magnetic, electric, stress, or pressure) changes. In conventional or reverse caloric materials, depending on polarization (EC effect), the phase transition occurred in the caloric materials for hence the entropy changed which increased or decreased its temperature. In the second step, the heat depends on the

caloric effect is rejected or absorbed to an external reservoir by a heat transfer process. In the third step, the adiabatic polarization releasing or relaxing development of decreasing or increasing depends on temperature changes. In the final step, caloric material heat soaks in from the cold reservoir, which became colder until it returns to initial step of the cycle to intergrate the cycle. Multicaloric refrigeration might have various thermodynamic cycles to enhancement cooling efficiency by empowering the application. Nevertheless, there is still mysterious and insufficient information about the caloric effect and its technologies [16,17].

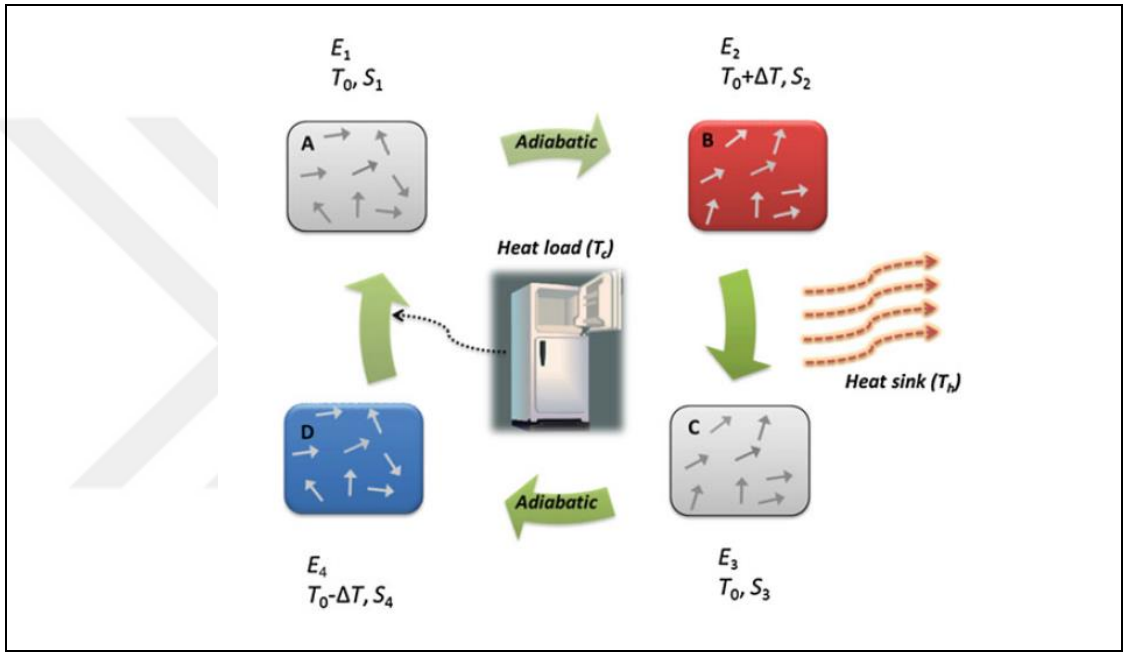

Figure 2.19: Illustration of ECE cooling system working principle.

Adiabatic depolarization (from A to B): With the rapid increase of applied electric field on the isolated electrocaloric material from the level of E_1 to E_2, as a result of holding dipoles. As a result of this, refrigerant entropy and heat capacity decreased from S_1 to S_2, the temperature of material increased ($T_0+\Delta T$) if there is no heat loss because refrigerant is isolated [19].

Heat transfer (from B to C): Between refrigerant and hot reservoir possessed thermal contact each other, During applied electric field reducing from the level of E_3 to E_4 during electric field changed from E_2 to E_3 to kept in constant level of refrigerant temperature. Then the heat is ejected from the refrigerant to the heat reservoir. The ejected heat is given by $Q = T_h \Delta S_h$ where $\Delta S_h = S_3 - S_2$ [19].

Adiabatic depolarizing (from C to D): During electric field decreasing from the level of E_3 to E_4, the heat is again isolated by electrocaloric material from the heat reservoir. Due to refrigerant entropy and heat capacity level increased the electric dipoles became unconstrained. When electrocaloric material is isolated from surrounding materials (adiabatic conditions), there is no heat exchange observed, therefore, the refrigerant temperature decreases ($T_0 - \Delta T$) [19].

Entropy transfer (from D to A): Heat transfer occurred from a cold reservoir to refrigerant because of their connection, the temperature cooled down to T_c. The electrocaloric material absorbed the heat from the cold reservoir as given by $Q = T_c \Delta S_c$ [19].

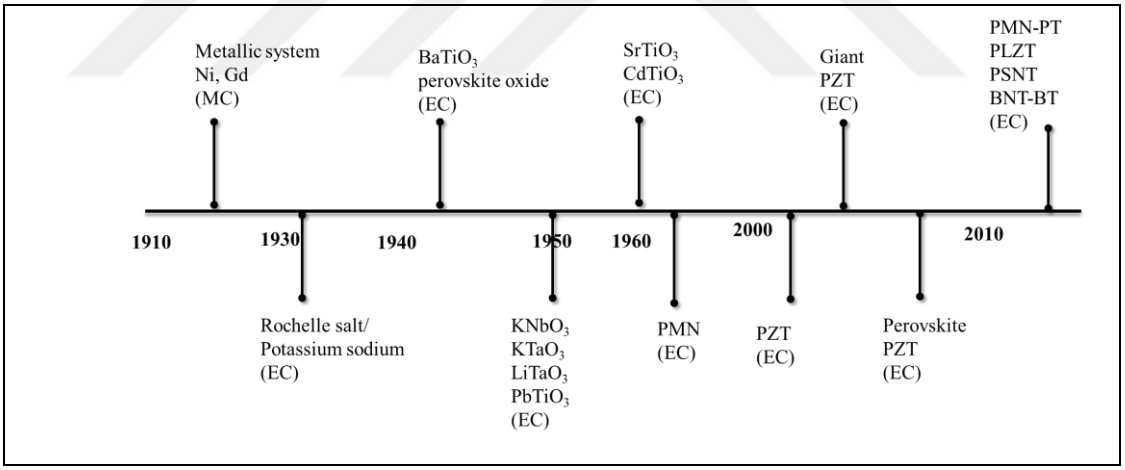

Figure 2.20: The chronological timeline of caloric materials due to use of caloric materials type.

In Figure 2.21, it can be seen cubic perovskite structure with their usage as solid state refrigerators system and other different technological applications.

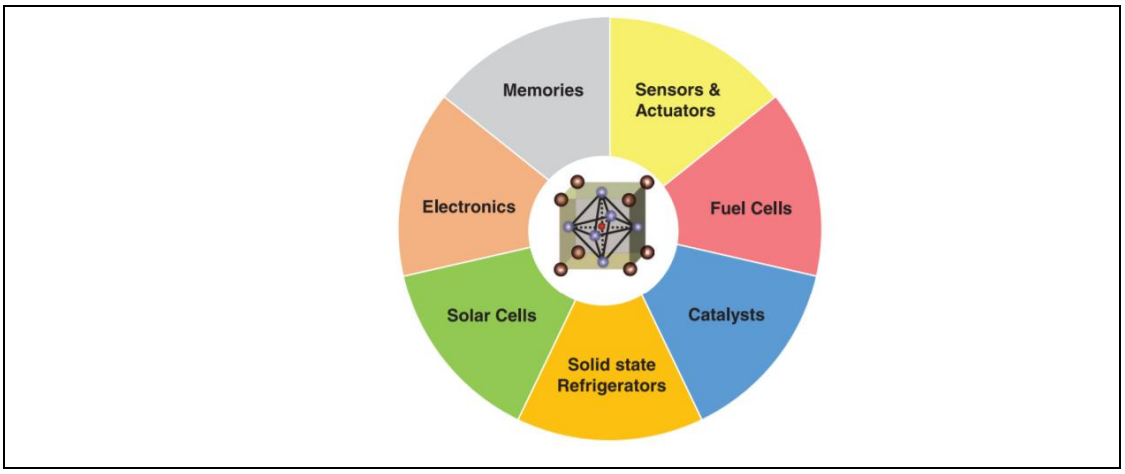

Figure 2.21: The illustration of cubic perovskite structure in the middle, with different technological application type.

Table 2.1:ECE measurements of some materials (a: indirect, b: direct measurement).

Material	**T[K]**	**IEI [kVcm^{-1}]**	**T[K]**	**IQI[Jkg^{-1}]**	**|S|[JK^{-1} kg^{-1}]**
PMN	343	90	2.6[b]	910	2.65
0.75PMN-0.25PT	383	25	1.15	360[a]	0.94
0.72PMN-0.28PT	404	9	0.53[b]	186	0.459
0.7PMN-0.3PT	433	90	2.8[a]	980	2.26
$SrTiO_3$	18	8	0.06[a]		
$BaTiO_3$	401	10	1.4[b]	1330	3.32
Thick films and multilayer					
$BaTiO_3$(1.4 µm)	353	176	1.8	890[a]	2.52[a]
$BaTiO_3$(3µm)	353	800	7.1[b]	3565[b]	10.1[a]
Thin films					
0.65PMN-0.35PT (240 µm)	413	747	31[b]	11500	28
0.67PMN-0.33PT (200 µm)	418	600	14.5[b]	5000	12

2.4.2. Thermodynamics of Electrocaloric Measurements

Maxwell Equation; Electrocaloric effect causes a squence of thermal response changes in material structure symbolized by X which is the applied electric field due to changes in the polarization denoted by Y. Derivation of the pyroelectric and electrocaloric coefficients comes from the thermodynamic analysis.

The Gibbs free energy density G of a dielectric is shown in Equation 2.9, Equation 2.10, Equation 2.11. expressed as a function of temperature T, entropy S, stress χ, strain x, electric field E, and dielectric polarization P. With the following equations changeable pairs (S, T) and (P, E) satisfy the standard Maxwell relation[16,17,19].

$$dG = -S\,dT - x_i X_i - P_i\,dE_i \tag{2.9}$$

$$S = \left(\frac{\partial G}{\partial T}\right)_{x,P} \quad , x_i = -\left(\frac{\partial G}{\partial x_i}\right)_{T,P}, \quad P_i = -\left(\frac{\partial G}{\partial E_i}\right)_{T,x} \tag{2.10}$$

$$\left(\frac{\partial S}{\partial E_i}\right)_{T,x} = \left(\frac{\partial P_i}{\partial T}\right)_{E,x} \tag{2.11}$$

Assuming a constant stress χ, the entropy changes while an adiabatic process is given by Equation 2.12 and Equation 2.13 and as follows:

$$dS = \left(\frac{\partial S}{\partial E}\right)_T dE + \left(\frac{\partial S}{\partial T}\right)_E T = 0 \tag{2.12}$$

$$\left(\frac{dT}{dE}\right)_s = \frac{T}{c_E}\left(\frac{\partial P}{\partial T}\right)_E = \frac{T}{c_E} PE \tag{2.13}$$

C_E is the heat capacity per unit volume and $p_E = (\partial P/\partial T)_E$ is the pyroelectric coefficient at constant electric field given by Equation 2.14:

$$C_E = T\left(\frac{\partial S}{\partial T}\right)_E \tag{2.14}$$

Using the equations given above, one can acquire the adiabatic temperature change by using Equation 2.14, where $\Delta T_{EC} \equiv T(E_2) - T(E_1) = T_2 - T_1$ by Equation 15:

$$\Delta T_{EC} = -\int_{E_1}^{E_2} \frac{T(E)}{C_E(T)}\left(\frac{\partial P}{\partial T}\right)_E dE \tag{2.15}$$

The isothermal entropy change ΔS_T given by $(\partial S/\partial T)_E$ at constant field E over T is provided by Equation 2.16:

$$\Delta S_T = \int_{E_1}^{E_2} \left(\frac{\partial P}{\partial T}\right)_E dE \tag{2.16}$$

In useful applications of equation ΔT_{EC}, known as an indirect method of ECE in which the usual input data consists of the empirical values for the dielectric polarization P(E, T) and the heat capacity $C_E(T)$. By assessing the integral numerically, values for the ECE temperature change ΔT_{EC} (E, T) are gained. In practice, the ECE estimation gained by the indirect method should possibly be tested by the direct methods based on the electrocaloric thermometry. Nevertheless, in some cases, the Maxwell approach might not give a confidential prediction for the ECE temperature change $\Delta T_{EC.}$ Accordingly, there is an alternative method based on the separation of the entropy into a lattice part which is regular, and the dipolar part which is obtained from the corresponding dipolar free energy [19,20].

Landau Phenomenological Approach; A typical system in ECE experiment measurement consist of two entropy components shown in Equation 2.17, in which adiabatic ECE process must be zero:

$$\Delta S\ (E, T) = \Delta S_{latt}(T) + \Delta S_{dip}(E, T) = 0 \tag{2.17}$$

where $\Delta S_{latt}(T)$ is showed entropy level of the weakly polarizable lattice and $\Delta S_{dip}(E, T)$ is the addition of the dipolar part. In ferroelectrics, antiferroelectrics, and dipolar glasses, the dipolar degrees of freedom are typically associated with individual molecular dipole moments or ionic displacements, whereas in relaxor ferroelectrics they can be represented as accumulates of polarized unit cells also known as polar nanoregions (PNRs). By presumption, $S_{latt}(T)$ does not depend on the field only when temperature changes from T_1 to T_2 it can be utilized as an integral over the lattice specific heat C_{latt} which represents the heat capacity of the lattice.

$$\Delta S_{\text{latt}} = \int_{T_2}^{T_1} \frac{C_{latt}(T)}{T}\, dT \approx C_{latt}(\mathrm{T_1}) \log\,(T_2/T_1) \tag{2.18}$$

The dipolar entropy $S_{dip}(E, T)$ can be calculated by considering the Landau free energy of the dipolar subsystem:

$$F = F_0 + \frac{1}{2} a\, P^2 + \frac{1}{4} b\, P^4 + \frac{1}{6} c\, P^6 + \frac{1}{8} d\, P^8 + \ldots - E\, P \tag{2.19}$$

Here, F_0 is the field-independent parameter shown in Equation 2.19. and P = P(E, T) is a scalar order parameter representing the dielectric polarization. The *a* is a temperature-dependent parameter and b, c, d, and so on are generally assumed to be temperature independent parameters. In ferroelectrics, b > 0 and b < 0 correspond to a second order and first-order phase transition, respectively. The dipolar entropy $S_{dip} = -(\partial F/ \partial T)$ is written as.

$$S_{dip} = S_0 + S_1(P) \tag{2.20}$$

Where $S_0 = -(\partial F_0/ \partial T)$ is the configurational entropy of the dipolar assest and S_1 (P) is in general gained from Equation 2.21.:

$$S_1(P) = -\frac{1}{2} a_1\, P^2 - \frac{1}{4} b_1\, P^4 - \frac{1}{6} c_1\, P^6 - \frac{1}{8} d_1\, P^8 + \ldots \tag{2.21}$$

The temperature of ECE is changed ($\Delta T_{EC} = T_2 - T_1$) according to the following relationship given Equation 2.22.:

$$\Delta T_{EC} \cong \frac{T}{2C_{latt}(T)}[a_1(T + \Delta T_{EC})P^2(E, T + \Delta T_{EC}) - a_1(T)P^2(0, T)] \quad (2.22)$$

$$aP + bP^3 + cP^5 + \ldots - E = 0 \quad (2.23)$$

These equations can be solved for P(E, T). Hence, P responds to stable minimizing of the free energy, therefore real equilibrium states of the system should be used in Equation 2.23. ΔT_{EC} [19].

ECE in Ferroelectrics; In ferroelectric system, undergoes second-order phase transition, set b>0 and $a(T) - a_1 (T - T_0)$ where a_1 of the order of the inverse Curie constant. Additionally, second-order phase transition equal the Curie temperature T_c. Other coefficients c, d, and so on are neglected because of second-order phase transition:

$$aP + bP^3 - E = 0 \quad (2.24)$$

For E = 0 and $T > T_c$ the solution is simple P = 0, and for $T < T_c$ one has $P = P_0$, where

$$P_0^2 = \frac{a_1}{b}(Tc - T) \quad (2.25)$$

When $E \neq 0$, the dielectric permittivity in zero bias field is given by

For $T < T_c$

$$\left.\frac{1}{\epsilon(E,T)} - \frac{\partial E}{\partial P}\right|_{E=0} = 2a_1(T_c - T) \quad (2.26)$$

For $T > T_c$

$$\left.\frac{1}{\epsilon(E,T)} - \frac{\partial E}{\partial P}\right|_{E=0} = a_1(T - T_c) \quad (2.27)$$

With Equation 2.25 and 2.26, the a_1 and b parameters can be specified from empirical data for spontaneous polarization and permittivity versus temperature, respectively. The dipolar entropy change obtains from Equation 2.21. and ultimate equations given Equation 2.28., Equations 2.29., Equation 2.30 [19]:

$$\Delta S_{dip} = -\frac{1}{2} a_1 [P^2(E_2, T) - [P^2(E_1, T)] \quad (2.28)$$

$$\Delta T_{EC} \cong \frac{a_1 T}{2C_{latt}} [P^2(E, T + \Delta T_{EC}) - P_0^2(T)] \quad (2.29)$$

$$C_{dip} = T\,[a_1 P(E, T)]^2 \chi(E, T) \quad (2.30)$$

2.4.3. Types of Electrocaloric Measurements

Electrocaloric effect can be measure by three methods which are called indirect, quasidirect, and direct methods. Generally, electrocaloric materials are measured to get the adiabatic temperature change (ΔT), isothermal heat (Q), the isothermal entropy change (ΔS) at specific temperature and change of one or more induced field. Commonly, indirect and quasidirect methods are more feasible than the direct method to measure electrocaloric effect due to the difficulties in measuring ΔT, ΔS, Q in the direct method.

Indirect Method; Maxwell and Clausius-Clapeyron relations of thermodynamic analysis are used to obtained ΔS values from empirical data results. X is replaced for the effects of temperature and field; Y is replaced on the local order parameter. With the data results from values of parameters Y measured at field ΔX at approximate temperature, ΔS can be nearly calculated [16,17,19].

Quasidirect Method; The temperature dependence of heat capacity c calculated and then using the c values for Maxwell and Clausius-Clapeyron relations ΔS and ΔT more exactly acquired via calculated heat capacity depend on temperature. Also, heat Q is measured with quasidirect method using special calorimeters, that allows the application of constant field X at changeable temperature T, via using the temperature and field dependence of the local order parameter [16,17,19].

Direct Method; Heat Q and ΔT are measured directly and independently. Differential scanning calorimetry (DSC) is useful to measure isothermal heat directly. This method permits the application of variable field X at various temperature T via contact or non-contact thermometry temperature changes measured directly. The heat leakage between samples and surrounding materials might cause incorrect results but the direct measurements of Q and T are always demanding. In the ultimate method, the direct measurement of pyroelectric currents under various applied electric field gives the pyroelectric coefficient and consequently the electrocaloric response of the material. Using the recent advanced technology, the scanning thermal microscopy and the infrared imaging techniques become more beneficial for the direct ECE measurement of the temperature distributions [16,17,19].

3. EXPERIMENTAL STUDY

3.1. Synthesis of PMN-PT Powders

To synthesize 0.72PMN-0.28PT ceramic powder composition, conventional solid-state reaction method was used. Solid-state reaction method contains two steps; the first step is named as columbite precursor method, and second step is named as mixing oxides as shown in Figure 3.1. Raw materials for 0.72PMN-0.28PT ceramic powder are magnesium carbonate hydroxide pentahydrate $(MgCO_3)_4$. Mg $(OH)_2.5H_2O$ (Sigma Aldrich, 98%) and niobium pentoxide (Nb_2O_5) (Alfa Aesar, 99.5%) for the first step to obtain magnesium niobate ($MgNb_2O_6$) to use in the second step. The second step starting powders which are lead carbonate $(PbCO_3)_2.Pb(OH)_2$ (Sigma Aldrich), titanium oxide (TiO_2) (Degussa, P25) were mixed with the pre-obtained magnesium niobate ($MgNb_2O_6$) due to stoichiometric ratios, as shown Equation 3.1 and Equation 3.2. All powders were mixed, and ball milled within ZrO_2 media in ethanol for 24 hours, then was dried at 70ºC on the hot plate. After that, the green powder of 0.72PMN-0.28PT was calcined at 850ºC for 4 hours with excess 2 wt% lead oxide (PbO)(ZAG).

Table 3.1: Raw materials for PMN-PT.

Chemical	**Aim of Use**	**Commercial Source**	**Purity (%)**	**CAS No:**
$(MgCO_3)Mg(OH)_2.5H_2O$	$MgNb_2O_6$ Synthesis	Alfa Aesar	99	56378-72-4
Nb_2O_5		Alfa Aesar	99.5	1313-96-8
$(PbCO_3)_2.Pb(OH)_2$	PMN-PT Powder Synthesis	Sigma Aldrich	99	1319-46-6
TiO_2		Degussa, P25	99.9	13463-677
PbO		ZAG	99.9	1317-36-8
PbO		Alfa Aesar	99.9	1317-36-8
MnO_2		Alfa Aesar	99.9	-
Polyvinyl Butrial (PVB)	Binder	Sigma Aldrich	-	63148-65-2
Polethylene Glycol (PEG)			-	25322-68-3
Benzyl Butyl Phtalate (BBP)		Fluka Sigma Aldrich	-	85-68-7

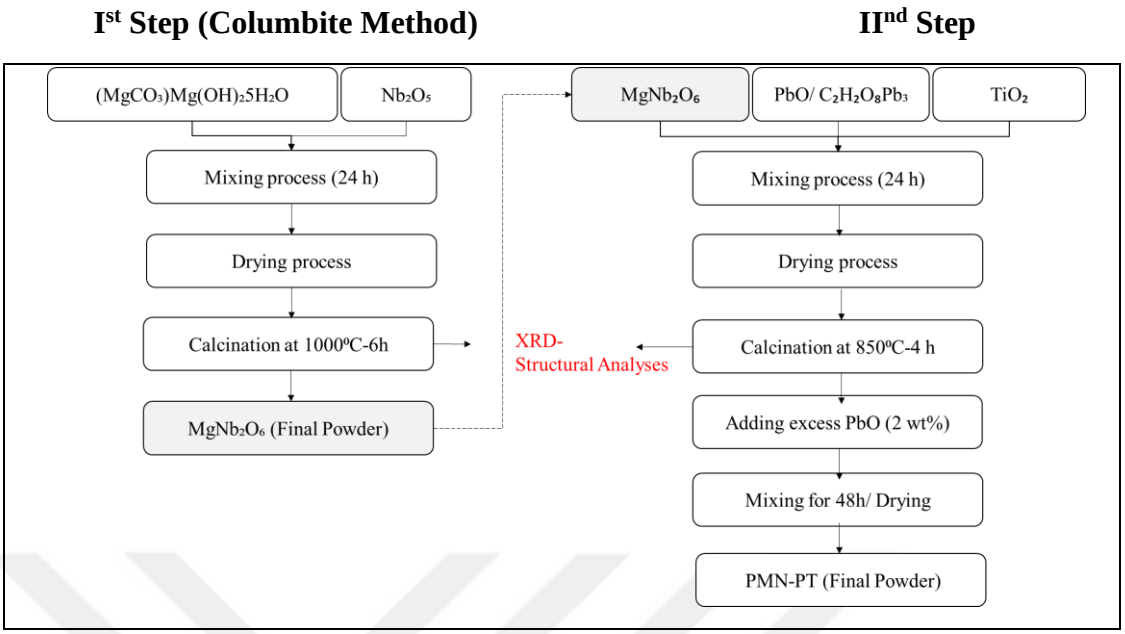

Figure 3.1: The flow chart of the fabrication of $MgNb_2O_6$ and PMN-PT powders by Columbite and solid-state calcination methods.

$$\text{I}^{st}\text{ Step:}\quad (MgCO_3)(MgOH)_2.5H_2O + Nb_2O_5 \rightarrow MgNb_2O_6 \qquad (3.1)$$

$$\text{II}^{nd}\text{ Step:}\quad 0{,}24\,(MgNb_2O_6) + 1/3\,[(PbCO_3)_2\,Pb\,(OH)_2] + 0{,}28\,(TiO_2) \rightarrow \qquad (3.2)$$

$$0{,}72\,[Pb\,(Mg_{1/3}Nb_{2/3})\,O_3] - 0{,}28\,(PbTiO_3) + 2/3(CO_2) + 1/3(H_2O)$$

$$0.72PMN \quad - \quad 0.28PT$$

3.2. Preparation of the Dry Pressed Samples

Bulk ceramics samples were fabricated using powder 0.78PMN-0.28PT composition with by uniaxial press at 150 MPa for 3 minutes. Then, for sintering process was done in the alumina crucible. Additionally, 2 wt% PbO was added as a pellet to compensate for lead volatilization. After all, another alumina crucible was used to cover upside down onto all samples and alumina powder was encompassed to create an insulated environment during the sintering process. Finally, organic binder content was removed from the green ceramic samples by heat treatment at 600ºC for 1 hour with a heating rate of 2ºC/min, followed by sintering at 1150°C for 4 hours with a heating rate of 5°C/min. The final thicknesses of the ceramics were adjusted as 500 μm and 1000 μm.

3.3. Processing of the Tape-Cast Samples

Ceramic samples were fabricated using the tape-casting method. The tapes were prepared layer by layer. The slurry for tape- casting was prepared with synthesized 0.72PMN-0.28PT powder. These powders were mixed with an organic binder (~7 wt%), ethanol (34 wt%), and ethyl methyl ketone (66 wt%) as a solvent. To prepare slurry with the templates $BaTiO_3$ or $SrTiO_3$ were added with (ratio 5% mole, 1% mole) to the PMN-PT slurry and to provide homogeneity, the slurry was mixed with a magnetic stirrer on the hot plate. When the slurry has become demanding viscosity, the tape-casting process was done. Then, the tapes were cast on a clean glass substrate using by Doctor blade with a casting speed of 10 cm/s. After two hours of drying of casting materials, the green tapes were removed from the glass substrate. The tapes were punched and then laminated at 80ºC under uniaxial pressure at 150 MPa for three minutes. Then, the binder burn-out heat process was applied to the green samples at 600ºC for one hour with a heating rate of 1ºC/min. Then samples were sintered at 1150ºC or 1200ºC for various times 4 hours, 8 hours atmospheric conditions. The ultimate thicknesses of the ceramics were adjusted as 500 μm and 1000 μm. Therefore, these stacked dense tapes can be called as thick films. The silver electrode has applied to both surfaces of ceramic samples, then ceramic thick films were heated up to 600ºC

for 30 min. The flow chart of the fabrication process of the samples are shown in Figure 3.2.

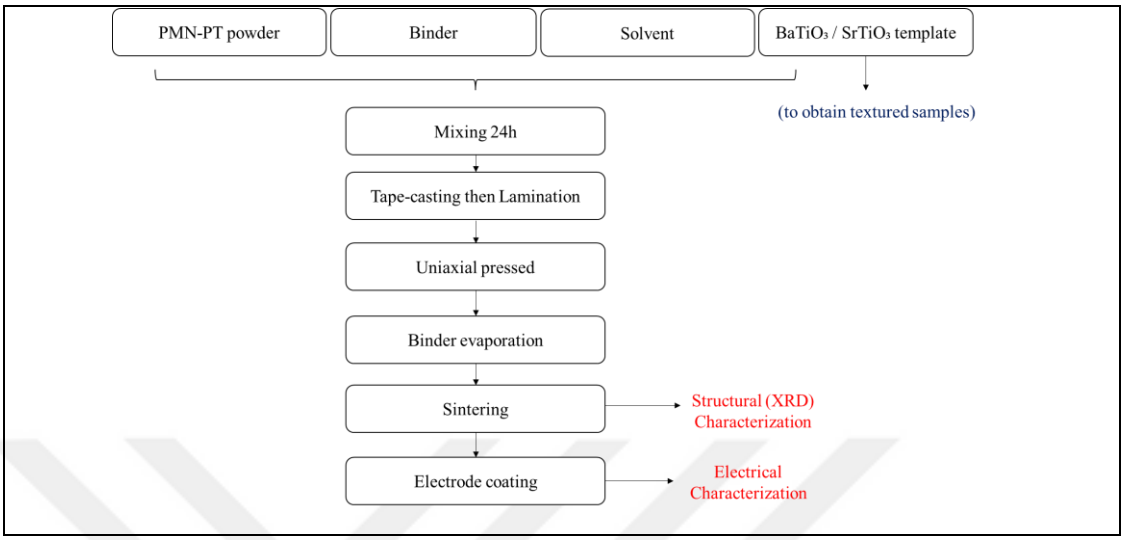

Figure 3.2: The flow chart for production of PMN-PTceramic samples.

All processes picture including of slurry and tape-casting were also given Figure 3.3.

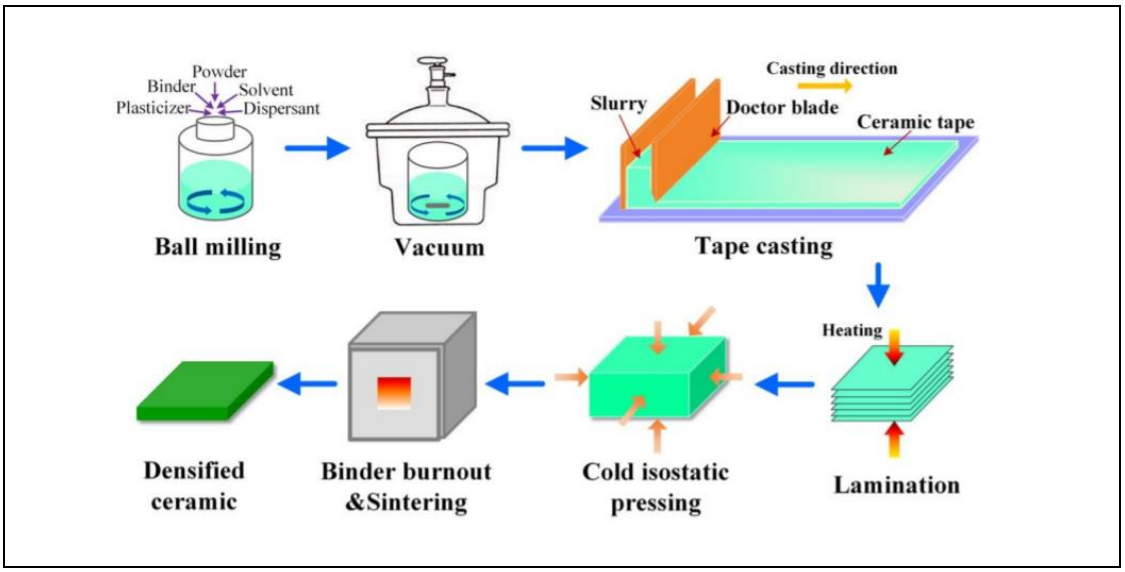

Figure 3.3: Schematic representation of sample preparation process.

3.4. Preparation of $BaTiO_3$ and $SrTiO_3$ Templates

This part of the study was cited from Ph.D. study of Ayşe Berksoy-Yavuz. Both molten salt synthesis (MSS) and topochemical microcrystal conversion (TMC) method combinations were used to synthesize the $BaTiO_3$ (BT) and $SrTiO_3$ (ST) template particles [21, 22, 29]. To obtain plate-like $BaTiO_3$ template particles, two steps synthesis in molten salt synthesis (MSS) and topochemical micro crystal conversation (TMC) have been used. Bi_2O_3 provide was used to produce platy $Bi_4Ti_3O_{12}$ (BIT) template particles (Alfa Aesar, 99% CAS:1317-80-2) It was weighed according to the stoichiometric reaction in the below**.** and the powders were homogeneously mixed in mortar. NaCl (Merck, 99% CAS: 7647-14-5) and KCl (1:1) were added as salt to this mixture after homogeneously mixing with ethanol (Merck). The slurry was dried in a magnetic stirrer at 80°C in a closed crucible environment. Heat treatment was done at 1100°C for 1 hour. The powder was washed eight times with hot de-ionized water to remove KCl and NaCl salts.

$$2Bi_2O_3 + 3TiO_2 \longrightarrow Bi_4Ti_3O_{12} \qquad (3.3)$$

In the second step, similar process has been followed to obtain $BaBi_4Ti_4O_{15}$(BBiT) particles. BiT template particles were prepared from $BaCO_3$ and TiO_2 without having any second phase, and then BBiT template particles were produced successfully.

3.5. Characterization

The microstructure and phase analysis of the powder and ceramics were examined by XRD (Bruker D8 Advanced, Germany) by using CuKα radiation in the range of $2\theta = 20^{o}-60^{o}$ with step size of 0.02^{o}. The crystallographic orientation level of textured samples along $<001>_{pc}$ were calculated by Lotgering Factor (*f)* [23,24] by using Equation 3.4, Equation 3.5, and Equation 3.6. A scanning electron microscope (SEM) (Philips XL30 SFEG, Eindhoven, Netherlands) was used to determine the surface and cross-section microstructures of the samples. The samples were prepared for SEM investigation after the grinding and polishing process, then thermal etching

was done at 980ºC for 30 min. To observe the grain boundaries of samples and to avoid lead-loss at high temperatures, the etching temperature was determined as ∼170ºC below the sintering temperature.

The polarization – electric field (P-E) hysteresis loops of samples were taken with a period of 2000 ms using a Precision LC ferroelectric tester (Radiant Technologies, Inc., USA) at room temperature. These measurements were also done from 90ºC to 25ºC during cooling for 10 min. waiting duration where was applied for each measurement step, as shown in Figure 3.4. The dielectric permittivity (ε_r) versus loss tangent (tanδ) measurement depending on temperature was done using by LCR meter (Hioki 3520, Japan) at room temperature (RT) at 1-100 kHz. The measurement range was from room temperature up to 250°C by the heating ratio of 2°C/min. Heat treatment furnace and LCR meter are shown in Figure 3.5.

Lotgering factor;
$$f_{L(00l)} = \frac{P_{(00l)} - P_0}{1 - P_0} \tag{3.4}$$

Textured orientation of ceramic;
$$P_{(00l)} = \frac{\sum l_{(00l)}}{\sum l_{(hkl)}} \tag{3.5}$$

Random orientation of polycrystalline;
$$P_0 = \frac{\sum l_{0(00l)}}{\sum l_{0(hkl)}} \tag{3.6}$$

Figure 3.4: Precision LC ferroelectric tester device.

Figure 3.5: LCR meter device.

4. RESULTS and DISCUSSION

In this chapter, the parameters such as different fabrication methods, different sintering durations at various temperatures, and effect of the addition of BT and ST templates on the structural and electrical properties of PMN-PT ceramics were investigated with various characterization methods. Results were discussed in detail.

4.1. Structural Analyses

In this section, structural analyses of the PMN-PT powder and ceramic samples after the calcination and sintering processes were given and discussed.

4.1.1. Phase and Microstructural Analyses of PMN-PT Powder

The 0.72PMN-0.28PT powders were calcinated at 850ºC for 4 hours due to in previous research [22,30] and DTA analysis of green powder. The columbite method was used to obtain magnesium niobate ($MgNb_2O_6$) powder. XRD analysis of $MgNb_2O_6$ was shown in Figure 4.1. The XRD pattern of 0.72PMN-0.28PT powder was given in Figure 4.2. A pure perovskite structure has been obtained without any secondary phase such as pyrochlore shown in Figure 4.2. The particle size distribution of the powder was measured by particle size analyzer and the result was shown as inset figure in Figure 4.2. SEM micrograph analyses of the 0.72PMN-0.28PT powder was also given as inset figure in Figure 4.2. Narrow and submicron particle size distribution was obtained, and mean particle size was found to be as 0.17 μm.

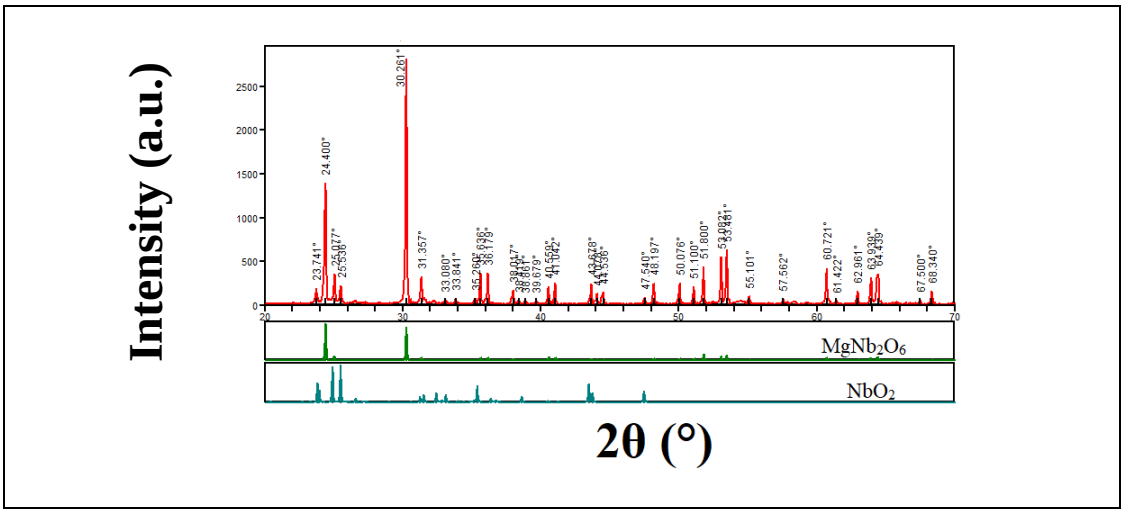

Figure 4.1: XRD pattern of $MgNb_2O_6$ powder.

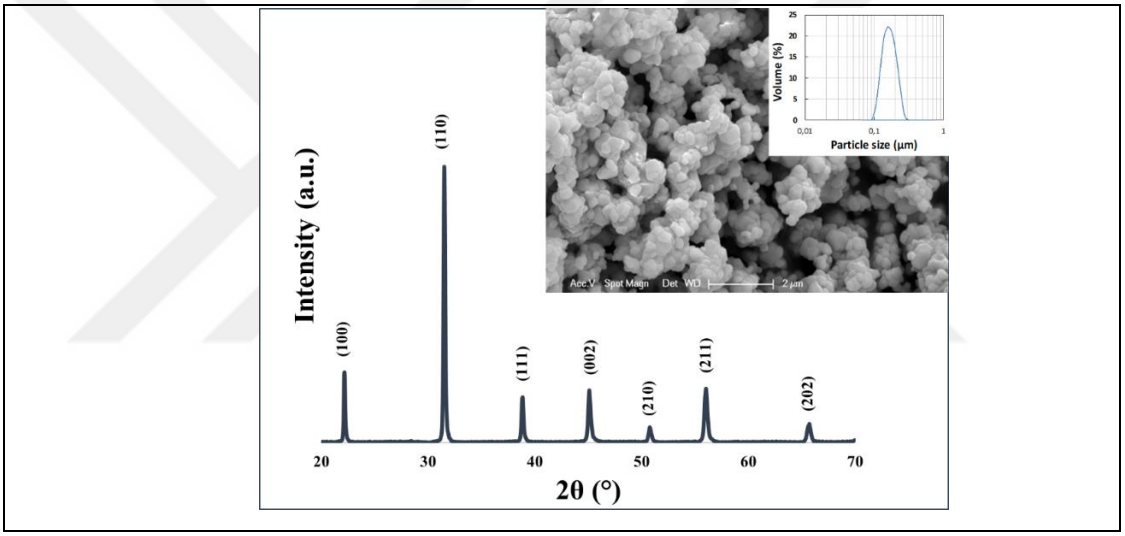

Figure 4.2: XRD pattern, SEM micrograph, and particle size distribution graph of 0.72PMN-0.28PT powder after the calcination.

4.1.2. Structural Analyses of the Templates

In this section, X-ray diffraction patterns and SEM micrographs (as inset figure) of the templates were given in Figure 4.3. and Figure 4.4. $BaTiO_3$ template particles have crystallized with tetragonal symmetry in the pure perovskite structure and rectangular morphologies as seen in Figure 4.3. Nevertheless, $SrTiO_3$ template particles have a perovskite structure, these template particles have different morphology comparing to BT templates as shown in Figure 4.4.

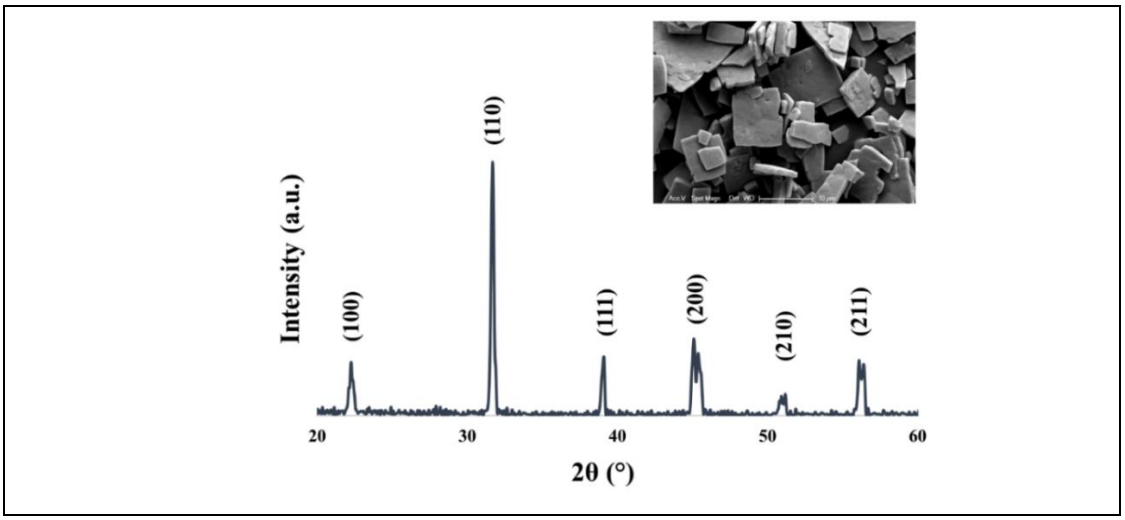

Figure 4.3: XRD pattern and SEM migrograph (inset figure) of $BaTiO_3$ templates.

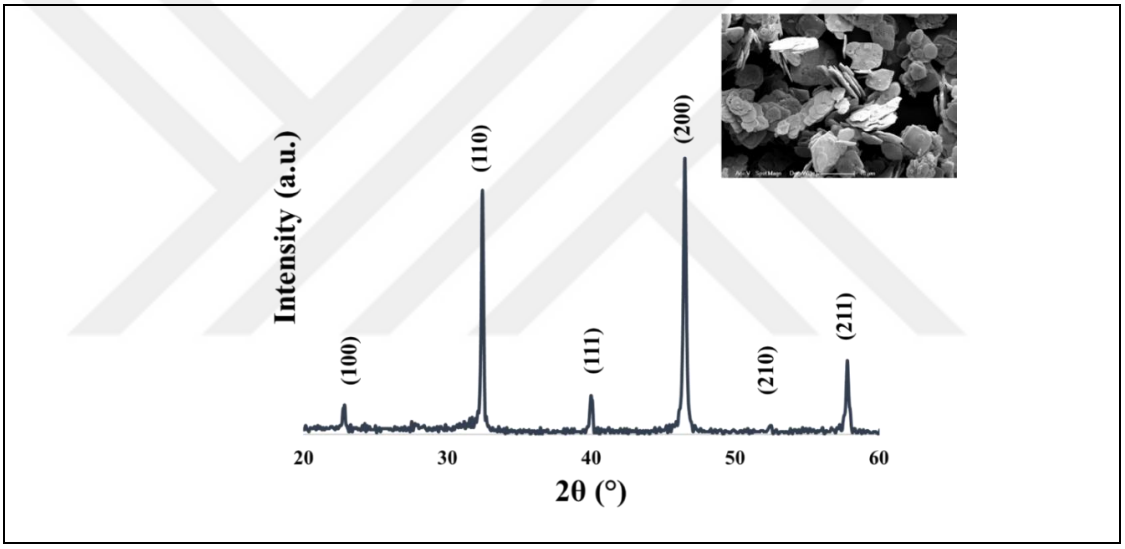

Figure 4.4: XRD pattern and SEM micrograph (inset figure) of $SrTiO_3$ templates.

4.1.3. Structural Analyses of 0.72PMN-0.28PT Ceramics

In the literature, to obtain textured samples with 0.72PMN-0.28PT composition, usage of two different templates were reported. Generally, $BaTiO_3$ and $SrTiO_3$[23,24] template particles were widely used because of their similar lattice with matrix.

The XRD patterns of random and textured ceramics are shown in Figure 4.5. All samples crystallized in the pure perovskite phase without any secondary phases. It is observed from Figure 4.5 that the random ceramic has the peak with highest intensity for $(110)_{pc}$, as expected from the perovskite structure. The intensities of the $(110)_{pc}$ and other (hkl) peaks of textured ceramics decreased with the development of texture. The intensities of (100) and (200) peak increased sharply with texturing. The Lotgering factor, *f*, of the textured ceramics to addition with 5% mole BT was calculated as 80% and 20% for 5% mole BT as seen in Figure 4.5.

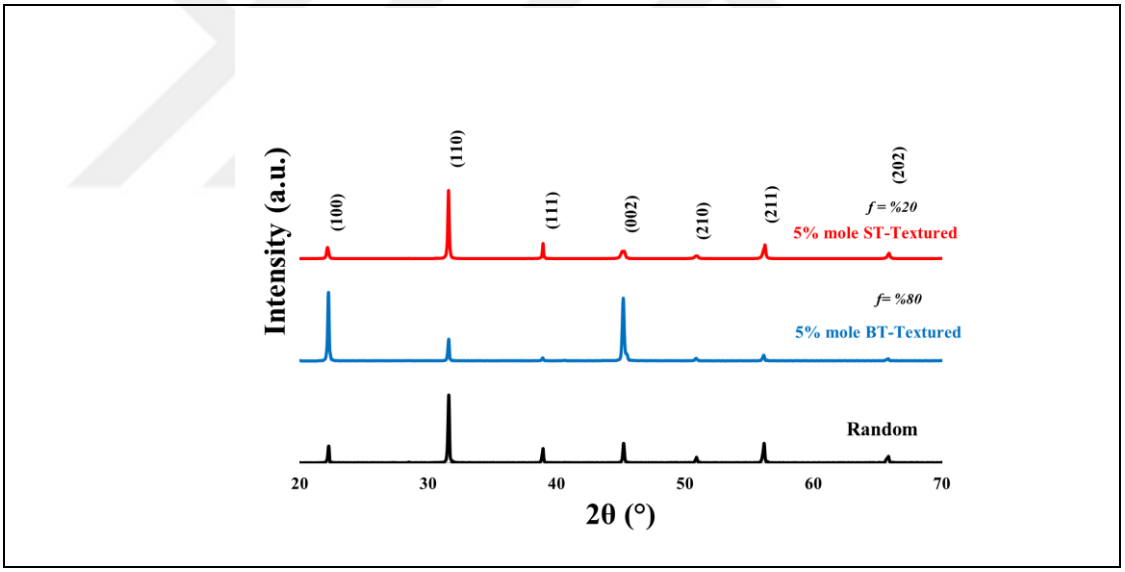

Figure 4.5: Comparison of XRD patterns of random and textured PMN-PT ceramics with 5% mole BT template addition.

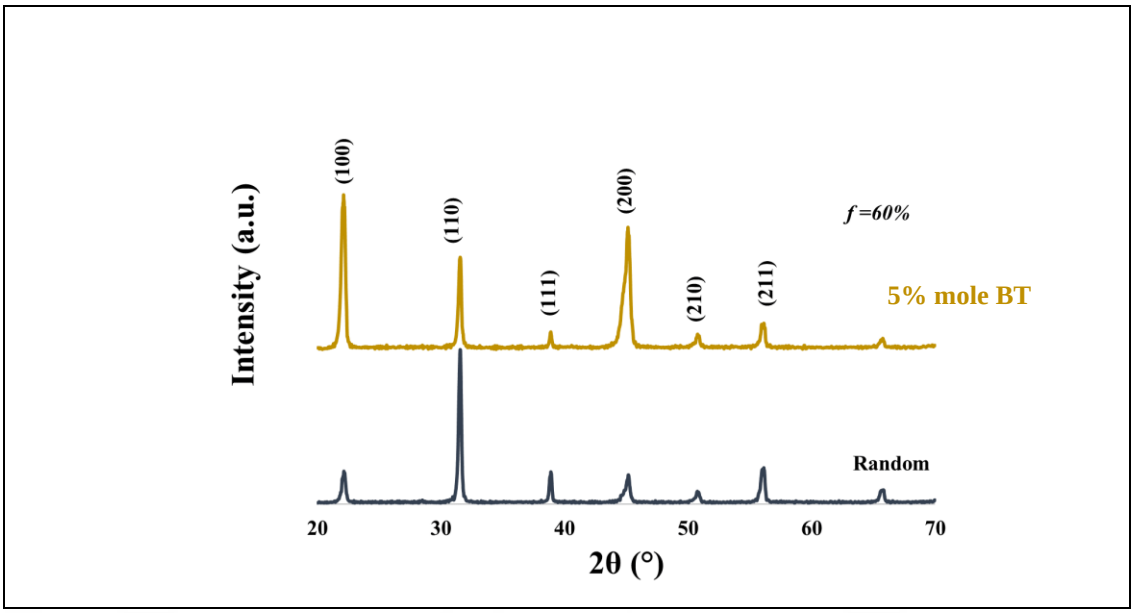

Figure 4.6: Comparison of XRD patterns of random and textured PMN-PT ceramics sintered at 1200ºC for 4h with 5% mole BT template addition.

Ceramics with for 5% mole BT addition and sinter at 1200ºC for 4 hours and 8 hours, lotgering factor, *f*, was found as 60%, 80%, respectively as shown in Figure 4.6, and Figure 4.7. The highest lotgering factor, *f*, 96% was measured for 1% mole BT addition and comparison of XRD patterns of random textured samples was shown in Figure 4.8.

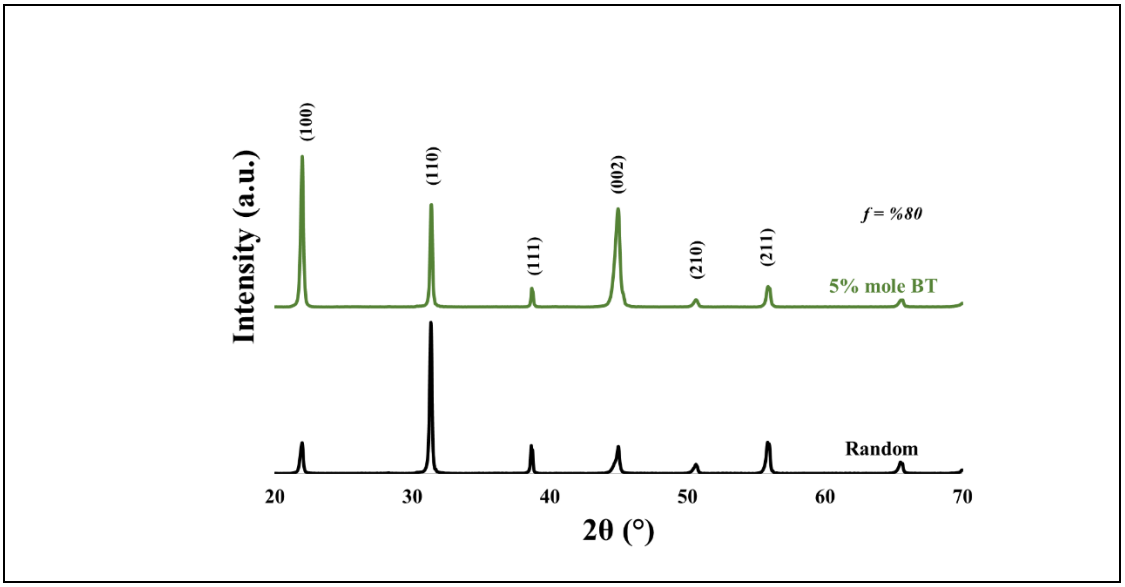

Figure 4.7: Comparison of XRD patterns of random and textured PMN-PT ceramics sintered at 1200ºC for 8h with 5% mole BT template addition.

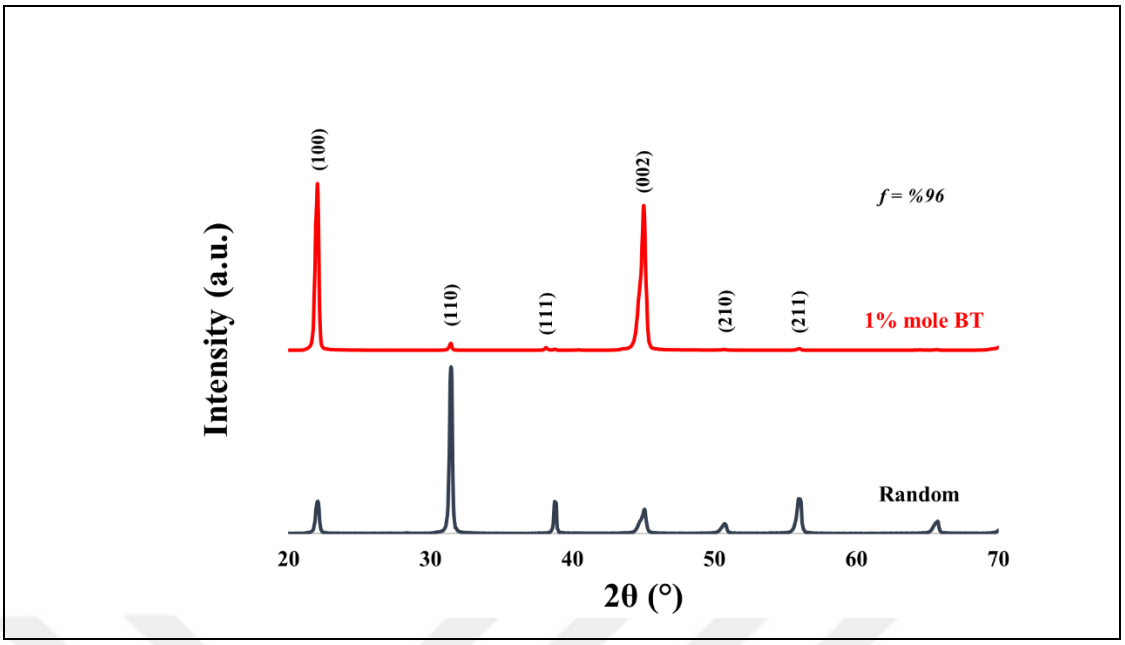

Figure 4.8: Comparison of XRD patterns of random and textured PMN-PT ceramics sintered at 1150ºC for 4h with 1% mole BT template addition.

PMN-PT ceramics were also prepared by dry-pressing method as undoped and Mn-doped .1% and 0.5% Mn was used as dopant ratios. XRD patterns of these samples were given in Figure 4.9.

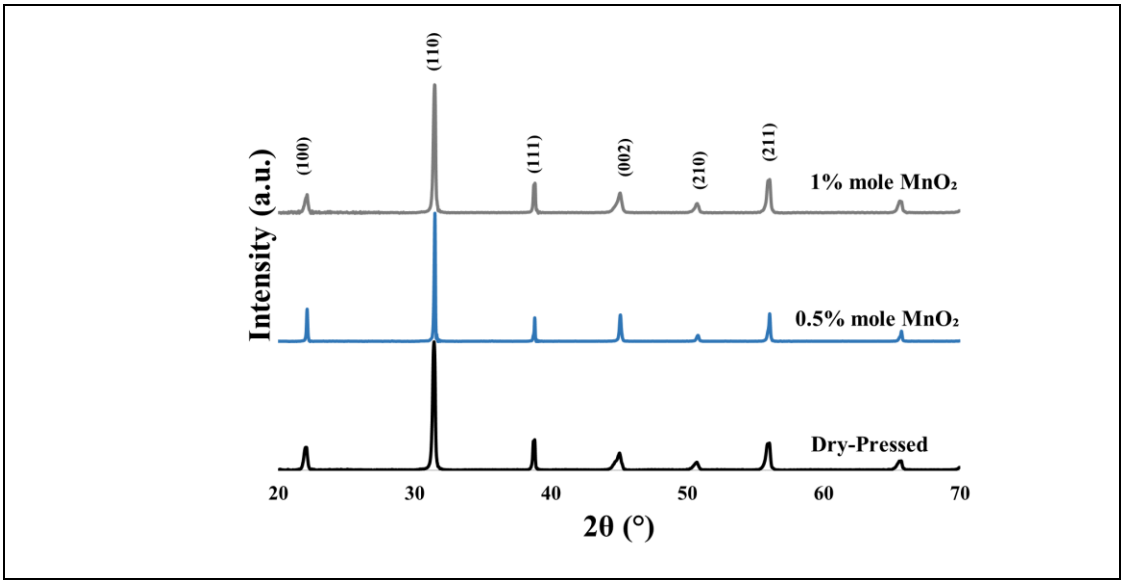

Figure 4.9: Comparison of XRD patterns of undoped, and doped PMN-PT ceramic with 0.5% mole Mn and 1% mole Mn addition of PMN-PT.

4.2. Microstructural Analyses of the PMN-PT Thick Films

SEM analyses were carried out to characterize the microstructure of the thick films. Samples were prepared by tape-casting process.

4.2.1. SEM Analyses of Tape-Cast Ceramics

BT and ST templates were used in this thesis study. Samples were textured in <001> direction using 5% mole BT, 1% mole BT, and 5% mole ST templates by tape-casting and TGG methods. SEM micrographs of the thermally etched surface and cross-sectional parts of PMN-PT samples were given in Figure 4.10. Both surface and cross-sectional views of microstructures exhibited a dense structure. Grain boundaries are also clearly visible in Figure 4.10 and templates were identified by arrows on the micrographs as given in Figure 4.11 and Figure 4.14. Uniform microstructures with sub-micron grains were observed for all ceramic samples. The BT template addition was changed the grain size and shape of TGG was observed for PMN-PT ceramics. Grain boundaries were also clearly visible for textured samples with BT template addition and identified by arrows on the micrographs as seen in Figure 4.11, Figure 4.12, Figure 4.13, and Figure 4.14 and these samples surface SEM micrographs shown in Figure 4.17, Figure 4.18, Figure 4.19, and Figure 4.20. The templates were very clearly seen for textured and were found to be well aligned in the PMN-PT matrix as seen in Figure 4.11-Figure 4.21. But ST templates were not observed in the structure of the PMN-PT sample, as shown in Figure 4.15. and Figure 4.21.

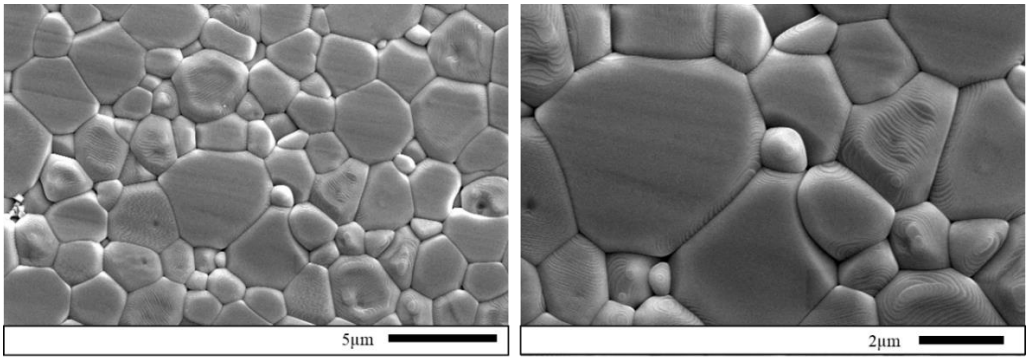

Figure 4.10: SEM micrographs of cross section of random PMN-PT ceramic sample with different magnifications.

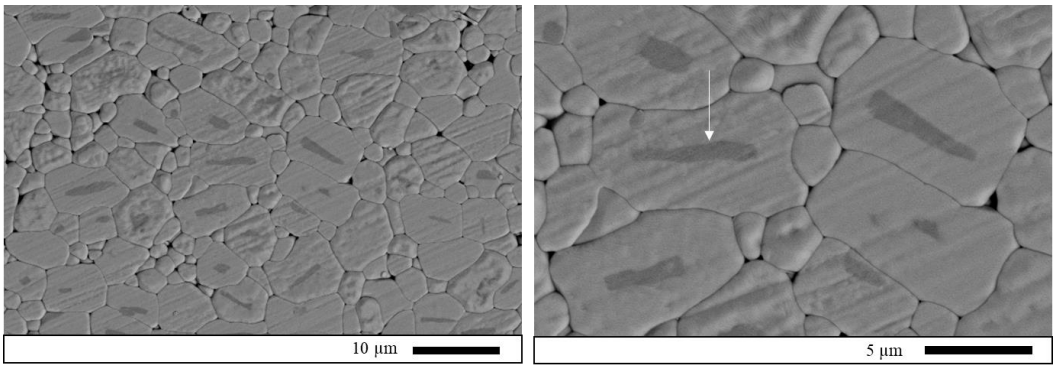

Figure 4.11: SEM micrographs of cross section of textured PMN-PT ceramic with 5% mole BT and sintered at 1150ºC for 4h.

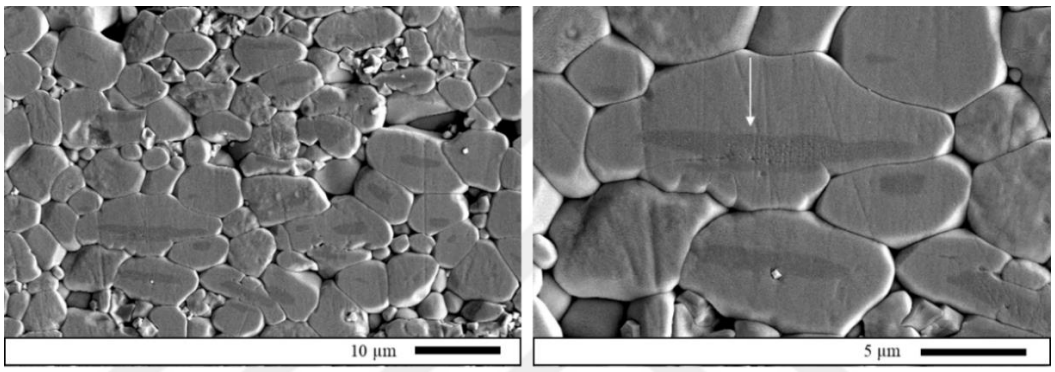

Figure 4.12: SEM micrographs of cross section of textured PMN-PT ceramic with 5% mole BT and sintered at 1200ºC for 4h.

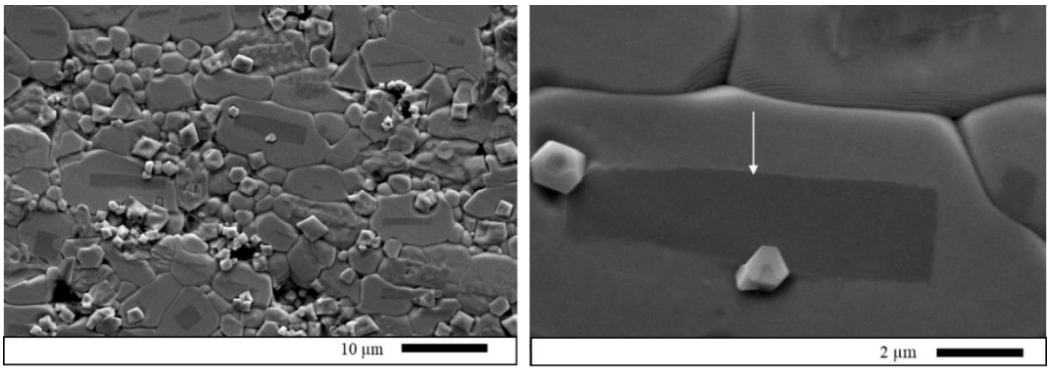

Figure 4.13: SEM micrographs of cross section of textured PMN-PT ceramic with 5% mole BT and sintered at 1200ºC for 8h.

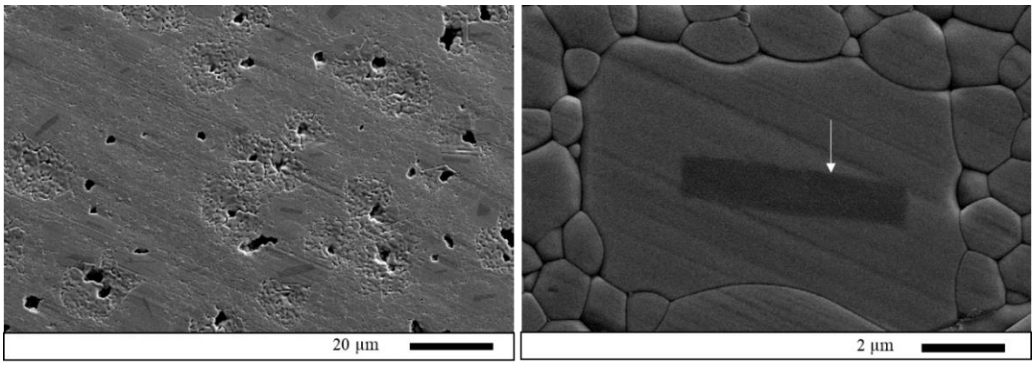

Figure 4.14: SEM micrographs of cross section of textured PMN-PT ceramic with 1% mole BT.

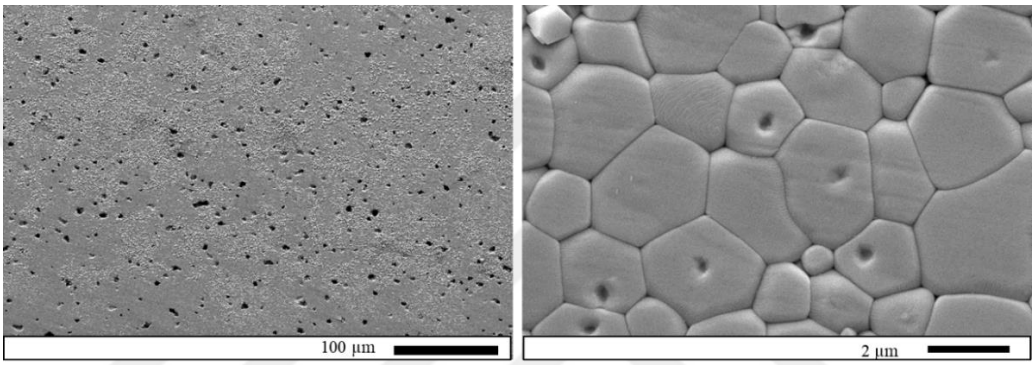

Figure 4.15: SEM micrographs of cross section of textured PMN-PT ceramic with 5% mole ST.

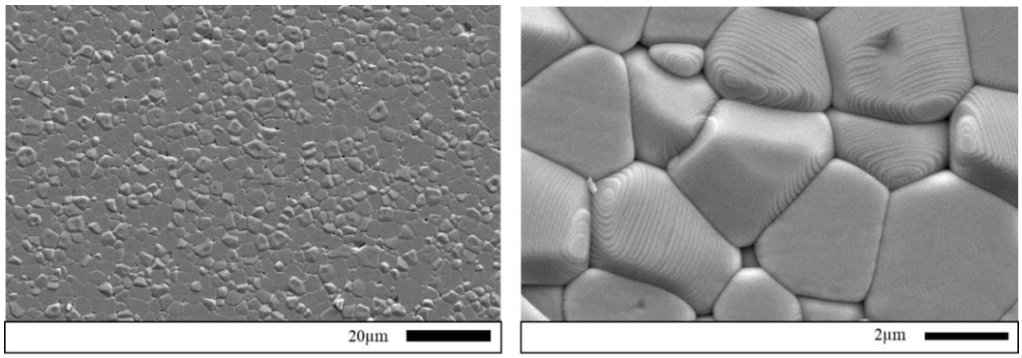

Figure 4.16: SEM micrographs of surface of random PMN-PT ceramic.

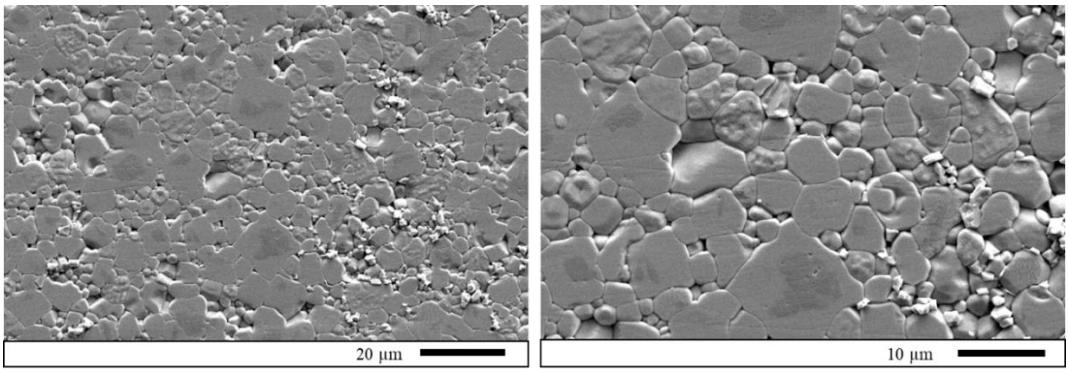

Figure 4.17: SEM micrographs of surface of textured PMN-PT ceramic with 5% mole BT and sintered at 1150ºC for 4h.

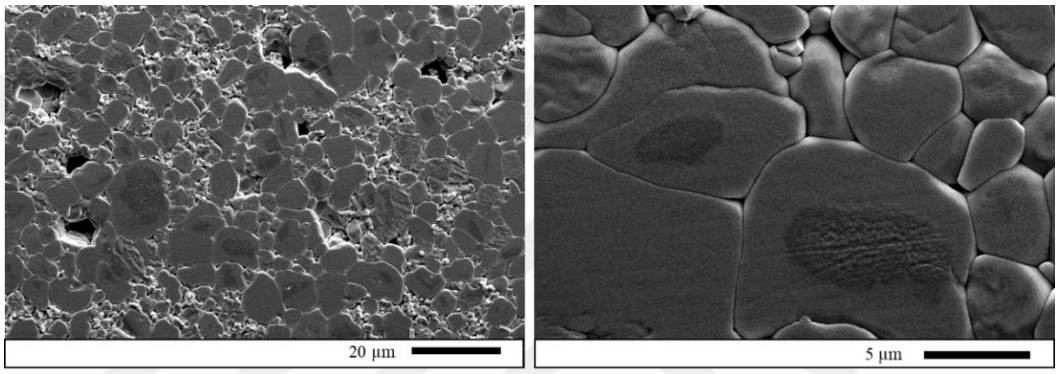

Figure 4.18: SEM micrographs of surface of textured PMN-PT ceramic with 5% mole BT and sintered at 1200ºC for 4h.

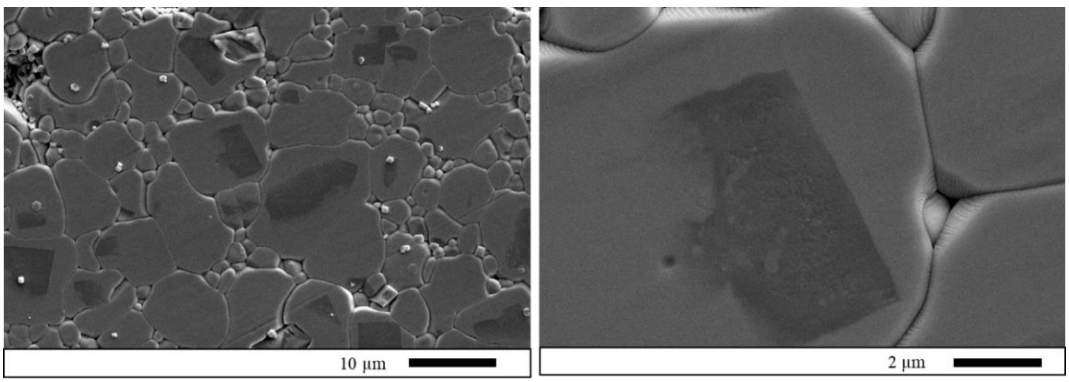

Figure 4.19: SEM micrographs of surface of textured PMN-PT ceramic with 5% mole BT sintered at 1200ºC for 8h.

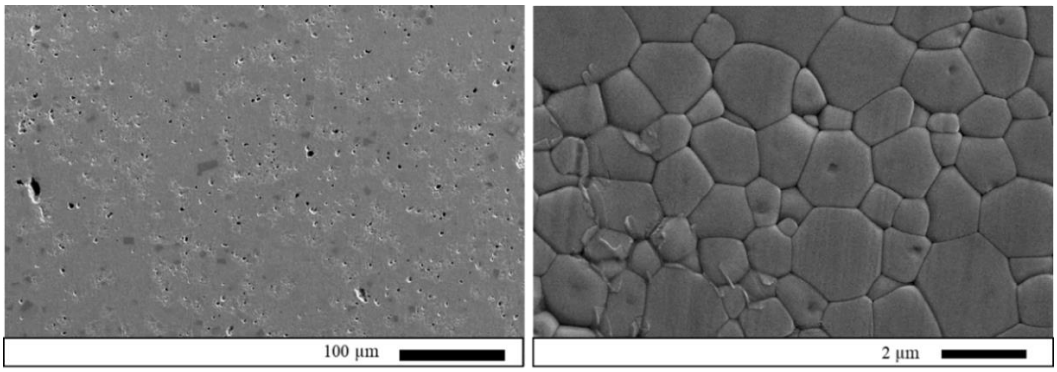

Figure 4.20: SEM micrographs of surface of textured PMN-PT ceramic with 1% mole BT.

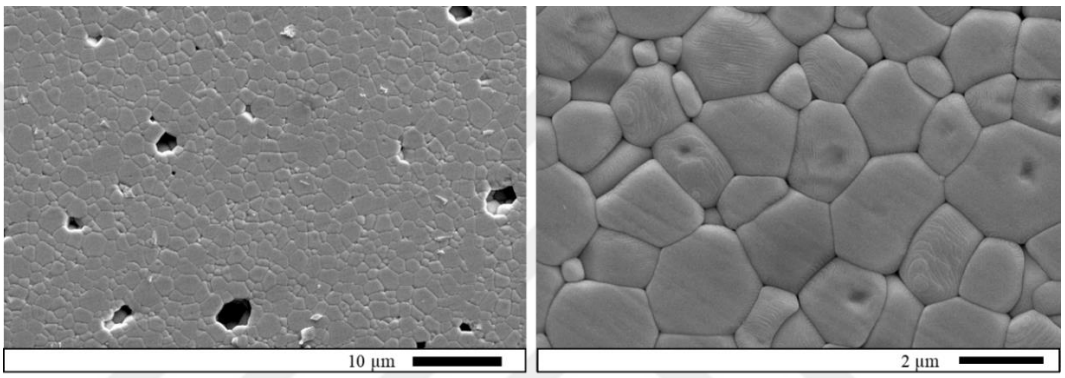

Figure 4.21: SEM micrographs of surface of textured PMN-PT ceramic with 5% mole ST.

As a summary, different sintering conditions and durations were provided TGG successfully. Well aligned textured grains were observed as seen surface and cross-sectional view (Figure 4.11— Figure 4.20) SEM micrographs of the PMN-PT samples.

4.2.2. SEM Analyses of Dry-Pressed Ceramics

MnO_2 was also used as dopant materials this thesis study. MnO_2 was added as 0.5% mole and 1% mole rations and then dry pressing were used, as shown in (Figure 4.22 and Figure 4.23). Both surface and cross-sectional views of microstructures exhibited a dense structure, in Figure 4.22 and 4.23. As seen in these figures, Grain boundaries were also clearly visible on the micrographs. For all SEM micrographs (Figure 4.22. and Figure 4.23), it was observed that, uniform microstructures with sub-micron grains were observed for the all-ceramic samples. Addition of the Mn was changed the grain size and shape of the PMN-PT ceramics. The grain growth and

bimodal grain size distributional were obtained by Mn addition, as seen Figure 4.22. and Figure 4.23.

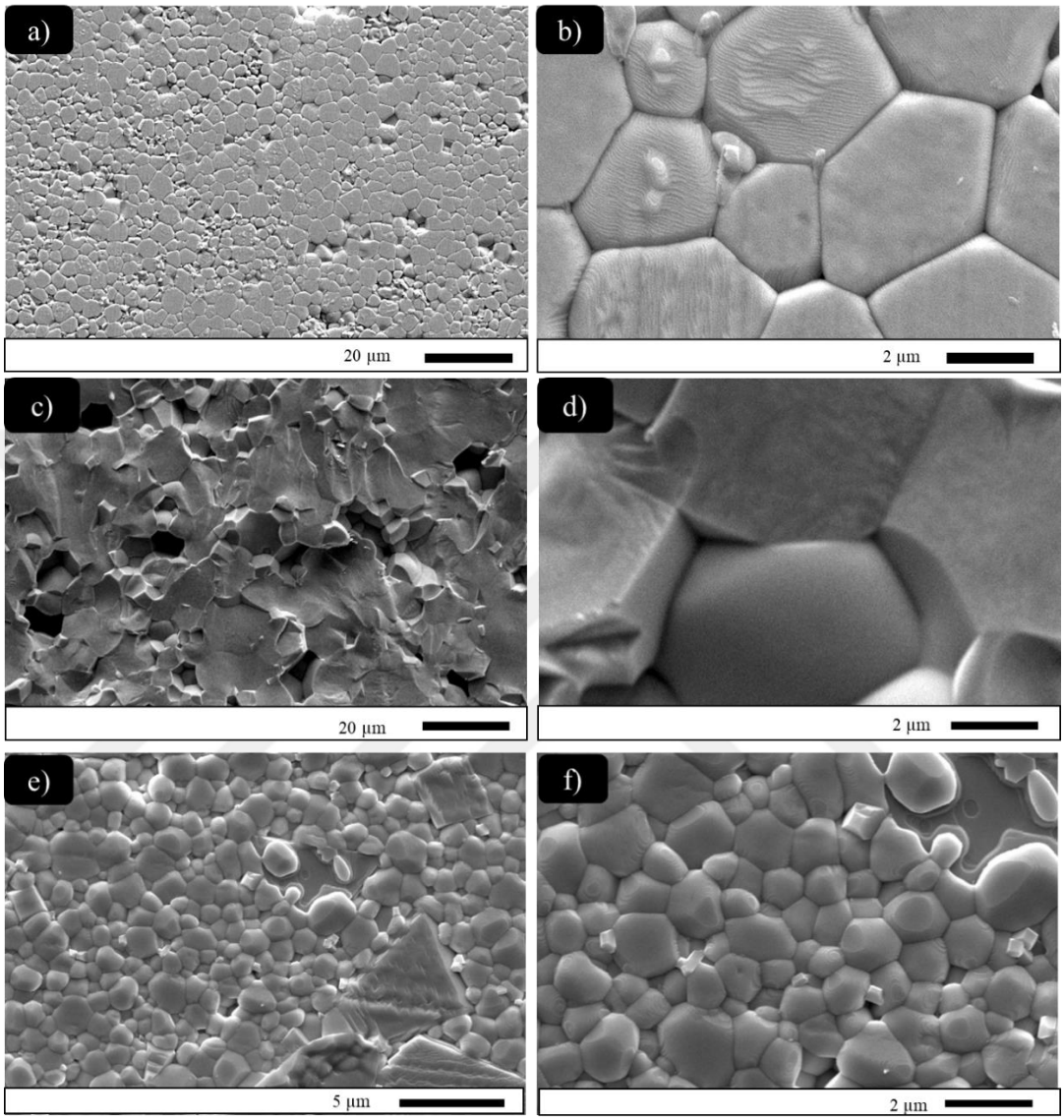

Figure 4.22: Comparison of SEM cross section analyses of PMN-PT samples: a-b) Undoped c-d) 0.5% mole Mn e-f) 1% mole Mn doped dry-pressed.

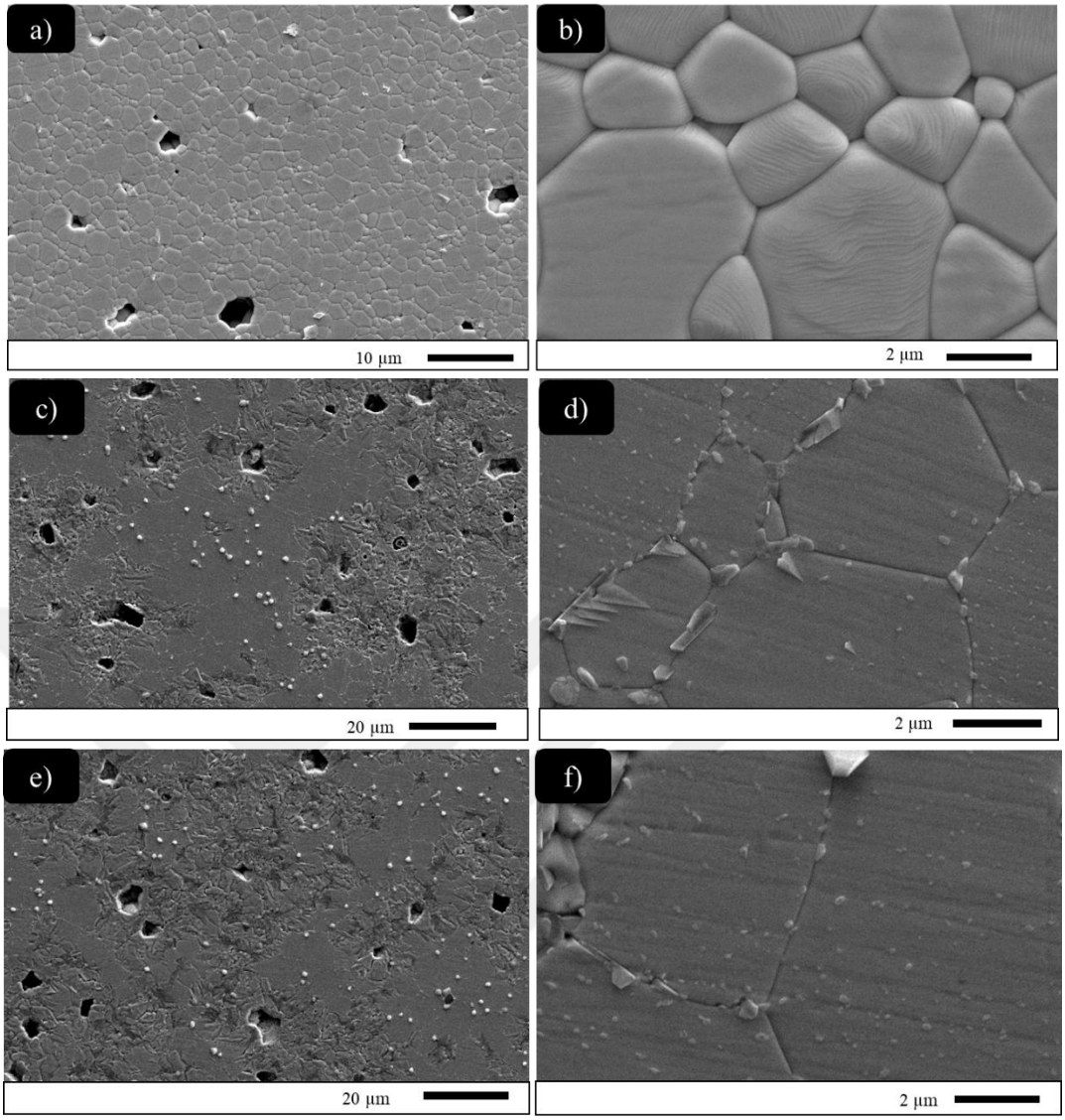

Figure 4.23: Comparison of SEM surface images of PMN-PT samples: a-b) Undoped c-d) 0.5% mole Mn e-f) 1% mole Mn doped dry-pressed.

4.3. Electrical Measurement Results

In this section, the change of dielectric constant (ε_r) and loss tangent (δ) depending on temperature, strain, polarization versus electric field hysteresis loops, electrocaloric measurements and analyses with the applied electric field as a function of temperature will be given.

4.3.1. Dielectric Measurement Results

The temperature dependence of the dielectric constant and loss tangent was exhibited a typical behavior as relaxor ferroelectrics, as shown in Figure 4.24 and Figure 4.25 below. The Curie Temperature (T_c) increases with increasing frequency, while the magnitude of the peak decreases. There is a strong dielectric dispersion depending on frequency below T_c. The temperature dependence results of the dielectric constant (ε_r) and loss tangent ($\tan\delta$) of tape-cast samples (Random, 5% mole BT, 1% mole BT, and 5% mole ST added) sintered at different parameters, and with different BT and ST template contents was shown in Table 4.1, respectively. The values of Curie temperature of random and textured tape-cast samples (5% mole BT, 1% mole BT, and 5% mole ST added) were 132ºC, 128ºC, 128ºC, 148ºC, and 68ºC, respectively. The values of dielectric constant (ε_r) and loss tangent ($\tan\delta$) at Curie temperature were measured as 27972, 21596, 22352, 16463, 12333 and 0.15, 0.019, 0.030, 0.026, 0.021. Depending on the barium titanate template addition, T_c of the samples were measured and calculated in the range of 125ºC-150ºC ST template addition was decreased the T_c around 68ºC, as expected (Figure 4.24.(e)).

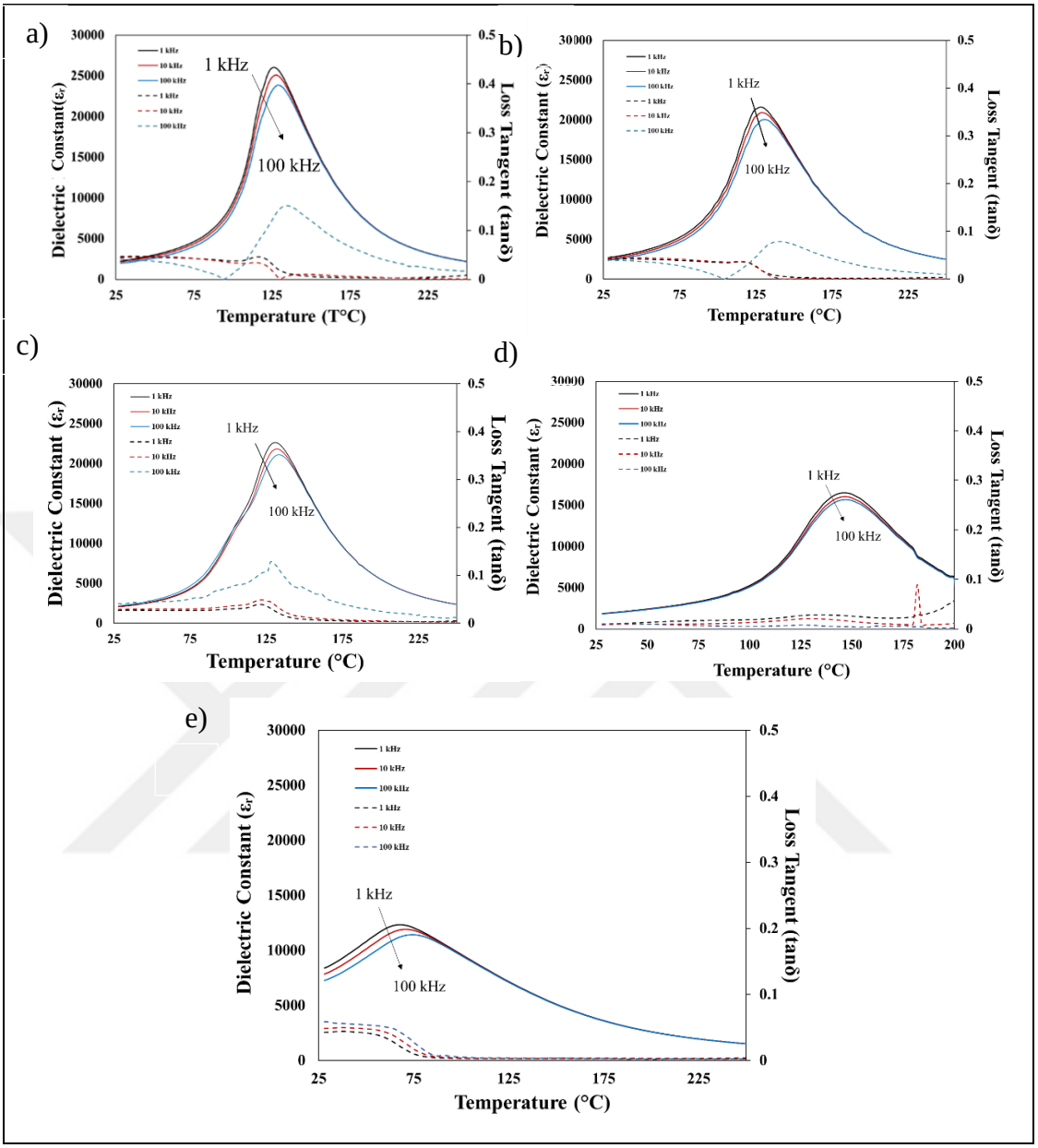

Figure 4.24: Comparison of dielectric constant and loss tangent vs. temperature plots of PMN-PT ceramic samples: a) Random, b) 5% mole BT sintered at 1150ºC for 4h, c) 5% mole BT sintered at 1200ºC for 4h d) 1% mole BT, e) 5% mole ST.

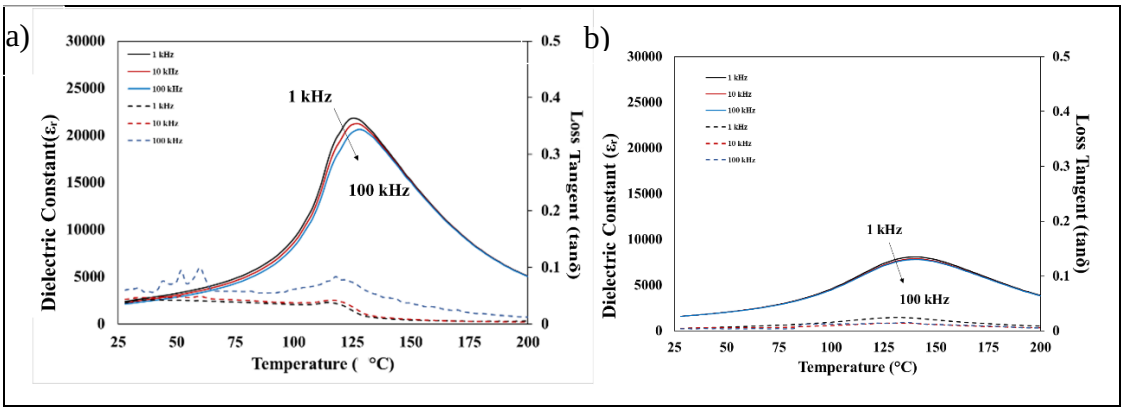

Figure 4.25: Comparison of dielectric constant and loss tangent vs. temperature plots of PMN-PT ceramic samples: a) Undoped and b) doped with 1% mole Mn.

Table 4.1: Dielectric properties of all tape-cast ceramic samples.

Samples	**T_c (°C)**	**Dielectric Constant (ε_r)**		**Loss Tangent (tanδ)**	
		@T_c	**@30°C**	**@T_c**	**@30°C**
Random	132	27972	2708	0.18	0.041
5% mole BT 1150°C-4h	128	21596	2776	0.019	0.041
5% mole BT 1200°C-4h	128	22352	2134	0.030	0.026
1% mole BT	148	16463	1923	0.025	0.008
5% mole ST	68	12333	8546	0.021	0.042
Undoped dry-pressed	126	21816	2350	0.038	0.039
1% mole Mn doped dry-pressed	142	8032	1644	0.022	0.005

As seen in Table 4.1, Mn addition was caused decreasing of the dielectric constant. Room temperature was taken as 30°C for the measurement results.

4.3.2. Bipolar and Monopolar Strain Measurement Results

In this section, strain curves vs. electric field measurements of all 0.72PMN-0.28PT ceramic samples were shown in Figure 4.26-Figure 4.32. All measurements were performed at 0.5 Hz (2000 ms) frequency.

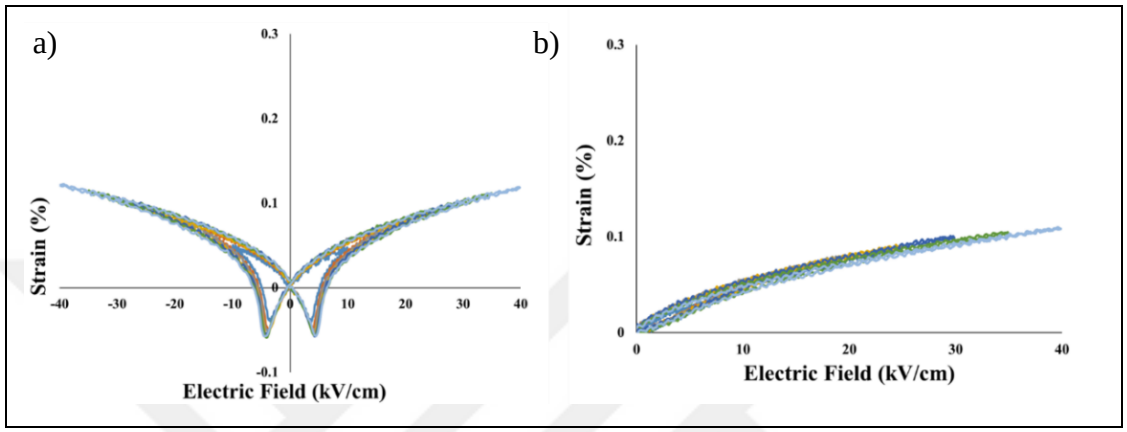

Figure 4.26: Comparison of strain vs. electric field plots of random PMN-PT ceramics. a) Bipolar and b) Unipolar.

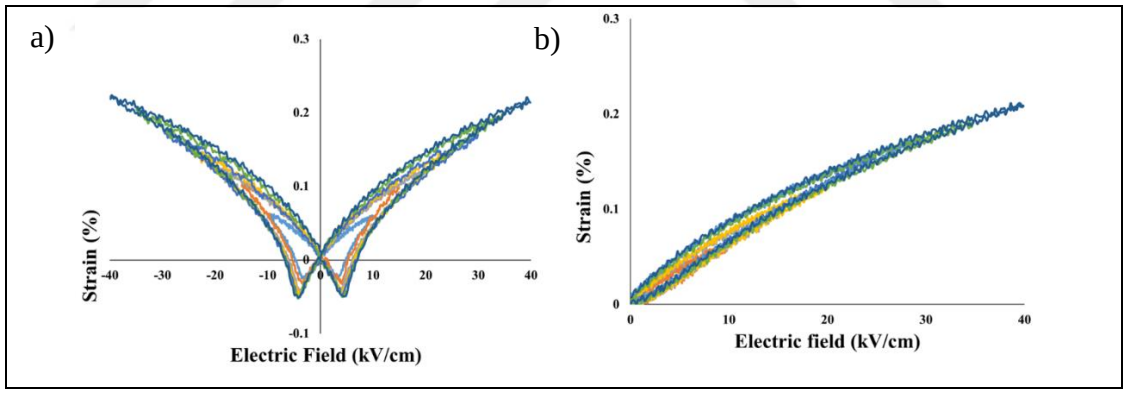

Figure 4.27: Comparison of strain vs. electric field plots of PMN-PT ceramic with 5% mole BT sintered at 1150ºC for 4h: a) Bipolar and b) Unipolar.

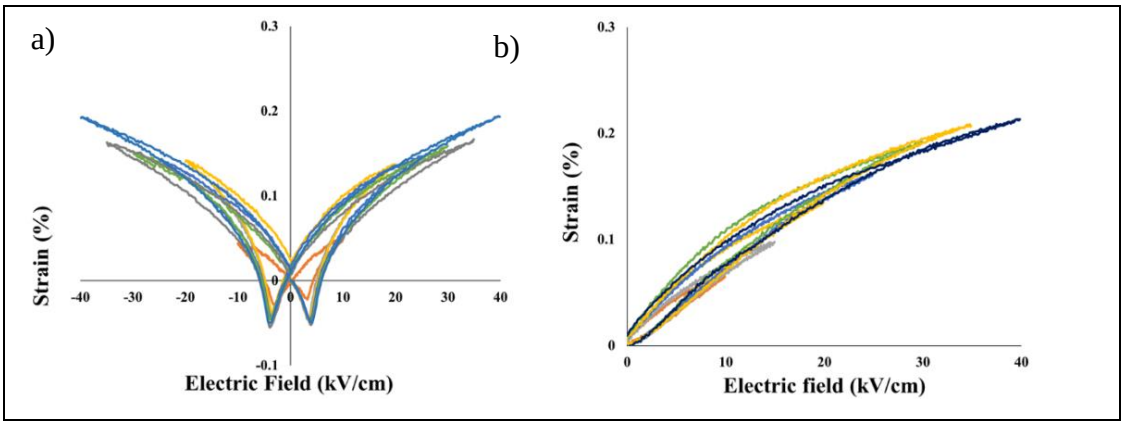

Figure 4.28: Comparison of strain vs. electric field plots of PMN-PT ceramic with 5% mole BT sintered at 1200ºC for 4h: a) Bipolar and b) Unipolar.

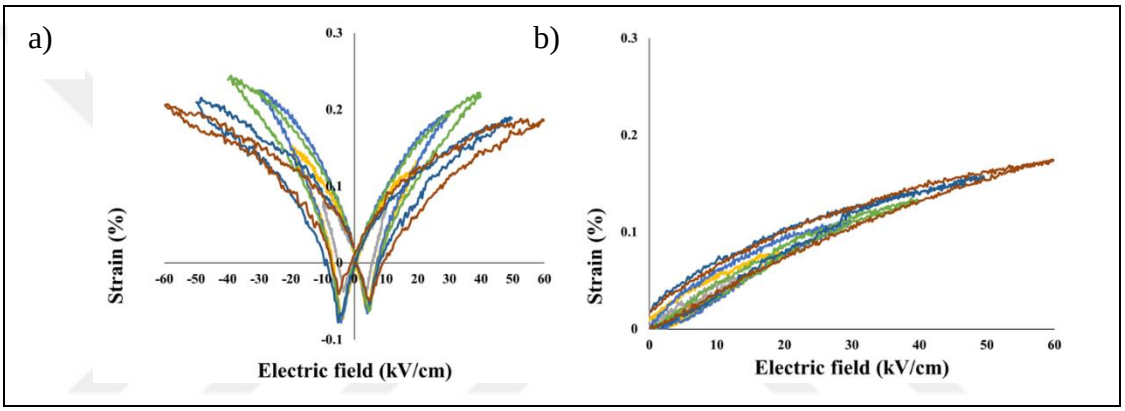

Figure 4.29: Comparison of strain vs. electric field plots of PMN-PT ceramics with with 5% mole BT sintered at 1200ºC for 8h: a) Bipolar and b) Unipolar.

Bipolar and unipolar, strain-electric field curves of 0.72PMN-O.28PT ceramics were obtained under applied 40 kV/cm electric field at 0.5Hz at RT which are shown in Figure 4.26-Figure 4.32. The level of the strain response increased by >20% with texturing. The strain level of the random sample measured under 60 kV/cm electric field was determined as 0.11% and the strain values increased to ~ 0.22% with texturing, as shown in Figure 4.30, and Table 4.2. These values indicated that texturing is rather effective in improving the electromechanical properties.

Table 4.2: Strain values of all tape-cast ceramic.

Sample	Strain (%) bipolar 40 kV/cm	Strain (%) unipolar 40 kV/cm	d_{33} (pC/N)	d_{33}^* (pm/V)
Random	0.11	0.10	340	250
5% mole BT-1150ºC-4h	0.21	0.20	390	500
5% mole BT-1200ºC-4h	0.19	0.21	375	475
5% mole BT-1200ºC-8h	0.22	0.13	360	325
1% mole BT	0.16	0.16	400	400
Undoped dry-pressed	0.24	0.25	300	625
1% mole Mn-dry-pressed	0.15	0.14	270	350

The piezoelectric charge coefficient, d_{33}, of random sample was measured as 340 pC/N by Berlincourt method, while it was measured as 390, 375, 360, and 400 pC/N for textured samples, respectively, as shown in Table 4.2.

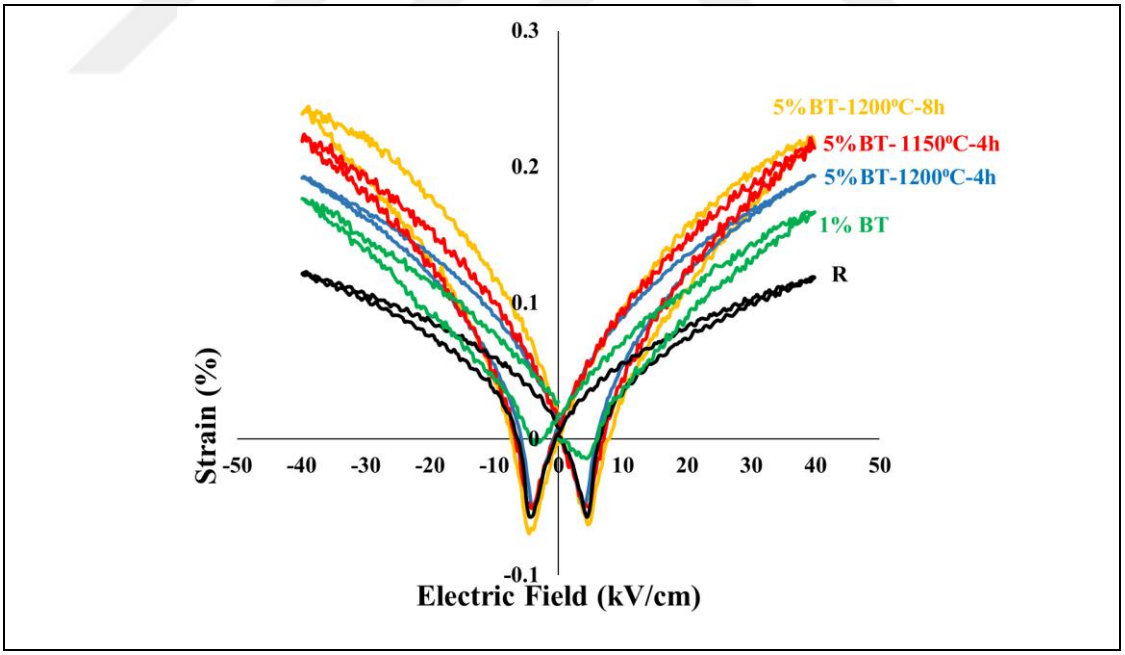

Figure 4.30: Comparison of bipolar strain vs. electric field plot of all tape-cast PMN-PT ceramics.

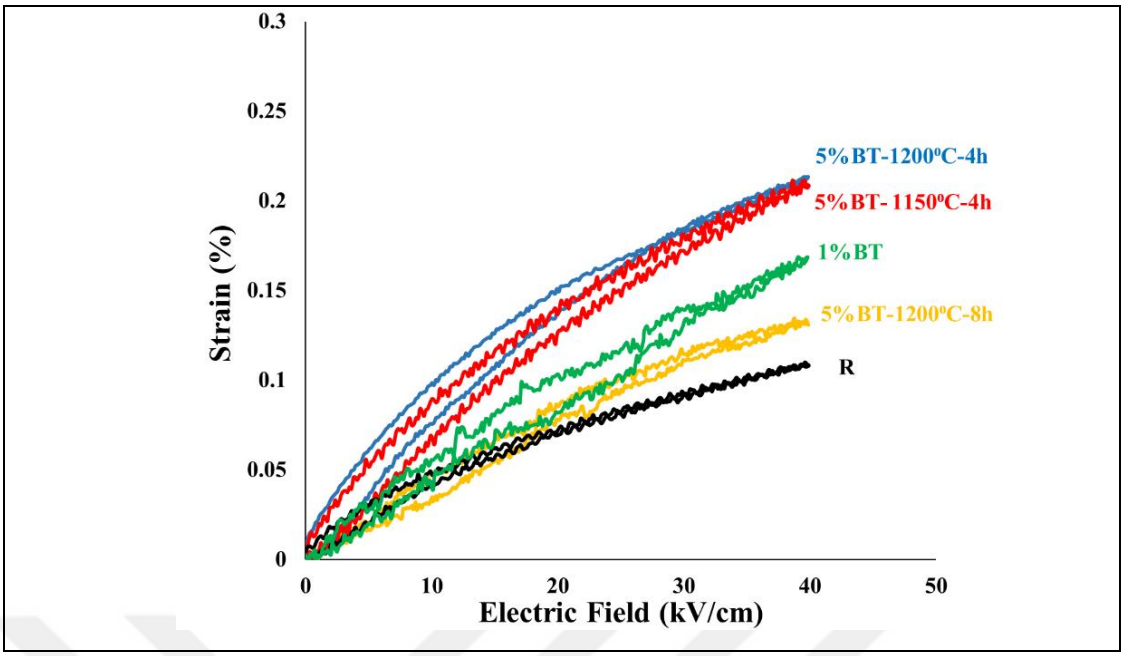

Figure 4.31: Comparison of unipolar strain vs. electric field plot of all tape-cast ceramics.

In Figure 4.30 and Figure 4.31, comparison of bipolar and unipolar strain vs. electric field loops of random (R) and textured samples were given. The textured PMN-PT thick films (ceramic) with 5% mole BT addition were exhibited the highest strain values. 1% mole Mn addition was not provided positive effect on the electromechanical properties of PMN-PT as seen in Figure 4.32.

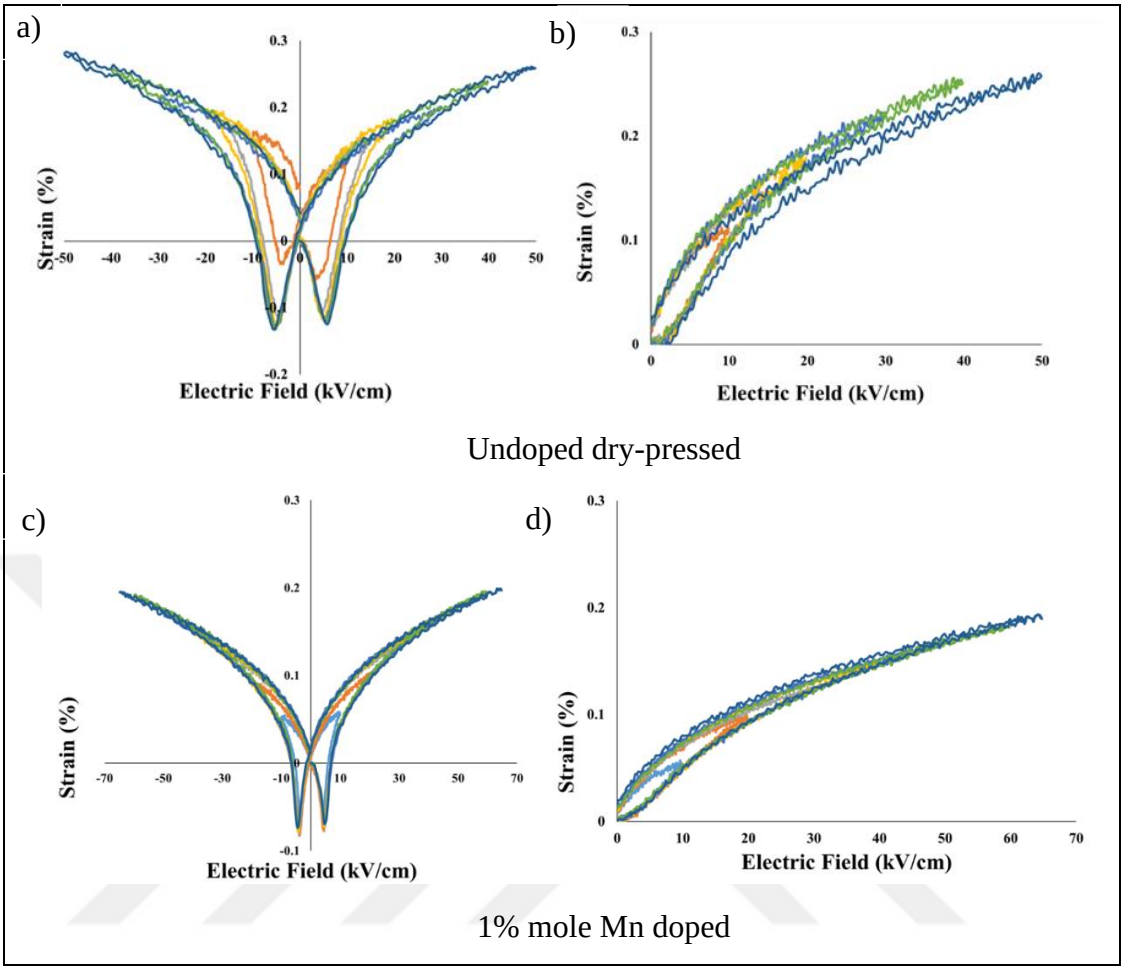

Figure 4.32: Comparison of bipolar and unipolar strain vs. electric field plots of PMN-PT ceramics: a-b) undoped and c-d) 1% mole Mn doped.

4.3.3. Electrocaloric Measurement Results and Analyses

In this section of the thesis, temperature - dependent polarization-electric field (P-E) hysteresis plots of the random, textured, undoped dry-pressed, Mn doped dry-pressed 0.72PMN-0.28PT ceramics were measured from 90ºC to 25ºC under 60 kV/cm applied electric field. Further investigations and analyses of the electrocaloric response and the results of these measurements were done with Prof. Dr. İ. Burç Mıaırlıoğlu and Assoc. Prof. M. Barış Okatan. The values of the electrocaloric response, the adiabatic temperature change - ΔT_{EC}, and the isothermal entropy change - ΔS, for all 0.72PMN-0.28PT ceramics were analyses and calculated from the P-E measurement plots which were shown in Figure 4.33 - Figure 4.40. The measurement was taken from 90ºC to 25ºC in the cooling regime and by waiting 10 minutes at each temperature

before each measurement. The values of maximum polarization (P_{max}), remnant polarization (P_r), and coercive electric field (E_c) increased by decreasing of the measurement temperature, as shown in Table 4.3 and Table 4.4.

P-E, ΔT_{EC}-T, $\partial P/\partial T$ pyroelectric coefficient graphs for all ceramics were given in Figure 4.33- Figure 4.40. The maximum ΔT value of random ceramics sample was measured as 0.45K at 80ºC under applied 60 kV/cm electric field (Figure 4.33). This result was similar with previous PMN-0.30PT research by Rozic et al.,2011[25] which is a very close composition to our current study. However, in our study, ΔT_{EC} values of samples were close to each other, but textured samples indicated slightly higher polarization values than random ones. Generally, ΔT_{EC} values are to be maximum levels close to the phase transition temperature which is around ~ 130ºC in the current case. Therefore, it forced limits of our laboratory device. Furthermore, for ferroelectrics with perovskite structure the highest ΔT_{EC} values were reported as 2-3K under applied electric field between 60-90 kV/cm [25].

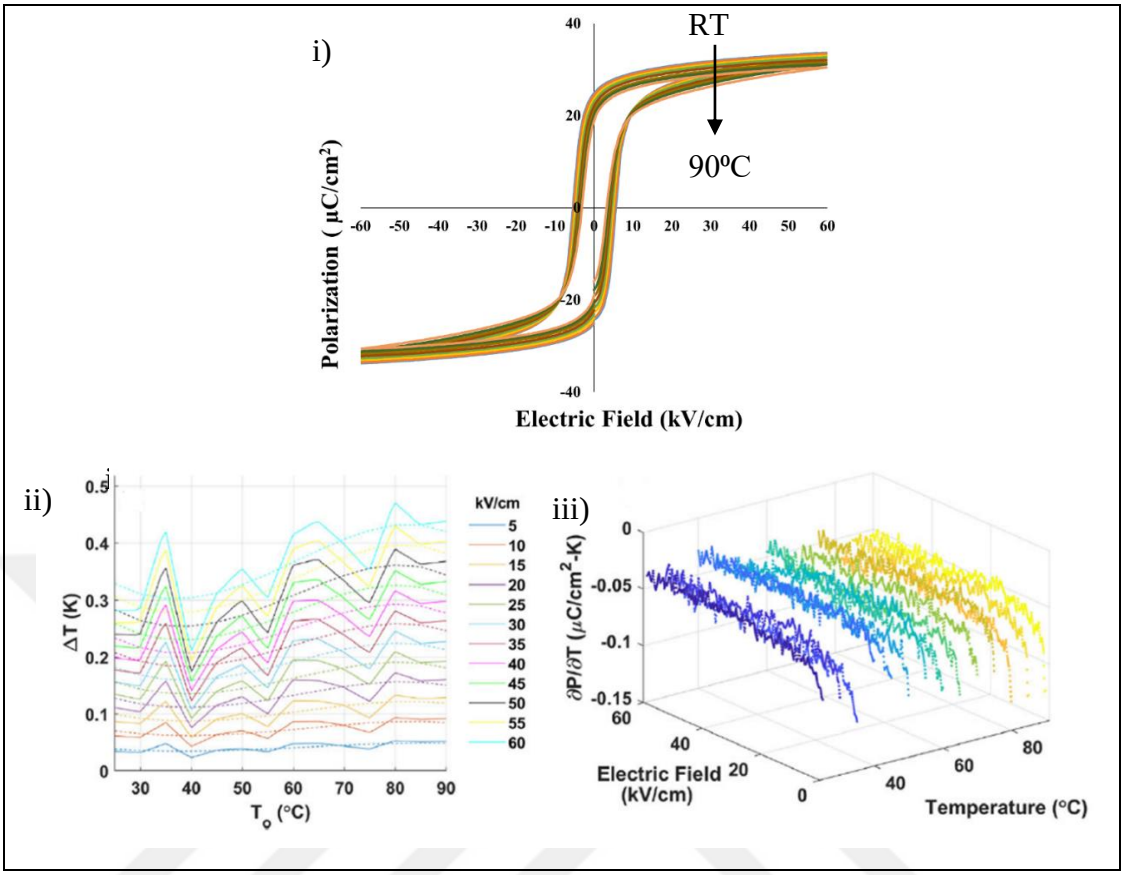

Figure 4.33: Results of random sample at measured at 60 kV/cm-2000 ms: i) Polarization vs. electric field ii) ΔT vs. temperature and iii) Pyroelectric coefficient vs. temperature plots.

For the random sample of PMN-0.28PT ceramic was sintered at 1150ºC for 4 hours, the measured value of P_{max} is approximately ~ 33.00 μC/cm^2, the value of P_r is ~ 24.04 μC/cm^2, and the value of E_c is ~ 4.99 kV/cm at RT. At 90ºC, P_{max} is ~ 30.53 μC/cm^2, P_r is ~19.52 μC/cm^2, and E_c is ~ 3.43 kV/cm for the sample, as shown in Table 4.3. and Table 4.4. As mentioned before, with increasing temperature, P_{max}, P_r, and E_c values slightly decreased. Pyroelectric coefficient measurements and analyses were also done at different electric field and temperature. Then $\Delta T - T$ values were calculated. The ΔT_{EC} values were about ~ 0.35 -0.5K at 25ºC-90ºC temperature regime.

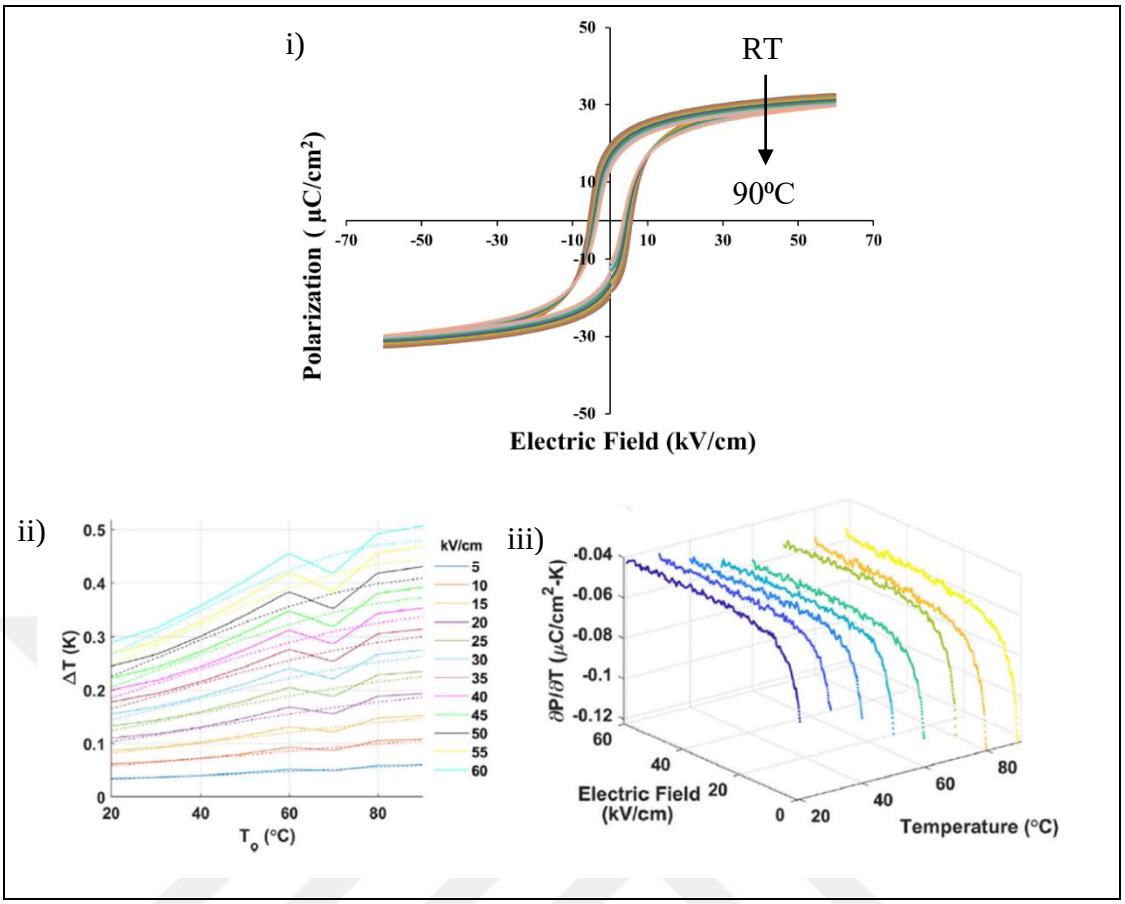

Figure 4.34: Results of textured sample with 5% mole BT sintered at 1150ºC for 4h, measured at 60 kV/cm-2000 ms: i) Polarization vs. electric field, ii) ΔT vs. temperature, and iii) Pyroelectric coefficient vs. temperature plots.

The textured sample with 5% mole BT addition of PMN-0.28PT ceramic was sintered at 1150ºC for 4 hours, the measured value of P_{max} is approximately ~ 32.65 µC/cm^2, the value of P_r is ~ 18.98 µC/cm^2, and the value of E_c is ~ 6.74 kV/cm, at RT. At 90ºC; P_{max} is ~ 29.70 µC/cm^2, P_r is ~ 13.63 µC/cm^2, and E_c is ~ 3.49 kV/cm for the sample, as shown in Table 4.3. and Table 4.4. As mentioned before, with increasing temperature, P_{max}, P_r, and E_c values slightly decreased. Pyroelectric coefficient measurements and analyses were also done at different electric field and temperature. Then $\Delta T - T$ values were calculated. The ΔT_{EC} values were about ~ 0.35 − 0.5K, as shown in Figure 4.34 at 25ºC-90ºC temperature regime.

Conventional caloric materials exhibit ΔT >0, ΔS<0 and reverse caloric materials exhibit ΔT<0, ΔS >0, respectively [16]. Textured samples sintering at 1200ºC for 4 hours and 8 hours shows negative and positive ΔT results as shown in Figures 4.35-Figure 4.36. Additionally, sintered at1200ºC for 4 h textured sample has

exhibited highest P_{max}, P_r values comparing to other textured, random, and dry-pressed samples.

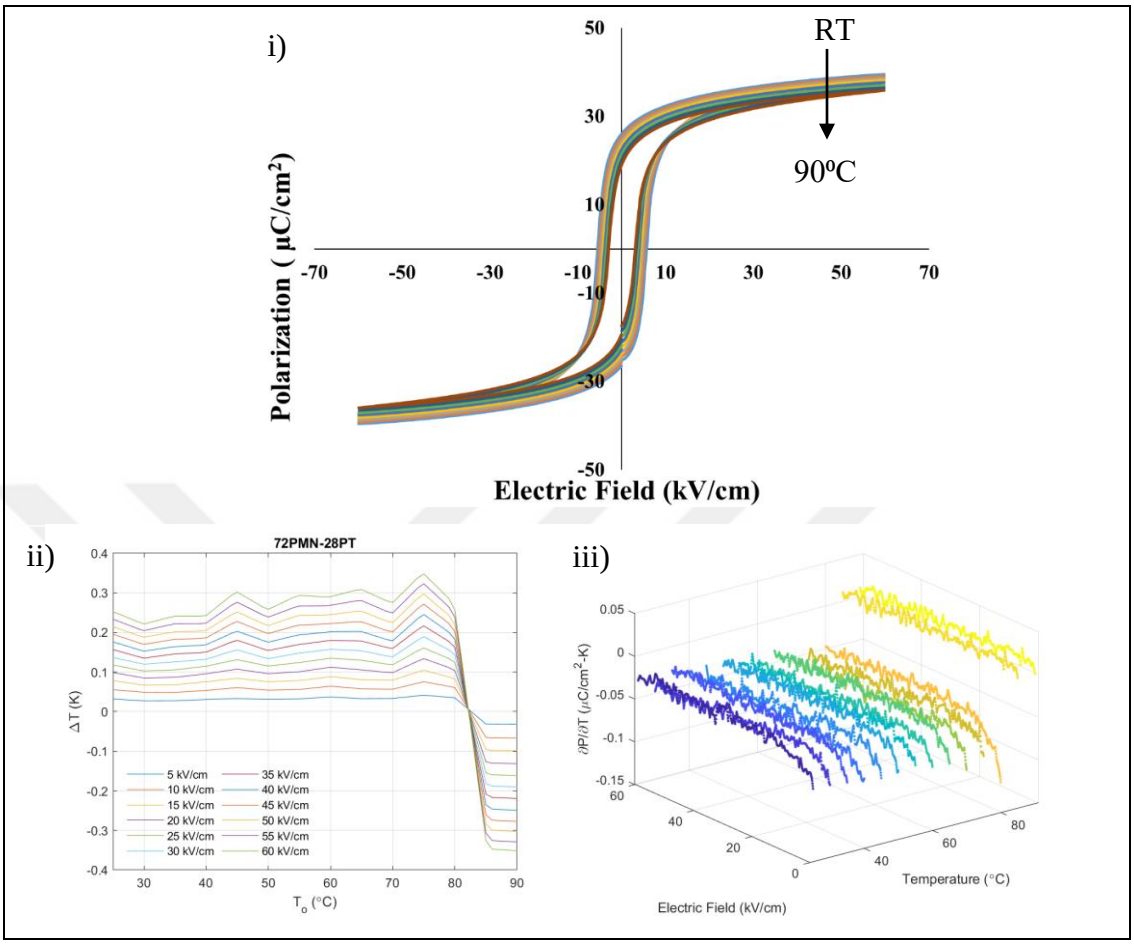

Figure 4.35: Results of textured samples with 5% mole BT, sintered at 1200ºC for 4h, measured at 60 kV/cm-2000 ms: i) Polarization vs. electric field, ii) ΔT vs. temperature, and iii) Pyroelectric coefficient vs. temperature plots.

Textured sample with 5% mole BT addition of PMN-0.28PT ceramic was sintered at 1200ºC for 4 hours, the measured value of P_{max} is approximately ~ 39.12 μC/cm^2, the value of P_r is ~ 25.52 μC/cm^2, and the value of E_c is ~6.74 kV/cm at RT. At 90ºC; P_{max} is ~ 35.94 μC/cm^2, P_r is ~19.04 μC/cm^2, and E_c is ~ 3.38 kV/cm, as shown in Figure 4.35. As mentioned before, with increasing temperature, P_{max}, P_r, and E_c values slightly decreased shown in Table 4.3 and Table 4.4.

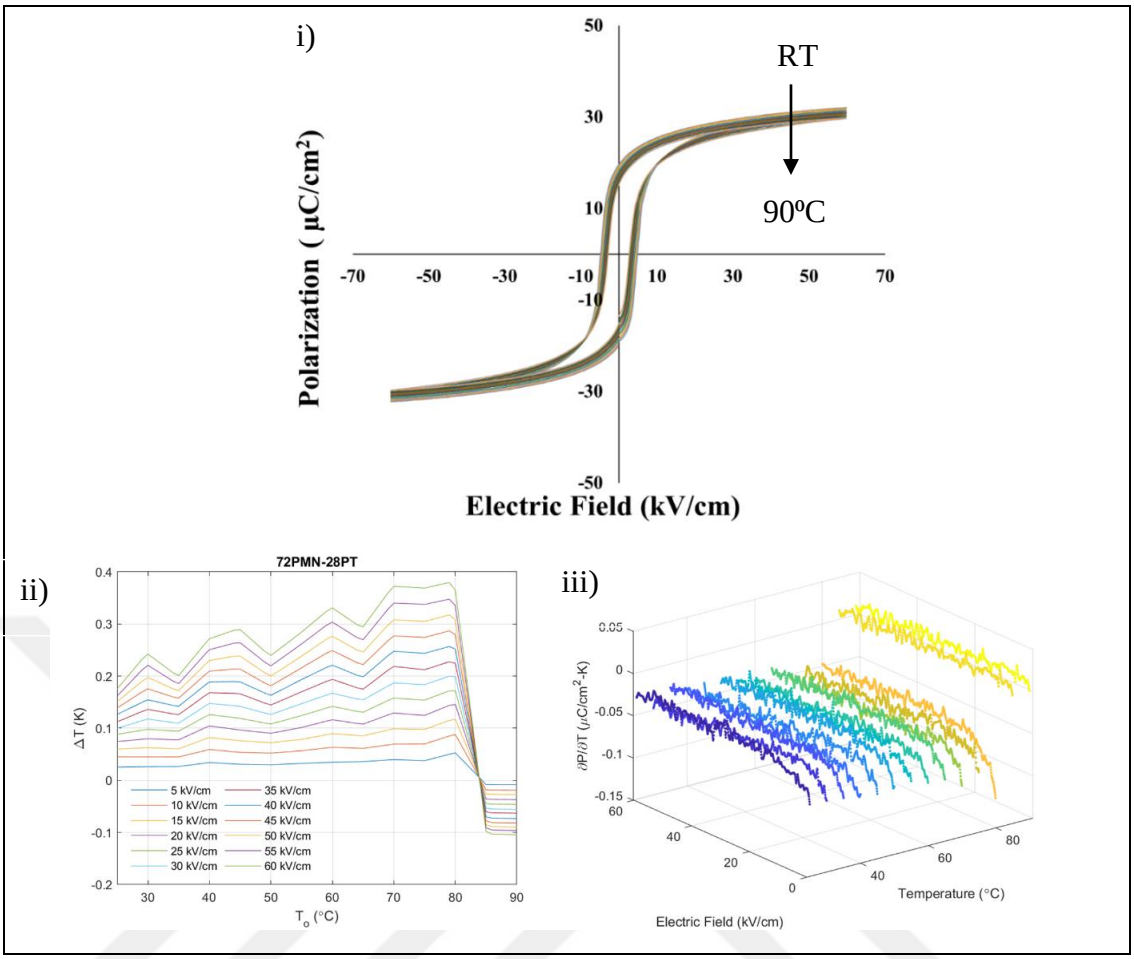

Figure 4.36: Results of textured sample with 5% mole BT, sintered at 1200ºC for 8h, measured at 60 kV/cm-2000 ms: i) Polarization vs. electric field, ii) ΔT vs. temperature, and iii) Pyroelectric coefficient vs. temperature plots.

The textured sample with 5% mole BT addition of PMN-0.28PT ceramic was sintered at 1200ºC for 8 hours measured values of P_{max} is ~ 32.02 µC/cm^2, P_r is ~ 18.50 µC/cm^2, and E_c is ~ 6.50 kV/cm at RT. At 90ºC, P_{max} ~ 29.75 µC/cm^2, P_r ~ 14.83 µC/cm^2, and E_c ~ 3.00 kV/cm, as shown in Table 4.3. and Table 4.4. As mentioned before, with increasing temperature P_{max}, P_r, and E_c values slightly decreased, shown in Table 4.3 and Table 4.4. The ΔT_{EC} values were about ~ 0.8K, as shown in Figure 4.36 at 25ºC-90ºC temperature range.

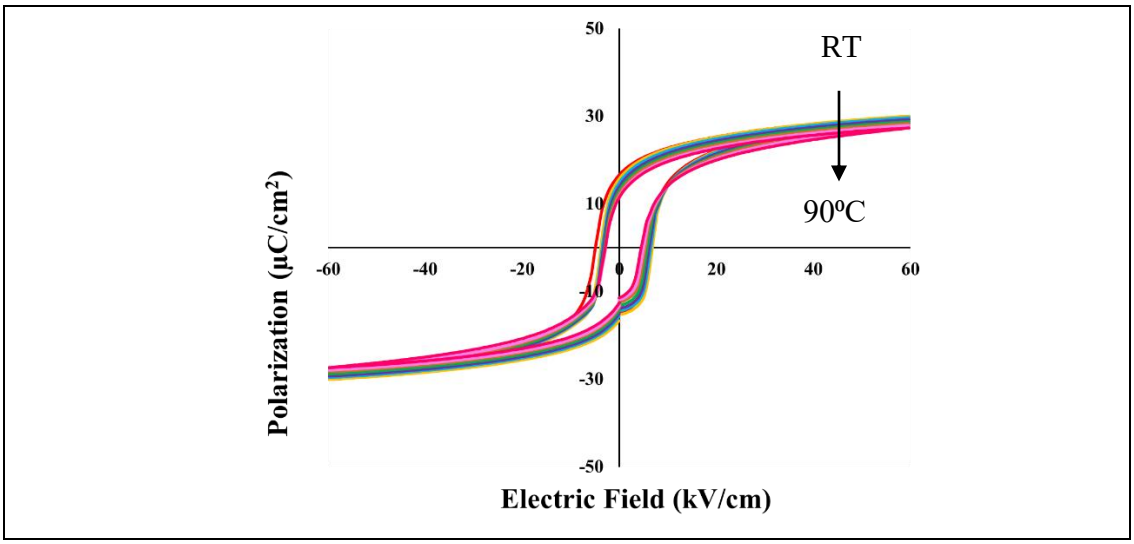

Figure 4.37: Results of textured sample with 1% mole BT, sintered at 1200ºC for 4h, measured at 60 kV/cm-2000 ms: Polarization vs. electric field plot.

The textured sample with 1% mole BT addition measured values of P_{max} is ~ 25.20 µC/cm^2, P_r is ~ 11.52 µC/cm^2, and E_c is ~5.3 kV/cm at RT. At 90ºC, P_{max} ~ 22.68 µC/cm^2, P_r ~ 7.9 µC/cm^2, and E_c ~ 3.64 kV/cm. As expected, with increasing temperature, P_{max}, P_r, and E_c values slightly decreased, as shown in the Table 4.3. and Table 4.4, and Figure 4.37.

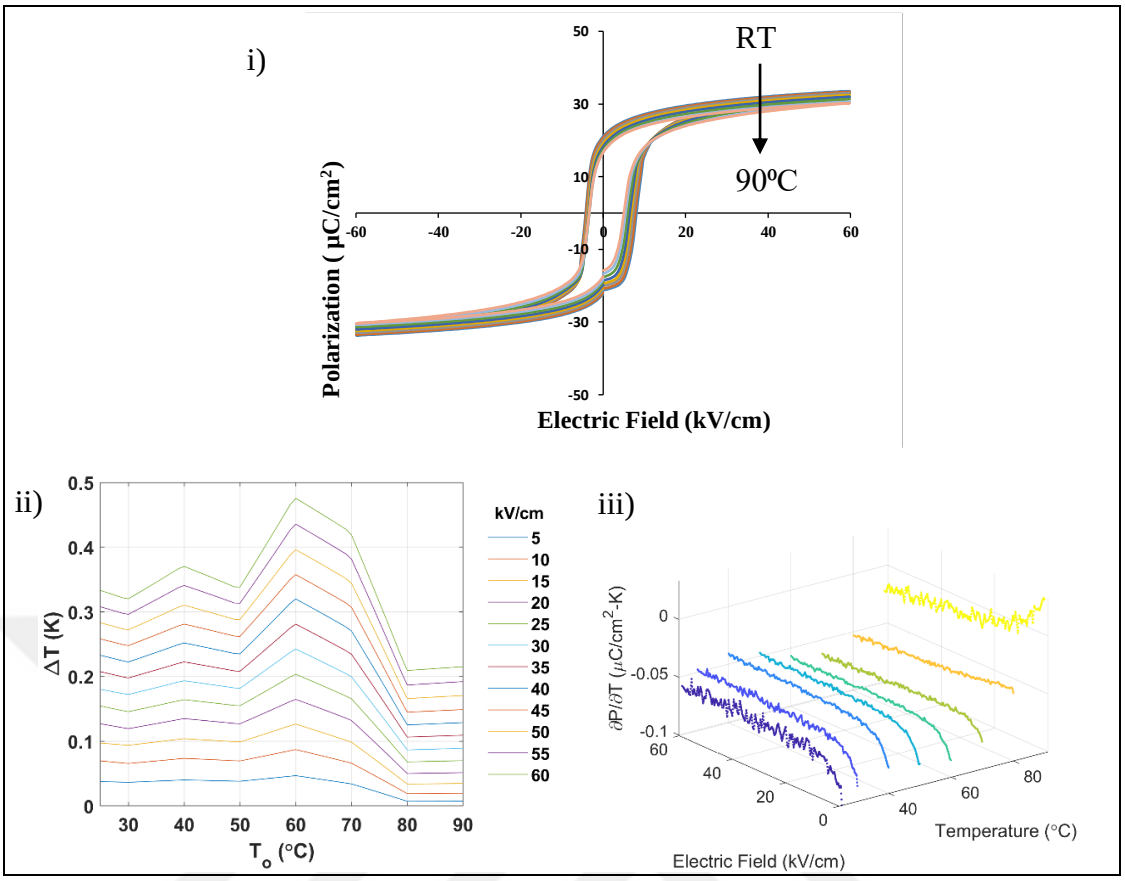

Figure 4.38: Results of undoped dry-pressed sample, sintered at 1150ºC for 4h measured at 60 kV/cm-2000 ms: i) Polarization vs. electric field, ii) ΔT vs. temperature, and iii) Pyroelectric coefficient vs. temperature plots.

The undoped dry-pressed sample of PMN-0.28PT ceramic the exhibited values of P_{max} is ~ 33.55 µC/cm^2, the value of P_r is ~ 21.13 µC/cm^2, and the value of E_c is ~ 8.16 kV/cm at RT. At 90ºC, P_{max} ~ 30.34 µC/cm^2, P_r ~17.25 µC/cm^2, and E_c ~ 5.45 kV/cm, as seen in Table 4.3. and Table 4.4. As mentioned before, with increasing temperature, P_{max}, P_r, and E_c values slightly decreased. The ΔT_{EC} values were about ~ 0.35K - 0.5K, as shown in Figure 4.38 at 25ºC – 90ºC temperature range.

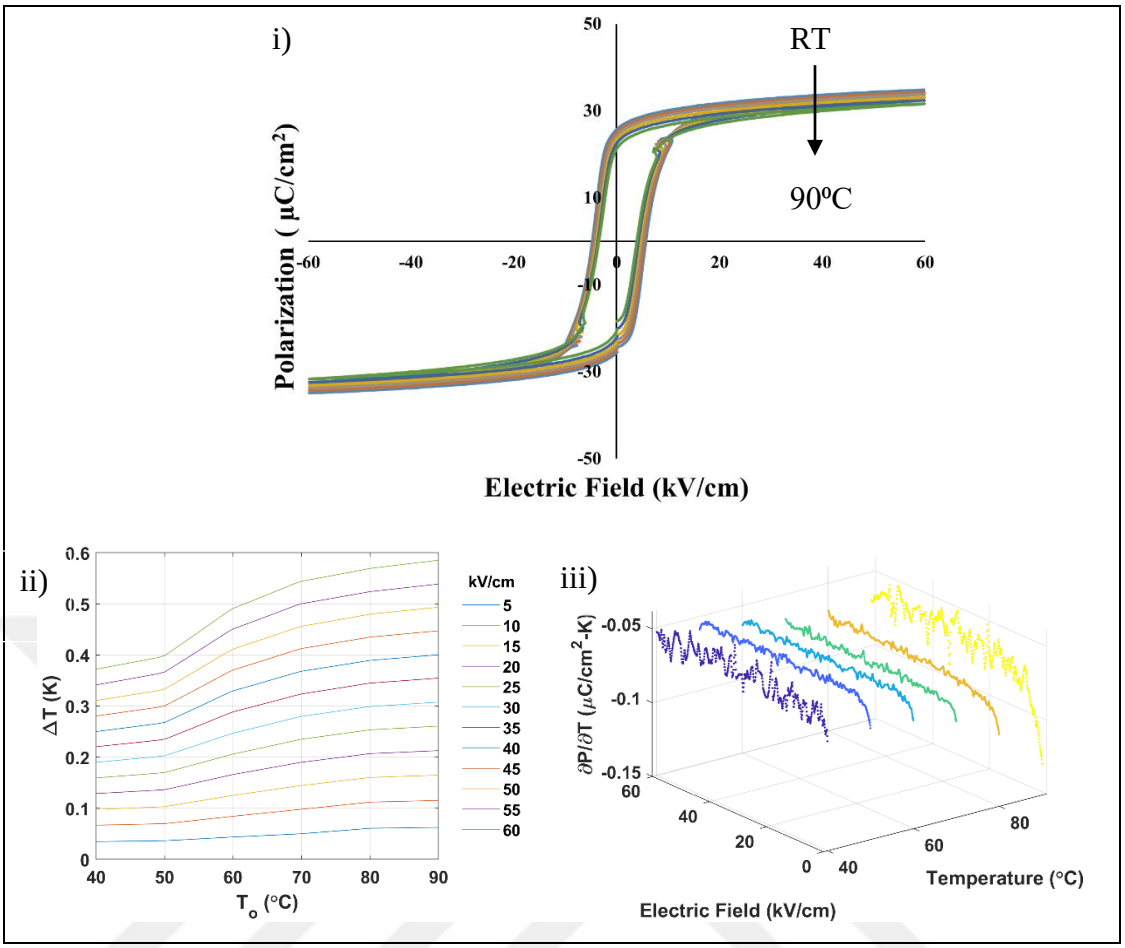

Figure 4.39: Results of 0.5% mole Mn dry-pressed sample measured at 60 kV/cm-1000 ms: i) Polarization vs. electric field, ii) ΔT vs. temperature, iii) Pyroelectric coefficient vs. temperature plots.

The 0.5% mole Mn doped dry-pressed sample of PMN-0.28PT ceramic measured values of P_{max} is ~ 35.32 µC/cm^2, the value of P_r is ~ 24.56 µC/cm^2, and the value of E_c is ~ 5.15 kV/cm at RT. At 90ºC, P_{max} ~ 31.66 µC/cm^2, P_r ~21.00 µC/cm^2, and E_c ~ 4.21 kV/cm, as seen in the Table 4.3. and Table 4.4. As mentioned before, with increasing temperature, P_{max}, P_r, and E_c values slightly decreased. The ΔT_{EC} values were about ~ 0.35 − 0.6K, as shown in Figure 4.39.

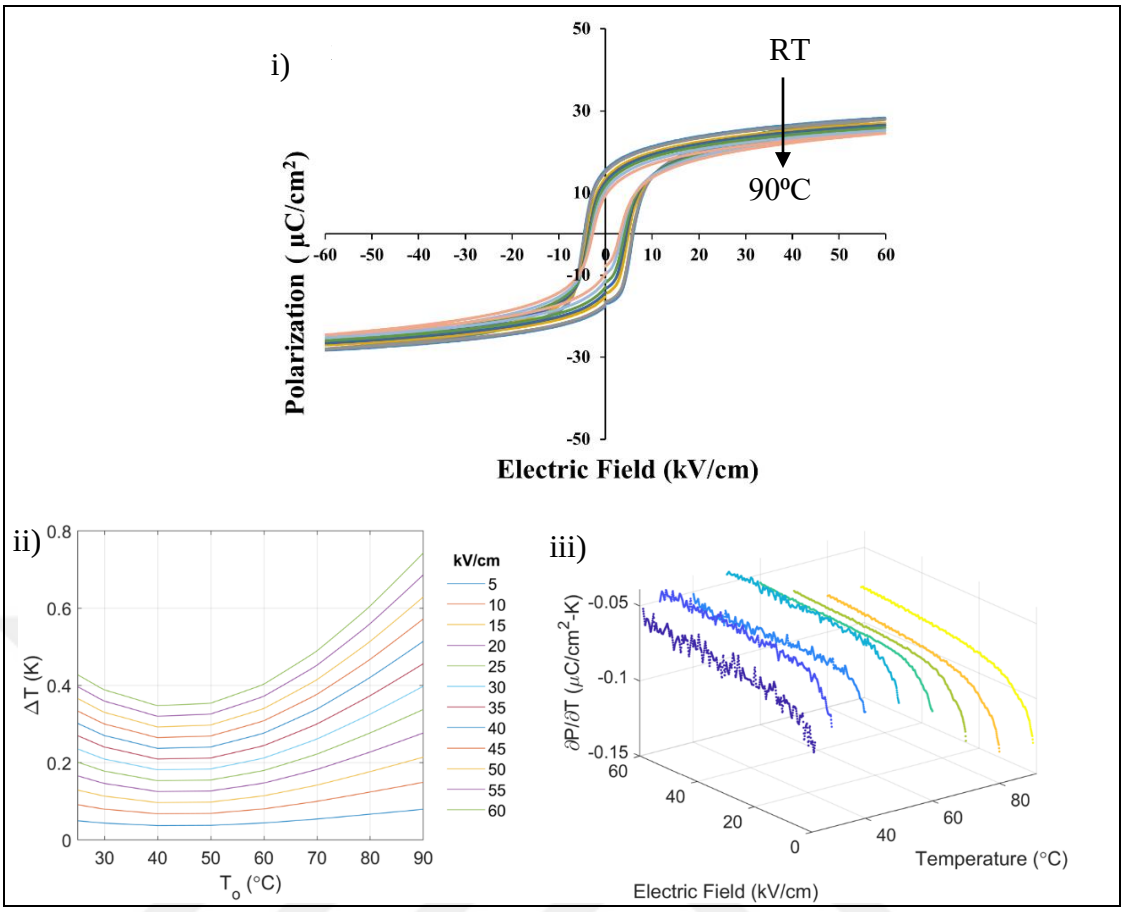

Figure 4.40: Results of 1% mole Mn doped dry-pressed sample measured at 60 kV/cm-2000 ms: i) Polarization vs. electric field, ii) ΔT vs. temperature and iii) Pyroelectric coefficient vs. temperature plots.

The 1% mole Mn doped dry-pressed sample of PMN-0.28PT ceramic measured values of P_{max} is ~ 27.98 µC/cm^2, the value of P_r is ~ 14.00 µC/cm^2, and the value of E_c is ~4.50 kV/cm at RT. At 90ºC, P_{max} ~24.54 µC/cm^2, P_r ~9.15 µC/cm^2, and E_c ~ 2.98 kV/cm, as shown in Table4.3. and Table4.4. As mentioned before, with increasing temperature, P_{max}, P_r, and E_c values slightly decreased, as shown in Table 4.3 and Table 4.4. The ΔT_{EC} values were about ~0.4 − 0.8K, as shown in Figure 4.40.

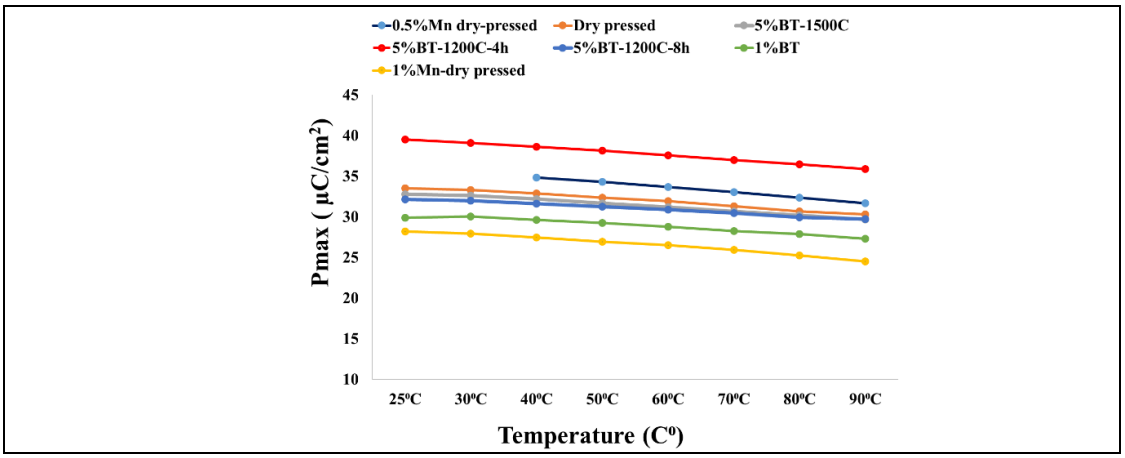

Figure 4.41: All samples P_{max} values vs. temperature plot.

Table 4.3: Electrical measurement values of all samples at 25ºC.

Samples	**P_{max} ($\mu C/cm^2$)**	**P_r ($\mu C/cm^2$)**	**E_c kV/cm)**
Random	33.00	24.04	4.99
5% mole BT-1150ºC-4h	32.65	18.98	2.44
5% mole BT-1200ºC-4h	39.12	25.52	6.74
5% mole BT-1200ºC-8h	32.02	18.50	6.50
1% mole BT-1150ºC-4h	30.00	16.66	5.84
Undoped dry pressed	33.55	21.13	8.16
0.5% mole Mn dry-pressed	35.32	24.56	5.15
1% mole Mn dry-pressed	27.98	14	4.50

Table 4.4: Electrical measurement values of all samples at 90ºC.

Samples	**P_{max} ($\mu C/cm^2$)**	**P_r ($\mu C/cm^2$)**	**E_c (kV/cm)**
Random	30.53	19.52	3.43
5% mole BT-1150ºC-4h	29.70	13.63	3.49
5% mole BT-1200ºC-4h	35.94	19.04	3.38
5% mole BT-1200ºC-8h	29.75	14.83	3.00
1% mole BT-1150ºC-4h	27.36	11.23	4.40
Undoped dry-pressed	30.34	17.25	5.45
0.5% mole Mn doped dry-pressed	31.66	21.00	4.21
1% mole Mn doped dry-pressed	24.54	9.15	2.98

The summarized P_{max} vs. T graph for all samples were given in Figure 4.41 and electrical measurement results such as P_{max}, P_r and E_c were also given in Table 4.3. and Table 4.4 for 25ºC 90ºC, respectively.

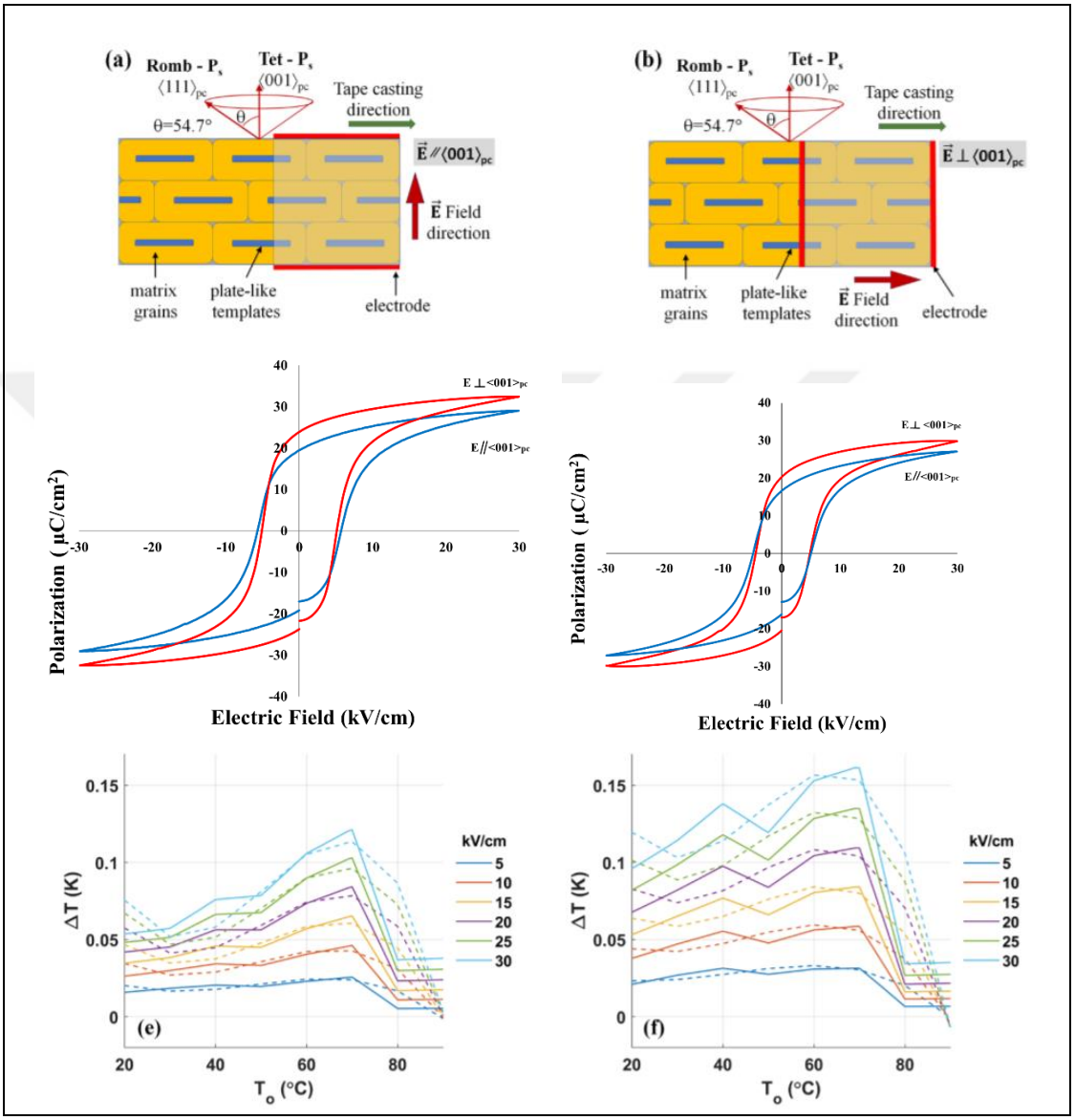

Figure 4.42: Electrocaloric measurement results of textured 0.72PMN-0.28PT samples applied electric field, parallel and perpendicular to <001>$_{pc}$ directions.

Rhombohedral symmetry included PMN-PT system single crystals were investigated of the anisotropy of ECE, some previous results presented that cut along <111>$_{pc}$ direction showed slightly higher ECE values than cut along <110>$_{pc}$ and <100>$_{pc}$ directions recorded in the literature [26, 27]. The texture samples in this study had crystallographic grain orientation through <001>$_{pc}$ direction was produced. Two

sets of texture samples were prepared to compare applied electric field direction due to grain orientation direction. One of the texture samples were grain oriented along the $<001>_{pc}$ direction, silver electrode coated onto the sample surface which is parallel to template grain growth direction as shown in Figure 4.42.a), then applied electric field parallel to orientation direction $E \parallel <001>_{pc}$. The second sample of the texture was grain-oriented $<001>_{pc}$ direction as well, the differences from previous texture sample is applied electric field was perpendicular the template orientation $E \perp <001>_{pc}$ shown in Figure 4.42.b). However, the result of these two texture samples comparison was, $E \perp <001>_{pc}$ texture sample response slightly higher P_{max}, P_r, E_c in Polarization-Electric field hysteresis loops as shown in Figure 4.42. and this figure was taken research paper [28]. $E \perp < 001 >_{pc}$ texture sample indicated little higher ΔT values depending on the temperature in electrocaloric effect than the $E \parallel < 001 >_{pc}$ texture sample as shown in Figure 4.42 third plots [28].

5. CONCLUSION

As a conclusion drawn from all results:

When the PMN-PT textured ceramics with BT template were compared to each other, the sample which was sintered at 1200ºC for 4 hours with about ~60% Lotgering factor has the highest ECE measurement results in terms of P_r, P_{max}, and E_c level than other BT textured samples with Lotgering factors of ~80%, 96%. On the other hand, dielectric vs. temperature, strain vs. electric field (bipolar-unipolar) measurements were found too similar to each other. These results show that the degree of grain orientation, as represented by the Lotgering factor, does not have a drastic effect on the dielectric and piezoelectric behaviors. Also, it was verified that the ΔT_{EC} values of P-E hysteresis loops increased with increasing applied electric field to the PMN-0.28PT ceramics in this study.

When we are compared the undoped, 0.5% mole Mn, 1% mole Mn-doped, and then dry-pressed samples; it is clear that Mn dopant addition affected the Curie temperature and dielectric constant level. As seen in the dielectric constant vs. temperature measurement, the Curie temperature of the 1% mole Mn-doped samples were ~8ºC higher, and the dielectric constant level was lower than the undoped dry-pressed samples. In the ECE measurement, the 0.5% mole and 1% mole Mn-doped samples have smoother ΔT vs. T variation compared to the undoped one. This was believed to be due to the defect dipoles that arise because of multivalent Mn doping, their accumulation around domain walls as a result of cyclic application of electric field, and finally, pinning the domain wall motion.

The random, tape-cast sample has the highest dielectric constant level compared to all other samples. This might possibility be due to the higher density of the tape-cast samples and homogeneity in the structure of the 0.72PMN-0.28PT sample.

The textured samples with ST templates have lower Curie temperature (~68ºC) and dielectric constant with high-frequency dependence. However, it was not possible to conduct any ECE and bipolar, unipolar measurement due to the fragile nature of the samples. After a few electric field cycles, the 5% mole ST textured samples were found to dielectric breakdown. Additionally, the ST templates were not observed in any SEM micrographs. The reason for this might be related to the processing of the ST template

or the low melting point of the ST template, therefore, during the sintering process ST vanished from the structure.

The investigation of the effect of electric field anisotropy indicated that when the electric field was applied perpendicular to the texture direction, i.e., $E\perp<001>_{pc}$, then the texture sample yielded slightly higher P_{max}, P_r, E_c in Polarization-Electric field hysteresis loops as shown in Figure 4.29. Additionally, the $E\perp< 001 >_{pc}$ sample yielded slightly higher ΔT values depending on the temperature in electrocaloric effect compared to the $E\parallel< 001 >_{pc}$ sample.

REFERENCES

[1] Moulson A. J., Herbert J. M., (2003), "Electroceramics: materials, properties, applications", 2nd edition, John Wiley & Sons.

[2] Setter N., Waser R. (2000). "Electroceramic materials", Acta materialia, 48(1), 151-178.

[3] Li J., Liu Y., Zhang Y., Cai H. L., Xiong R. G. (2013), "Molecular ferroelectrics: where electronics meet biology", Physical Chemistry Chemical Physics, 15(48), 20786-20796.

[4] Ciubotariu A., (2016), "Design, Modeling, Fabrication and Control of PMN-PT Piezoelectric Systems", Doctoral dissertation, Université de Franche-Comté.

[5] Newnham R. E., (2005), "Properties of Materials-Anisotropy, Symmetry and Structure", Oxford University Press.

[6] Jong M., Chen W., Geerlings H., Asta M., Persson K. A., (2015), "A database to enable discovery and design of piezoelectric materials", Scientific Data, 2, 150053.

[7] Damjanovic D., (1998), "Ferroelectric, dielectric and piezoelectric properties of ferroelectric thin films and ceramics", Reports on Progress Physics, 61, 1267-1324.

[8] Kao C. K., (2004), "Dielectric Phenomena in Solids: With Emphasis on Physical Concepts of Electronic Processes", 1st Edition, Elsevier Academic Press.

[9] Safari A., Akdogan E. K., (2008), "Piezoelectric and Acoustic Materials for Transducer Applications", Springer Science & Business Media.

[10] Liu G., Zhang S., Jiang W., Cao W., (2015), "Losses in Ferroelectric Materials", Materials Science and Engineering: R: Reports, 89, 1-48.

[11] Cowley R. A., Gvasaliya S. N., Lushnikov S. G., Roessli B., Rotaru G. M., (2011), "Relaxing With Relaxors: a Review of Relaxor Ferroelectrics'', Advances in Physics, 60(2), 229-327.

[12] Genenko Y. A., Glaum J., Hoffmann M. J., Albe K., (2015), "Mechanisms of Aging and Fatigue in Ferroelectrics'', Materials Science and Engineering: B, 192, 52-82.

[13] Fu D., Taniguchi H., Itoh, M., Mori S. (2012), "Pb ($Mg_{1/3}Nb_{2/3}$) O_3 (PMN) Relaxor: Dipole Glass or Nano-Domain Ferroelectric'', Advances in Ferroelectrics, 3(8).

[14] Li F., Zhang S., Damjanovic D., Chen L. Q., Shrout T. R., (2018), "Local Structural Heterogeneity and Electromechanical Responses of Ferroelectrics: Learning from Relaxor Ferroelectrics'', Advanced Functional Materials, 28(37), 1801504.

[15] Seok S. I., Guo T. F., (2020), "Halide Perovskite Materials and Devices. MRS Bulletin'', 45(6), 427-430.

[16] Trolier-McKinstry S., (2008), "Crystal Chemistry of Piezoelectric Materials'', In Piezoelectric and Acoustic Materials for Transducer Applications, (pp. 39-56). Springer, Boston, MA.

[17] Alpay S. P., Mantese J., Trolier-McKinstry S., Zhang Q., Whatmore R. W., (2014), "Next-Generation Electrocaloric and Pyroelectric Materials for Solid-State Electrothermal Energy Interconversion'', Mrs Bulletin, 39(12), 1099-1111.

[18] Du H., Chang Y., Li C., Hu Q., Pang J., Sun Y., Jin L., (2019), "Ultrahigh Room Temperature Electrocaloric Response in Lead-Free Bulk Ceramics Via Tape Casting'', Journal of Materials Chemistry C, 7(23), 6860-6866.

[19] Correia T., Zhang Q. (2014), "Electrocaloric Effect: an Introduction", In Electrocaloric materials, (pp. 1-15), Springer, Berlin, Heidelberg.

[20] Kutnjak Z., Rožič B., Pirc R., (1999), "Electrocaloric Effect: Theory, Measurements, and Applications'', Wiley encyclopedia of electrical and electronics engineering, 1-19.

[21] Lee S. M., Lee S. H., Yoon C. B., Kim H. E., Lee K. W., (2007), "Low-Temperature Sintering of MnO_2-doped PZT–PZN Piezoelectric Ceramics'', Journal of Electroceramics, 18(3-4), 311-315.

[22] Berksoy-Yavuz A., Mensur-Alkoy Ebru, (2018b), "Electrical properties and Impedance Spectroscopy of Crystallographically Textured 675[Pb ($Mg_{1/3}Nb_{2/3}$) O_3]- 0.325[$PbTiO_3$] Ceramics", Journal of Materials Science: Materials in Electronics, 29, 13310-13320.

[23] Brosnan K. H., Messing G. L., Meyer Jr R. J., Vaudin M. D., (2006), "Texture Measurements in <001> Fiber-Oriented PMN–PT'', Journal of the American Ceramic Society, 89(6), 1965-1971.

[24] Brosnan K. H., Poterala S. F., Meyer R. J., Misture S., Messing, G. L. (2009), "Templated Grain Growth of < 001> Textured PMN-28PT Using $SrTiO_3$ Templates'', Journal of the American Ceramic Society, 92, S133-S139.

[25] Rožič B., Kosec M., Uršič H., Holc J., Malič B., Zhang Q. M., Kutnjak Z., (2011), "Influence of the Critical Point on the Electrocaloric Response of Relaxor Ferroelectrics'', Journal of Applied Physics, 110(6), 064118.

[26] Sebald G., Seveyrat L., Guyomar D., Lebrun L., Guiffard B., Pruvost S., (2006), "Electrocaloric and Pyroelectric Properties of 0.75Pb($Mg_{1/3}Nb_{2/3}$)O_3–0.25 $PbTiO_3$ Single Crystals'', Journal of applied physics, 100(12), 124112.

[27] Zhang T. F., Tang X. G., Ge P. Z., Liu Q. X., Jiang Y. P., (2017), "Orientation Related Electrocaloric Effect and Dielectric Phase Transitions of Relaxor PMN-PT Single Crystals'', Ceramics International, 43(18), 16300-16305.

[28] Bobrek I., Berksoy-Yavuz A., Kaya M. Y., Alkoy S., Okatan M. B., Misirlioglu I. B., Mensur-Alkoy E., (2021), "Temperature Dependent Electrical and Electrocaloric Properties of Textured 0.72 PMN-0.28 PT Ceramics'', Integrated Ferroelectrics, 223(1), 214-227.

[29] Berksoy-Yavuz A., (2018), "Fabrication, Characterization and Energy Harvesting Application of Crystalografic Textured [Pb ($Mg_{1/3}Nb_{2/3}$)O_3]-[$PbTiO_3$]'', PhD Thesis, Gebze Technical University.

[30] Brosnan K. H., (2007), "Processing, Properties, and Application of Textured 0.72 Pb ($Mg_{1/3}Nb_{2/3}$) O3-0.28 $PbTiO_3$ Ceramics'', PhD Dissertation, Penn State University.

BIOGRAPHY

İrem Böbrek graduated from Kocaeli University, Department of Metallurgical and Materials Engineering in 2017. After graduation, she continued her Post.graduate studies and finished her Masters in Materials Science and Engineering in Gebze Technical University, between 2019-2022. During MSc. education, she was a project assistant for 2 years which is supported by AFOSR.